2008

EFFECT OF Si02, TOTAL FeO, Fe3+/Fe2+, AND ALKALIS IN BASALTIC GLASSES ON MID-INFRARED SPECTRA

Celeste D.M. Dufresne
Western University

Recommended Citation

Dufresne, Celeste D.M., "EFFECT OF Si02, TOTAL FeO, Fe3+/Fe2+, AND ALKALIS IN BASALTIC GLASSES ON MID-INFRARED SPECTRA" (2008). *Digitized Theses*. 4154.
https://ir.lib.uwo.ca/digitizedtheses/4154

EFFECT OF SiO_2, TOTAL FeO, Fe^{3+}/Fe^{2+}, AND ALKALIS IN BASALTIC GLASSES ON MID-INFRARED SPECTRA

(Spine title: Mid-IR of Basaltic Glasses)

(Thesis format: Monograph)

by

Céleste D. M. Dufresne

Graduate Program in Geology

A thesis submitted in partial fulfillment
of the requirements for the degree of
Master of Science

Faculty of Graduate Studies
The University of Western Ontario
London, Ontario, Canada

THE UNIVERSITY OF WESTERN ONTARIO
FACULTY OF GRADUATE STUDIES

CERTIFICATE OF EXAMINATION

Supervisor	Examiners
Dr. Penelope L. King	Dr. Neil Banerjee
	Dr. Sean Shieh
	Dr. Yining Huang

The thesis by

Céleste Dale Marie Dufresne

entitled:

Effect of SiO_2, total FeO, Fe^{3+}/Fe^{2+}, and alkalis in basaltic glasses on mid-infrared spectra

is accepted in partial fulfillment of the
requirements for the degree of
Master of Science

Date___________________________

Chair of the Thesis Examination Board

ABSTRACT

This study examines a suite of basaltic glasses to determine how subtle compositional changes affect mid-infrared spectra. Glasses with varying SiO_2, FeO_{total}, Fe^{3+}/Fe^{2+}, and total alkalis were synthesized in a gas-mixing furnace. The glasses were analyzed using micro-reflectance Fourier transform infrared spectroscopy in the region of 650 to 5400 cm^{-1}. The main feature of interest is the Si-O asymmetric stretching vibrational feature located at ~1200 – 800 cm^{-1}. The location of the Si-O feature shifts to higher wavenumbers as SiO_2 content increases. The full width half maximum of the Si-O feature decreases as total alkali content increases. FeO_{total} and Fe^{3+}/Fe^{2+} have no effect on the location or shape of the Si-O feature. These observations indicate that mid-infrared spectra of basaltic glasses may assist in determining the SiO_2 and total alkali contents in basaltic glasses irrespective of FeO_{total} and Fe^{3+}/Fe^{2+}. These observations will aid in the interpretation of remotely sensed data.

Keywords: basalt, basaltic glass, mid-infrared, total FeO, ferric/ferrous, alkalis

Acknowledgements

I would like to thank my supervisor Dr. Penelope L. King for all of the support and guidance she has given me throughout my masters. Thank you for taking a chance on me even though I did not have a geology background. I learnt a lot and I enjoyed my time at Western.

I'd like to thank everyone who has assisted me at some time or another with my lab work whether it be helping me with the gas-mixing furnace, looking at my results, or conducting analyses at other locations.

Throughout my time at Western I made some wonderful friends who were always there to hear the successes or the challenges I experienced throughout my masters. Specifically I would like to thank Lee Stach for all of her support and all of the fun times we had together. Without you my experience at Western would not have been the same.

The successful completion of my masters could not have been accomplished without love and support from family and friends at home. Mom and Dad, I appreciate all the encouragement and love you have given me throughout my life and especially during the final months of my masters. Your support and distractions helped keep me focused on the work at hand while enjoying my time as well. I'd like to thank my sisters for being supportive and understanding of my busy schedule and allowing for sister weekends to be scheduled around that time.

Lastly I would like to thank Paul Schofield for encouraging me to complete a masters and listening to all of my stories on a daily basis. Thank you for being loving and supportive through it all.

Table of Contents

List of Tables

List of Figures

Appendices

1.0 Introduction

Basalts are the most common igneous rocks on Earth's surface and are ubiquitous on planetary bodies. The most common type of basalt is tholeiitic basalt and they are found at convergent and divergent plate margins as well as within plates. Tholeiitic basalts are the major component of Earth's oceanic crust and are also voluminous on continents in large igneous provinces (Best and Christiansen, 2001; Wilson, 1989). Tholeiitic basalts contain minerals +/- glass or may be entirely glassy. For example tholeiitic glass is common on the Earth's seafloor and presumably on cold atmosphere-poor planets where molten material quenched to form glass or where impact processes have melted basaltic rocks.

Tholeiitic basalts have a range of compositions, with SiO_2 content, alkali content (Na_2O + K_2O), molar Mg/(Mg + Fe) (or Mg#), and Fe^{3+}/Fe^{2+} showing the greatest relative variation (Wilson, 1989). Tholeiitic basalts have SiO_2 contents ranging from 45 to 52 wt.% (Hall, 1996). Their total alkali content is generally 5 wt.% or less (Wilson, 1989). In general seafloor tholeiitic basalts have Mg# varying from 25% to 70%, but most have Mg#s between 50% to 65% (Sinton and Detrick, 1992). The Fe^{3+}/Fe^{2+} is ~0.04 to ~0.15 for oceanic basaltic glasses on Earth (Carmichael, 1991), with an average of ~0.12 for mid-ocean ridge basalts (Bézos and Humler, 2005), and from ~0.04 to ~0.19 for basalts on Mars (Herd, 2006). Fe^{3+}/Fe^{2+} is a sensitive indicator of a magma's source region and processes during ascent such as crystallization, assimilation and loss of volatiles (Bézos and Humler, 2005; Carmichael, 1991; Christie et al., 1986; Kress and Carmichael, 1988). Mössbauer spectroscopy allows the analysis of Fe^{3+}/Fe^{2+} within samples.

Knowledge of basalts on other planets comes largely from studying meteorites or using remote sensing techniques such as infrared (IR) spectroscopy. Infrared remote sensing of volcanic materials on Earth and the surfaces of other planets, such as Mars, is a common practice because of the dangers associated with volcanoes and extraterrestrial locations. Currently remotely sensed data of suspected basaltic regions is generally used to identify if basalt and alteration products are present (Bandfield, 2002; Christensen et al., 2000; Farrand and Singer, 1991; Wyatt et al., 2001; Wyatt and McSween, 2002) Infrared spectroscopy has been successfully applied to identifying basalts on Earth and other planets (Crisp et al., 1990; Johnson et al., 2007; Minitti et al., 2005; Minitti et al., 2002; Wyatt et al., 2001; Wyatt and McSween, 2002). This technique is based on using the position of the Si-O asymmetric stretching vibrational feature located at ~1200-800 cm^{-1} (8.3-12.5 μm) in the mid-IR (Bell et al., 1968); hereafter referred to as "Si-O peak" in absorbance or "Si-O trough" in reflectance for brevity. However, there is limited knowledge regarding the effects of subtle changes in basaltic glass composition on the position of the Si-O peak in IR spectra. Changes in the mid-IR spectra as a function of composition (SiO_2, FeO_{total}, Fe^{3+}/Fe^{2+}, and total alkalis) may provide constraints to use mid-IR spectra to determine glass composition and allow it to be used as a spectral endmember.

Remotely sensed IR spectra is obtained in the form of emission spectra which includes a diffuse component (specular, transmitted and refracted light). The relationship between a diffuse reflectance spectrum, in units of %Reflectance, and an emission spectrum, in units of %Emission, is as follows:

$$\varepsilon = 1 - R \qquad [1]$$

Where ε is the emission spectrum, and R is the diffuse reflectance spectrum (King et al., 2004b). A direct transformation from one form to the other can easily be done using equation 1. However, within this study I investigated Kramers-Kronig specular reflectance spectra rather than diffuse reflectance spectra. This factor should however not affect the outcome of the results because a study by Byrnes et al. (2007) that investigated quartzofeldspathic glasses for specular reflectance and emission spectra of the same glassy material indicates that the specular reflectance maxima obtained was very similar to the minima measured for the emission spectrum (Byrnes et al., 2007). Thus I suggest that similar locations are expected for specular reflectance and emission spectra of basaltic glasses, which would make the results of this study directly applicable to remotely sensed mid-IR spectra.

To better understand the IR signal from remote planetary bodies, it is necessary to understand how the signal responds to changes in basaltic glass composition. A few studies of the mid-IR spectra of basaltic glasses include studies by Johnson et al. (2007), Minitti et al. (2002; 2005), and Crisp et al. (1990). Johnson et al. (2007) investigated the mid-IR spectra of partially glassy, shocked natural basaltic rocks and they use spectral deconvolution to determine the mineral and glass contents. Since the basalts were not completely glassy it was not possible to use the result of that study to investigate the role of glass composition on spectral characteristics. Minitti et al. (2002; 2005) investigated the effects of oxidizing crystal-free and crystal-bearing basaltic glasses in air or pure CO_2 at subsolidus temperatures. They found that when the glass was oxidized, crystals of hematite and pyroxene were produced which in turn affected the mid-IR spectra. Hematite changed the spectra by narrowing the broad feature at ~1200 – 800 cm^{-1} and by the appearance of a new spectral feature at ~540 cm^{-1}. Pyroxene altered the spectra by creating small features between 800 – 1100 cm^{-1}. Crisp et al. (1990) investigated weathering of natural basaltic glass. They observed that over time the IR spectrum for the exterior portion of the glass that was exposed to weathering produced a spectrum different than the initial glass investigated and the interior portion of the glass. They attribute the observed spectral changes centred at ~1080 cm^{-1} and centred between ~900 – 950 cm^{-1} to increased ordering of the silicate structure at the surface, specifically the formation of sheetlike and chainlike silica tetrahedra. All three of these studies however do not specifically look at how the composition of the glass affects the spectra.

It is well-established that an increase in SiO_2 content increases the position of the major Si-O peak centred at ~1050 – 1100 cm^{-1} in glasses (Byrnes et al., 2007; Dalby, 2007; Dalby et al., 2006; Logan et al., 1975; Minitti et al., 2007). Dalby (2007) has also shown that as glass composition changes from basaltic (~43 to 53 wt.% SiO_2) to rhyolitic (~65 to 75 wt.% SiO_2) a shoulder appears at ~1220 cm^{-1} which may also be correlated with SiO_2 content. Despite these previous studies, very little work has been done to systematically examine how SiO_2 content affects mid-IR spectra in glasses in a small compositional range (e.g., 45 to 55 wt.% SiO_2).

Despite the large variations in FeO_{total} and Fe^{3+}/Fe^{2+} to my knowledge there are no studies that directly address how these elements change the mid-IR spectra. However, there are studies in the ultraviolet-visible-near IR regions that investigated the effects of FeO_{total} and Fe^{3+}/Fe^{2+} in silicate glasses which contain features that are attributed to Fe electronic transitions (Bell and Mao, 1976; Kakkadapu et al., 2003).

As indicated above, alkali contents may also vary substantially in basaltic rocks; however, there are no systematic studies investigating whether the alkali content of basaltic glasses changes mid-IR spectra. Studies on other glass compositions suggest that alkalis play an important role in changing mid-IR spectra. For example, mid-IR spectra for binary and ternary sodium silicate glasses (with ~11 to 40 wt.% Na_2O) show that as Na_2O increases the Si-O peak becomes resolved into two peaks, located at ~920 – 975 cm^{-1} and ~1040 – 1070 cm^{-1}, rather than a broad feature (Domine and Piriou, 1983; Merzbacher and White, 1988; Sweet and White, 1969). Those studies also indicate that as Na_2O increases the two peaks are more resolved.

To better understand the mid-IR of basaltic glasses this study investigates subtle compositional changes of multiple unaltered, crystal-free basaltic glasses. The main goals of this study were to investigate the effects of SiO_2, FeO_{total}, Fe^{3+}/Fe^{2+}, and total alkalis in basaltic glass samples in order to better constrain the IR spectrum of basaltic glasses. If we know how certain compositional changes in glasses affect the IR spectra we can use this knowledge when interpreting remotely sensed data, and in turn gain a better knowledge of probable compositions.

2.0 Experimental techniques

The synthetic basaltic glasses analyzed in this study were either synthesized specifically for this study or obtained from previous studies as indicated in Table 1. Basaltic glasses synthesized in this study were prepared using tholeiitic basalt collected from the 1921 Pu'u O'o lava flow, Kilauea, Hawaii, that was previously used by Lui (2005). A sample from nearby has been the subject of many experimental studies (Holloway and Burnham, 1972). The tholeiitic basalt was ground under ethanol to <30 μm in size using an agate mortar and pestle. Particle size was confirmed using a polarizing microscope. The powdered sample was placed in a Pt crucible and sintered at 1100 °C in a box furnace for 6 hours. It was then ground under ethanol for 15 minutes. This sintering and grinding process was repeated four separate times to ensure homogeneity. The powdered sample was then combined with polyethylene oxide to form a paste (O'Neill and Mavrogenes, 2002), which was mounted onto ~2.5 mm diameter loops of Re ribbon (0.025 mm thick by 0.80 mm wide), loops of Pt wire (0.25 mm diameter), or loops of Fe-doped Pt wire (0.25 mm diameter). Once mounted onto the loops, the samples were placed in a 110 °C oven for 30 minutes to harden.

A Deltech vertical, one-atmosphere, gas-mixing furnace, set at 1400 °C, was used to synthesize the basaltic glasses. Air or mixtures of $CO_{2(g)}$ and $CO_{(g)}$ were used to create the desired oxygen fugacities for the syntheses (Table 1). The oxygen fugacities of each run were confirmed using a zirconia electrode (details in Appendix A). Sample loops were suspended on a thin piece of Pt wire (0.127 mm diameter) in the hot spot of the furnace for durations of 5 to 200 hours (see Table 1). To quench the sample to a glass, an electric current was applied to the thin Pt wire causing the sample loops to drop into the furnace base, which was pre-cooled with ice water. The Re ribbon or Pt wire was removed from the glass samples either by directly pulling it off or by using a steel rock crusher and hammer. A small portion of the sample was ground and placed under a polarizing microscope to confirm that the sample was glassy. A partial glass bead from each sample run was mounted in epoxy and polished to a 1 μm finish for further analyses.

The main goal of this study was to synthesize basaltic glasses of similar but slightly varying compositions. In order to accomplish this goal synthesis conditions were varied in order to take advantage of two common issues that occur during experimental synthesis: Fe-loss and alkali-loss.

Iron-loss occurs when Fe from the melt alloys with the sample holder material, generally noble metals. The degree to which Fe alloying occurs varies with the composition of the sample holder; for instance, Fe alloys significantly with Pt (Mysen and Richet, 2005), but only minimally with Re (Borisov and Jones, 1999) and a larger sample holder to sample ratio causes more Fe-loss (Corrigan and Gibb, 1979). Other factors that influence Fe-loss include the duration of the experiment because Fe alloying increases with time (Corrigan and Gibb, 1979; Donaldson, 1979), and the oxygen fugacity (f_{O_2}) of the synthesis because Fe alloying increases as f_{O_2} decreases (Donaldson, 1979). For the remainder of this study, f_{O_2} will be referenced with respect to the nickel-nickel oxide buffer, NNO, solid buffer curve, which is a way of reporting f_{O_2} irrespective of temperature (e.g., $\log(f_{O_2})$ = some value ΔNNO).

I used Pt wire, Fe-doped Pt wire, and Re ribbon as sample holders in order to obtain basaltic glasses with a range of Fe_{total} contents. Glasses synthesized using Fe-doped Pt wire at high f_{O_2} had higher Fe_{total} contents than the starting basaltic powders because Fe diffused from the wire to the melt. Glasses synthesized using Fe-doped Pt wire at low f_{O_2} had lower Fe_{total} contents than the starting basaltic powder because Fe diffused from the melt to the wire. In contrast, glasses synthesized at a variety of f_{O_2} on Pt wire, Fe-doped Pt wire, and Re ribbon had similar Fe contents to the starting basaltic powder. The Re ribbon was not used at f_{O_2} above NNO-1.5 because Re oxidizes readily at those conditions (Borisov and Jones, 1999).

Alkali-loss occurs during high temperature syntheses because alkali oxides, specifically Na_2O and K_2O, tend to vaporize (Corrigan and Gibb, 1979; Donaldson, 1975; Donaldson, 1979; O'Neill, 2005). Alkali-loss increases as temperature is increased, or the duration of the synthesis is increased (Corrigan and Gibb, 1979; Donaldson, 1979), or f_{O_2} is lowered (Donaldson, 1979), or the surface area of the melt to mass ratio is increased (Corrigan and Gibb, 1979). These factors were varied in order to increase alkali-loss in some of the syntheses in this study. Alkali-poor glasses were synthesized on Pt wire at an f_{O_2} of NNO+2.95 (CO_2 gas only) for durations of 100 and 200 hours in order to increase alkali-loss. Alkali-rich glasses were synthesized by adding Na_2CO_3 or K_2CO_3 and melting samples on Pt wire at an f_{O_2} of NNO+2.95 for a duration of 5 hours. The mixture of basalt and alkali carbonates were ground for 20 minutes under ethanol in an agate mortar and pestle prior to being sintered twice for 3 hours at 800 °C and ground for 15 minutes under ethanol after each sintering step. The mixtures were melted for a duration of 5 hours before being quenched to the final glass.

3.0 Analytical techniques

3.1 Electron microprobe analysis

Electron microprobe analysis of the basaltic glasses was performed by Glenn Poirier using a JEOL 733 Superprobe at the Canadian Museum of Nature to confirm that the glasses were homogeneous, crystal-free, and the correct composition. The sample disks were carbon coated prior to analysis. Wavelength dispersive spectrometry analyses were conducted, using a beam current of 20 nA, a beam diameter of 10 μm, and an accelerating voltage of 15 kV, on each of the individual glass pieces.

3.2 Mössbauer spectroscopy

Mössbauer spectroscopy for eight synthetic basaltic glasses was performed at Mount Holyoke College, South Hadley, MA, USA. The following methods were provided by Dr. M. Darby Dyar who performed the analyses. Mössbauer spectra were collected at 295 K on a WEB Research Co. model WT302 spectrometer equipped using an ~50 mCi ^{57}Co in Rh source. Approximately 15 – 18 mg of each glass sample was crushed under acetone and subsequently mixed with a sugar-acetone solution in order to form a coating around each grain to prevent them from positioning themselves in a preferred orientation. The coated grains were place in a sample holder and covered with Kapton tape. Spectra were collected over a duration of 24 – 48 hours with baseline counts of ~6 – 14 million after Compton correction, due to relatively small FeO_{total} content. Data were collected in 2048 channels and corrected for nonlinearity via interpolation to a linear velocity scale, which is defined by the spectrum of the 25 μm Fe foil used for calibration. Data were then folded before fitting, using a procedure that folds the spectrum about the channel value that produces the minimum least squares sum difference between the first half of the spectrum and the reflected second half of the spectrum.

Mössbauer data for the glasses were modeled at Mount Holyoke College using an in-house program generously made available to them by Eddy De Grave and Toon Van Alboom at the University of Ghent, in Belgium. The spectra were processed using the Dist3e program, which models spectra using quadrupole splitting or hyperfine field distributions for which the subspectra are Lorentzian shaped lines. The program uses velocity approximations rather than the full Hamiltonian and does not presume any particular shape of the distribution. Widths (Γ), isomer shifts (δ), and quadrupole splittings (Δ) of the doublets were allowed to vary. If the widths fell below 0.24 mm/s, they were held constant. Overall errors on isomer shift and quadrupole splitting are ±0.05 – 0.1 mm/s, but errors on total Fe^{3+} areas are probably ±1 – 3% absolute.

3.3 Determination of calculated Fe^{3+}/Fe^{2+}

As mentioned in section 3.2, Mössbauer spectroscopy was only collected for eight glasses. To calculate the Fe^{3+}/Fe^{2+} ratios of the remaining glasses we used an equation presented by Kress and Carmichael (1991):

$$\ln\left(\frac{X_{Fe_2O_3}}{X_{FeO}}\right) = a\ln(f_{O_2}) + \frac{b}{T} + c + \sum_i d_i X_i + \qquad [2]$$

$$e\left[1 - \frac{T_O}{T} - \ln\left(\frac{T}{T_O}\right)\right] + f\frac{P}{T} + g\frac{(T-T_O)P}{T} + h\frac{P^2}{T}$$

where X is mole fraction, f_{O_2} is oxygen fugacity, T is temperature in degrees Kelvin, T_O is 1673 K, P is pressure in Pascals, a – h are constants as follows: a = 0.196, b = 1.1492 x 10^4 K, c = -6.675, $d_{Al_2O_3}$ = -2.243, d_{FeO^*} = -1.828, d_{CaO} = 3.201, d_{Na_2O} = 5.854,

d_{K_2O} = 6.215, e = -3.36, f = -7.01 x 10^{-7} KPa^{-1}, g = -1.54 x 10^{-10} Pa^{-1}, and h = 3.85 x 10^{-17} KPa^{-2}. It is necessary to iterate this equation in order to obtain the calculated Fe^{3+}/Fe^{2+} because the mole fraction of FeO*, which considers all of the Fe as ferrous, slightly changes as the ferric and ferrous changes. Use of this equation assumes that the melt had sufficient time to reach equilibrium with its surrounding fO_2 (Kress and Carmichael, 1988).

3.4 Micro-reflectance Fourier Transform infrared spectroscopy

Micro-reflectance (μR) Fourier Transform Infrared (FTIR) analyses of the basaltic glasses were collected using a Nicolet FTIR spectrometer with a microscope attachment in the Experimental Analysis Laboratory at the University of Western Ontario. Specifically the spectrometer is a Nexus 670 with a Globar source, KBr beamsplitter, and the Continuμm microscope has a MCT/A detector that was cooled with liquid nitrogen. Sample disks were purged with dry air prior to collecting spectra. Each spectrum was collected in a spectral range of 5400 – 650 cm^{-1} over 300 scans with 4 cm^{-1} resolution in a 100 μm by 100 μm sampling area. A background spectrum, collected on a gold slide before each sample analysis was divided from the sample spectrum. Spectra were obtained for each glass piece in approximately the same locations in which the electron microprobe analyses were conducted. The raw spectra were collected in units of percent reflectance (%R) and were subsequently transformed into units of Kramers-Kronig (KK) absorbance by smoothing over an ~40.5 cm^{-1} window and performing a KK correction. Trough locations were recorded for the reflectance spectra prior to smoothing and peak locations were recorded for the KK-absorbance spectra before the spectra were baseline corrected since values after baseline correction changed by less than 0.5 cm^{-1}.

The KK correction removes the effects of optical constants, such as the refractive index, n, and the dielectric constant, ε, that vary as a function of wavelength from the specular reflectance spectra and transforms a spectrum from units of percent reflectance to KK absorption units (McMillan and Hofmeister, 1988). Incident wavelengths that come in contact with the medium can be reflected, transmitted, or absorbed. Thus, optical constants can affect the spectra and in turn make comparisons between different media difficult. The refractive index of a medium, n, is defined by:

$$n = c/v \qquad [3]$$

where c is the speed of light in a vacuum and v is the velocity of light as it passes through the medium. The refractive index is related to the dielectric constant, ε, by

$$\varepsilon = n^2 \qquad [4]$$

In a reflectance spectrum, the refractive index and dielectric constant are comprised of a real and an imaginary portion which are related as follows:

$$n = n' + in'' \qquad [5]$$

$$\varepsilon = n'^2 - n''^2 + 2in'n'' \qquad [6]$$

where n' is the real portion of the refractive index, i is $\sqrt{-1}$, and n" is the imaginary portion of the refractive index. These terms are related to a reflectance spectrum by:

$$R = \frac{(n' - 1)^2 + (n'')^2}{(n' + 1)^2 + (n'')^2} \qquad [7]$$

where R is the infrared reflection coefficient. The real and imaginary parts of this equation are related to each other through:

$$r_i = r\, e^{i\theta} \qquad [8]$$

where r_i is the imaginary part of the reflectivity ($\sqrt{R}$), r is the real part of the reflectivity, and θ is the phase shift which is proportional to the magnitude of the absorption coefficient. A KK transform is performed in order to determine the phase shift and produce an absorption spectrum. The formula for the KK transform is:

$$\theta(v_i) = \frac{2v_i}{\pi} \int_0^\infty \frac{\ln r(v) - \ln r(v_i)}{v_i^2 - v^2} dv \qquad [9]$$

where ν is the real portion of the frequency and ν_i is imaginary portion of the frequency. Once the phase shift is determined so are the real and imaginary parts of the reflectivity. It is then possible to use this information to calculate the refractive index and the dielectric constant of the medium:

$$n' = \frac{(1-r^2)}{1+r^2-2r\cos\theta} \qquad [10]$$

$$n'' = \frac{2r}{1+r^2-2r\cos\theta} \qquad [11]$$

Since the KK formula must be evaluated over a range of wavelengths ranging from zero to infinity, software programs extrapolate the wings of the reflectance spectrum in order to perform this transform. By performing the KK transform the effect from the refractive index is removed and allows for accurate comparisons between KK absorbance spectra (McMillan and Hofmeister, 1988).

3.5 Calculation of refractive indices

The calculated refractive indices for the glasses were determined using a formula developed by Church and Johnson (1980) that uses the normalized composition of the silicate glass and the refractive indices of the oxides.

$$n = \sum_i (n_i w_i) + 1 \qquad [12]$$

where n is the refractive index of the glass, n_i is the refractive index for the oxide, and w_i is the normalized weight percent of the oxide (Church and Johnson, 1980). This formula assumes that all Fe is present in ferrous form.

4.0 Results

4.1 Glass composition

Electron microprobe data for the synthetic basaltic glasses (Table 1) indicate that each glass is homogeneous within electron microprobe error and crystal-free. Data reported in Table 1 are averages based on the number of analyses of each glass piece and the errors presented are standard deviations. While the averages are useful when evaluating the entire dataset, individual spot locations were considered when comparing IR results to the electron microprobe data for the basaltic glasses synthesized in this study. Data for the individual spot locations can be found in a data repository (Appendix B).

Electron microprobe data revealed that the synthetic basaltic glasses have similar compositions for all oxides except SiO_2 that varied from 47.18 to 55.57 wt.%, FeO_{total} that varied from 6.06 to 16.30 wt.%, Na_2O that varied from 0.04 to 3.12 wt.%, and K_2O that varied from 0.02 to 1.80 wt.% (Table 1). From these results I am able to neglect changes in Al_2O_3 because even though Al may contribute to the Si-O peak the electron microprobe results indicate that Al_2O_3 does not vary substantially. Since there is a range of SiO_2 within the suite of glasses I examined how FeO_{total} and total alkalis (Na_2O + K_2O) vary as SiO_2 increases in increments of 1.0 wt.% (Table 2). These results indicate that as SiO_2 increases the FeO_{total} decreases within the suite of glasses, but that total alkalis are not affected by the SiO_2 in the suite of glasses.

To classify the synthetic glasses I used CIPW norm calculations as well as SiO_2 and total alkalis (Appendix B). The CIPW norm calculations revealed that the main CIPW normative components of the glasses are plagioclase, diopside, hypersthene, quartz, and orthoclase (Appendix B). Accessory CIPW normative minerals include ilmenite, magnetite, hematite, and apatite (Appendix B). Since none of the basalts contain feldpathoids (nepheline or leucite) they all plot as tholeiitic on a basalt tetrahedron (Yoder and Tilley, 1962). However, classification through SiO_2 and total alkalis (Le Maitre, 1989) reveals that some of the glasses, those with SiO_2 greater than 52.0 wt.%, fall within the range of basaltic andesites (Fig. 1; Appendix B). Nonetheless all samples will be considered when interpreting data.

Table 1: Summary of experimental data for the synthetic basaltic glasses.

	NNO-4_Re	NNO-3_Re	NNO-3_dPt	NNO-3_dPt	NNO-2_Re	NNO-1.5_Re	NNO-1.5_dPt
# of IR and probe analyses	4	4	10	8	5	4	5
T range (°C)	1414-1417	1413-1417	1413-1416	1414-1417	1414-1418	1414-1420	1413-1416
$\log (f_{O_2})$	-10.01	-8.69	-8.70	-8.66	-7.63	-7.11	-7.12
Loop material	Re	Re	dPt	dPt	Re	Re	dPt
Duration (hours)	5	5	5	5	5	5	5
Other							
wt.%							
SiO_2	51.60 ± 0.10	51.13 ± 0.20	54.86 ± 0.57	53.19 ± 0.25	52.28 ± 0.17	51.52 ± 0.23	51.42 ± 0.09
TiO_2	2.67 ± .01	2.62 ± 0.02	2.79 ± 0.04	2.77 ± 0.06	2.65 ± 0.03	2.73 ± 0.01	2.74 ± 0.06
Al_2O_3	11.94 ± 0.04	11.61 ± 0.14	12.50 ± 0.13	12.23 ± 0.15	12.00 ± 0.07	11.92 ± 0.09	12.05 ± 0.06
FeO	11.46 ± 0.07	11.29 ± 0.07	6.91 ± 0.81	8.53 ± 0.19	11.59 ± 0.06	11.32 ± 0.11	10.37 ± 0.05
MnO	0.17 ± 0.01	0.16 ± 0.01	0.16 ± 0.03	0.15 ± 0.03	0.16 ± 0.02	0.16 ± 0.03	0.16 ± 0.05
MgO	9.94 ± 0.05	10.01 ± 0.05	10.56 ± 0.12	10.35 ± 0.17	10.01 ± 0.04	9.85 ± 0.08	9.88 ± 0.11
CaO	10.74 ± 0.02	10.43 ± 0.06	11.21 ± 0.10	10.89 ± 0.13	10.76 ± 0.05	10.73 ± 0.08	10.67 ± 0.05
Na_2O	0.40 ± 0.01	0.44 ± 0.02	0.66 ± 0.10	1.36 ± 0.03	0.33 ± 0.04	0.06 ± 0.01	1.48 ± 0.03
K_2O	0.25 ± 0.01	0.24 ± 0.01	0.33 ± 0.01	0.40 ± 0.02	0.05 ± 0.02	0.03 ± 0.01	0.43 ± 0.03
P_2O_5	0.15 ± 0.01	0.15 ± 0.01	0.11 ± 0.01	0.22 ± 0.01	0.24 ± 0.01	0.23 ± 0.02	0.21 ± 0.01
Total	99.30	98.08	100.08	100.08	100.07	98.54	99.40
Micro-reflectance IR minimum location (μR min. loc.; cm^{-1})	1233 ± 2	1233 ± 1	1242 ± 2	1235 ± 2	1237 ± 5	1238 ± 2	1232 ± 1
Kramers-Kronig absorbance maximum location (KK-abs max. loc.; cm^{-1})	1038 ± 0	1040 ± 3	1050 ± 3	1044 ± 2	1039 ± 1	1039 ± 2	1040 ± 1
Kramers-Kronig absorbance full width half maximum (KK-abs FWHM; cm^{-1})	222 ± 1	222 ± 1	228 ± 3	212 ± 3	227 ± 1	234 ± 1	204 ± 1
Mg#	60.7 ± 0.2	61.2 ± 0.2	73.1 ± 2.4	68.4 ± 0.8	60.6 ± 0.2	60.8 ± 0.4	62.9 ± 0.3
Total alkali wt.%	0.65 ± 0.01	0.68 ± 0.03	0.99 ± 0.11	1.76 ± 0.03	0.39 ± 0.06	0.08 ± 0.01	1.91 ± 0.04
Calculated Fe^{3+}/Fe^{2+}	0.0268 ± 0.0001	0.0487 ± 0.0001	0.0534 ± 0.0004	0.0550 ± 0.0003	0.0775 ± 0.0004	0.0968 ± 0.0003	0.1076 ± 0.0003
Measured Fe^{3+}/Fe^{2+}		0.0526	0.0753			0.0989	0.0753
Calculated refractive index, n	1.611 ± 0.001	1.611 ± 0.001	1.596 ± 0.003	1.601 ± 0.001	1.611 ± 0.000	1.612 ± 0.000	1.607 ± 0.001

Table 1 Continued.

	NNO+1_Pt	NNO+3_Pt	NNO+3_d Pt	Alk-5A	Alk-5B	Alk-5C	Alk-5D
# of IR and probe analyses	3	6	10	4	5	4	5
T range (°C)	1414-1417	1414-1418	1408-1412	1414-1417	1414-1417	1408-1412	1408-1412
log (f_{O_2})	-4.55	-2.95	-2.95	-2.95	-2.95	-2.95	-2.95
Loop material	Pt	Pt	dPt	Pt	Pt	Pt	Pt
Duration (hours)	5	5	5	5	5	5	5
Other				3.22 mg Na_2CO_3 added to 248.19 mg basalt	5.47 mg Na_2CO_3 added to 246.91 mg basalt	3.53 mg K_2CO_3 added to 248.79 mg basalt	7.23 mg K_2CO_3 added to 247.56 mg basalt
wt.%							
SiO_2	50.86 ± 0.13	50.25 ± 0.45	49.70 ± 0.61	50.90 ± 0.39	50.02 ± 0.09	51.62 ± 0.24	51.05 ± 0.37
TiO_2	2.71 ± 0.05	2.60 ± 0.04	2.59 ± 0.03	2.67 ± 0.02	2.65 ± 0.08	2.61 ± 0.05	2.61 ± 0.01
Al_2O_3	11.85 ± 0.01	11.68 ± 0.12	11.95 ± 0.37	11.78 ± 0.09	11.59 ± 0.05	11.75 ± 0.14	11.66 ± 0.08
FeO	9.67 ± 0.26	10.78 ± 0.17	12.65 ± 0.24	10.19 ± 0.17	10.61 ± 0.09	10.78 ± 0.02	10.53 ± 0.15
MnO	0.17 ± 0.01	0.15 ± 0.03	0.16 ± 0.02	0.17 ± 0.03	0.16 ± 0.03	0.16 ± 0.01	0.15 ± 0.03
MgO	9.90 ± 0.03	9.68 ± 0.07	9.59 ± 0.16	9.64 ± 0.15	9.52 ± 0.10	9.78 ± 0.11	9.68 ± 0.14
CaO	10.60 ± 0.03	10.49 ± 0.05	10.24 ± 0.08	10.42 ± 0.10	10.41 ± 0.03	10.32 ± 0.07	10.32 ± 0.10
Na_2O	1.80 ± 0.03	1.94 ± 0.03	1.89 ± 0.06	2.57 ± 0.08	3.04 ± 0.06	1.98 ± 0.03	1.89 ± 0.03
K_2O	0.48 ± 0.01	0.48 ± 0.02	0.45 ± 0.02	0.49 ± 0.01	0.47 ± 0.01	0.95 ± 0.02	1.71 ± 0.06
P_2O_5	0.21 ± 0.01	0.22 ± 0.01	0.18 ± 0.04	0.15 ± 0.03	0.19 ± 0.02	0.20 ± 0.03	0.17 ± 0.02
Total	98.26	98.26	99.39	98.98	98.65	100.12	99.75
μR min. loc. (cm^{-1})	1231 ± 2	1229 ± 2	1224 ± 2	1229 ± 0	1226 ± 2	1228 ± 1	1227 ± 1
KK-abs max. loc. (cm^{-1})	1040 ± 2	1040 ± 1	1036 ± 1	1040 ± 2	1039 ± 1	1041 ± 1	1041 ± 1
KK-abs FWHM (cm^{-1})	201 ± 1	200 ± 1	203 ± 2	194 ± 1	189 ± 1	199 ± 1	189 ± 1
Mg#	64.6 ± 0.6	61.6 ± 0.5	57.5 ± 0.8	62.8 ± 0.1	61.5 ± 0.4	61.8 ± 0.3	62.1 ± 0.5
Total alkali wt.%	2.28 ± 0.02	2.42 ± 0.03	2.34 ± 0.07	3.06 ± 0.09	3.51 ± 0.06	2.92 ± 0.04	3.60 ± 0.07
Calculated Fe^{3+}/Fe^{2+}	0.3557 ± 0.0017	0.7253 ± 0.0021	0.7084 ± 0.0095	0.7566 ± 0.0037	0.7748 ± 0.0027	0.7516 ± 0.0046	0.7767 ± 0.0017
Measured Fe^{3+}/Fe^{2+}	0.5386	1.1279	1.0200				
Calculated refractive index, n	1.605 ± 0.001	1.608 ± 0.001	1.614 ± 0.001	1.605 ± 0.001	1.607 ± 0.000	1.606 ± 0.001	1.605 ± 0.001

Table 1 Continued.

*The bulk chemistry for B-Alk was taken from Oskarsson et al. (1982).

**Number of IR spectra = 1. Electron microprobe data obtained from an average of multiple points.

	Alk-100	Alk-200	NNO+5 _Pt	NNO+5 _dPt	DL0413	B-Alk*	Fe-Free MORB
# of IR and probe analyses	4	3	4	10	1**	1**	1**
T range (°C)	1408-1412	1408-1412	1413-1417	1408-1412	1300		1400
log (f_{O_2})	-2.95	-2.95	-0.68	-0.68	NNO-2	air	air
Loop material	Pt	Pt	Pt	dPt	PC exp. Pt capsule	Fe-doped Pt crucible	Fe-doped Pt crucible
Duration (hours)	100	200	5	5	3	N/A	2
Other					Lui (2005) P = 0.5 GPa 0.97 wt.% H_2O	King (in Dalby 2007)	Lockard (2005)
wt.%							
SiO_2	51.70 ± 0.05	52.79 ± 0.47	50.19 ± 0.15	48.87 ± 1.17	50.87 ± 0.32	48.25	59.20 ± 0.28
TiO_2	2.71 ± 0.04	2.77 ± 0.04	2.65 ± 0.05	2.54 ± 0.07	2.59 ± 0.08	4.22	1.29 ± 0.04
Al_2O_3	12.02 ± 0.21	12.22 ± 0.21	11.69 ± 0.07	11.30 ± 0.32	12.13 ± 0.14	12.38	18.27 ± 0.62
FeO	10.73 ± 0.08	10.31 ± 0.16	10.97 ± 0.06	14.39 ± 1.77	10.36 ± 0.16	14.51	0.12 ± 0.05
MnO	0.17 ± 0.03	0.16 ± 0.02	0.17 ± 0.02	0.16 ± 0.04	0.16 ± 0.06	0.22	
MgO	10.02 ± 0.13	10.17 ± 0.17	9.74 ± 0.10	9.45 ± 0.27	9.37 ± 0.24	5.35	11.14 ± 0.13
CaO	10.67 ± 0.13	10.69 ± 0.05	10.39 ± 0.06	10.07 ± 0.16	10.51 ± 0.14	10.00	7.55 ± 0.16
Na_2O	1.43 ± 0.04	0.87 ± 0.03	1.86 ± 0.04	1.68 ± 0.10	2.06 ± 0.06	2.97	1.73 ± 0.16
K_2O	0.44 ± 0.02	0.38 ± 0.01	0.49 ± 0.02	0.39 ± 0.03	0.48 ± 0.03	0.77	0.04 ± 0.01
P_2O_5	0.07 ± 0.00	0.04 ± 0.01	0.22 ± 0.02	0.19 ± 0.01	0.28 ± 0.04	0.56	0.03 ± 0.02
Total	99.97	100.41	98.36	99.05	98.81	99.23	99.37
μR min. loc (cm^{-1})	1230 ± 1	1232 ± 0	1232 ± 2	1225 ± 3			
KK-abs max. loc. (cm^{-1})	1041 ± 1	1044 ± 3	1040 ± 1	1038 ± 4	1037.5	1033.7	1079.8 ± 3.1
KK-abs FWHM (cm^{-1})	211 ± 1	223 ± 1	206 ± 1	209 ± 2	193	195	244 ± 7
Mg#	62.5 ± 0.4	63.8 ± 0.4	61.3 ± 0.3	53.9 ± 3.7	61.7	39.7	
Total alkali wt.%	1.87 ± 0.05	1.25 ± 0.03	2.35 ± 0.06	2.06 ± 0.13	2.54 ± 0.09	3.74	1.78 ± 0.15
Calculated Fe^{3+}/Fe^{2+}	0.7191 ± 0.0047	0.6969 ± 0.0044	2.0011 ± 0.0110	1.8992 ± 0.0700			
Measured Fe^{3+}/Fe^{2+}			1.1742				
Calculated refractive index, n	1.608 ± 0.001	1.607 ± 0.001	1.609 ± 0.001	1.620 ± 0.006	1.604	1.622	1.553

Table 2: Summary of FeO_{total} and total alkali ranges when SiO_2 is held within 1.0 wt.%.

$SiO_2 \pm 0.50$ wt.%	FeO_{total} wt.%	Total alkali wt.%
47	16.30	1.95
48	14.51 - 16-13	1.86 – 3.74
49	12.62 – 12.89	2.09 – 2.30
50	10.50 – 12.89	2.10 – 3.60
51	9.39 – 12.50	0.09 – 3.68
52	10.33 – 11.66	0.07 – 3.59
53	8.27 – 11.59	0.29 – 1.80
54	6.67 – 8.54	0.93 – 1.72
55	6.06 – 7.12	0.92 – 0.95
56	6.65	0.94

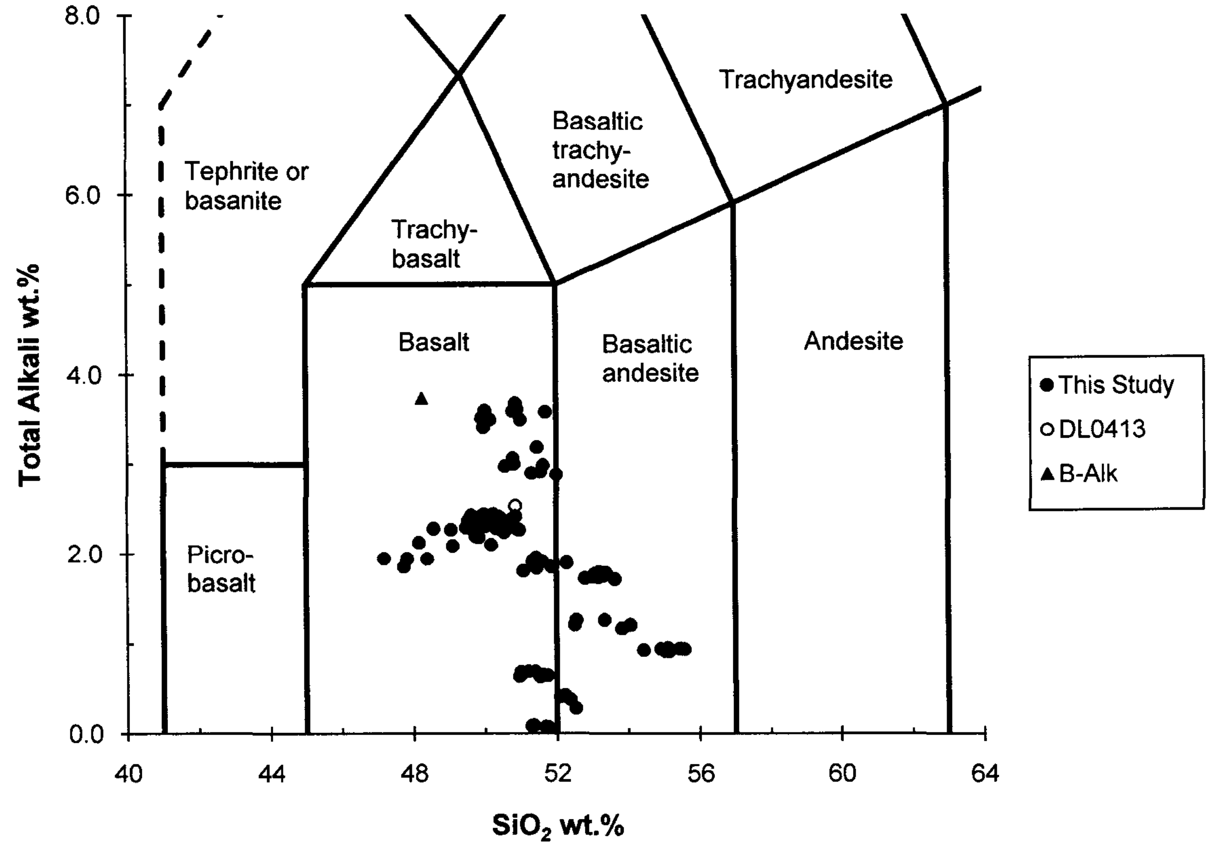

Figure 1: Basalt classification according to SiO_2 and total alkalis (Le Maitre, 1989). Closed circles indicate the classification of synthetic glasses in this study, which are individual spot locations. The open circle is the average composition of DL0413 (Lui, 2005). The closed triangle is the average composition of B-Alk (Oskarsson et al., 1982).

4.2 Correlation matrix

A correlation matrix (Table 3) was generated using Statview in order to determine trends within the data for the Fe-bearing basaltic glasses presented in Table 1. A total of 98 individual spot locations and 2 averaged glasses (B-Alk and the glass synthesized by Lui (2005) in Table 1) were used (Appendix B). Results for correlations with calculated Fe^{3+}/Fe^{2+} are not presented in Table 3 because no correlations were observed. The matrix in Table 3 indicates that SiO_2 has $R^2 \geq 0.64$ with FeO_{total}, CaO, Mg#, and calculated refractive index (n).

Table 3: Correlation matrix, R^2 values, created in Statview, for data presented in Appendix B. Data that show significant correlations are underlined and bold.

	KK-peak loc. (cm^{-1})	KK FWHM (cm^{-1})	SiO_2 wt.%	FeO wt.%	MgO wt.%	CaO wt.%	Na_2O wt.%	K_2O wt.%	Mg#	Total alkali wt.%	Calculated refractive index, n
KK- peak loc. (cm^{-1})	1.00	0.16	0.70	0.71	0.38	0.59	0.11	0.00	0.73	0.06	0.69
KK FWHM (cm^{-1})	0.16	1.00	0.33	0.07	0.22	0.37	0.86	0.44	0.13	0.92	0.03
SiO_2 wt.%	**0.70**	0.33	1.00	0.78	0.50	0.83	0.30	0.02	0.80	0.24	0.75
FeO wt.%	**0.71**	0.07	**0.78**	1.00	0.41	0.73	0.05	0.00	0.93	0.03	0.97
MgO wt.%	0.38	0.22	0.50	0.41	1.00	0.44	0.25	0.05	0.66	0.22	0.39
CaO wt.%	0.59	0.37	**0.83**	**0.73**	0.44	1.00	0.33	0.11	0.75	0.32	0.62
Na_2O wt.%	0.11	**0.86**	0.30	0.05	0.25	0.33	1.00	0.23	0.12	0.91	0.02
K_2O wt.%	0.00	0.44	0.02	0.00	0.048	0.11	0.23	1.00	0.00	0.52	0.02
Mg#	**0.73**	0.13	**0.80**	**0.93**	**0.66**	**0.75**	0.12	0.00	1.00	0.08	0.90
Total alkali wt.%	0.06	**0.92**	0.24	0.03	0.22	0.32	**0.91**	0.52	0.08	1.00	0.01
Calculated refractive index, n	**0.69**	0.03	**0.75**	**0.97**	0.39	0.62	0.02	0.02	**0.90**	0.01	1.00

4.3 Calculated Fe^{3+}/Fe^{2+}

The basaltic glasses synthesized for this study were done at oxygen fugacities ranging from NNO-4.4 to NNO+5 (air). Calculated Fe^{3+}/Fe^{2+} were generated using equation 1 and are reported in Table 1. In order to determine the accuracy of the calculated Fe^{3+}/Fe^{2+} I compared them to measured Fe^{3+}/Fe^{2+} generated from Mössbauer spectroscopy (Fig. 2) that were conducted on selected glass samples (Table 1). It is however important to note that the calculated data are for averaged individual electron microprobe spot analyses and the measured Fe^{3+}/Fe^{2+} from Mössbauer data are for bulk analyses of the glasses. Mössbauer parameters used for the determination of the Fe^{3+}/Fe^{2+} are given in Table 4. When the calculated and measured values are compared (Fig. 3), the calculated values are systematically lower than the measured values with a linear correlation of calculated values = 0.67*measured values (R^2 = 0.99) for samples synthesized at oxygen fugacities less than NNO+3. When all of the data is considered a linear correlation of calculated values = 1.03*measured values (R^2 = 0.68) was obtained (Fig. 4). The sample synthesized in air (NNO+5) is the only sample that had a significantly higher calculated value when compared to the measured value.

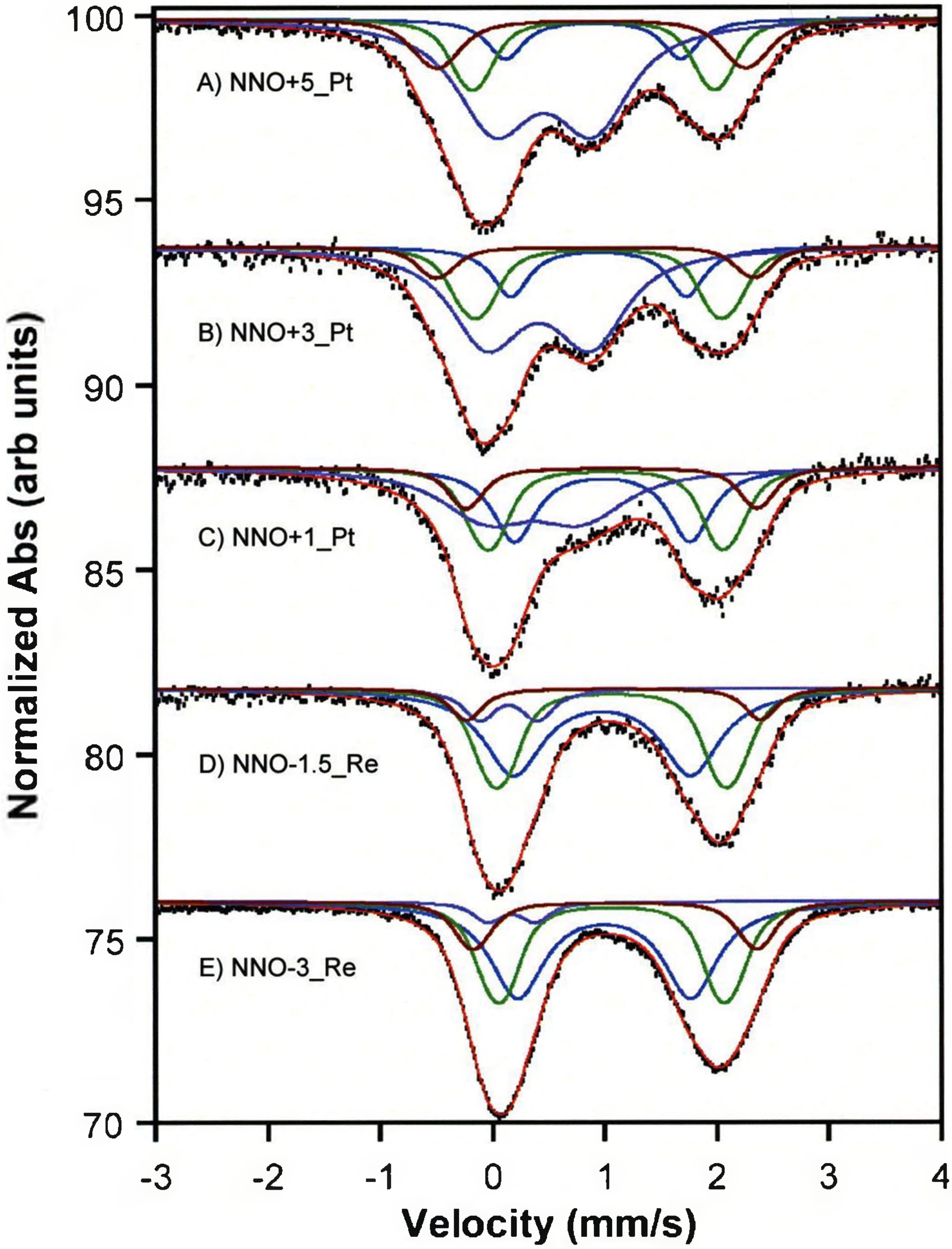

Figure 2: Fitted Mössbauer spectra for A) NNO+5_Pt, B) NNO+3_Pt, C) NNO+1, D) NNO-1.5_Re, E) NNO-3_Re, F) NNO_3_dPt, G) NNO-1.5_dPt, and H) NNO+3_dPt. The fitted doublets represent the following Fe coordinations: $^{IV}Fe^{2+}$ is blue, $^{IV\text{-}VI}Fe^{2+}$ is green, $^{IV\text{-}VI}Fe^{2+}$ is maroon, and $^{VI}Fe^{3+}$ is purple.

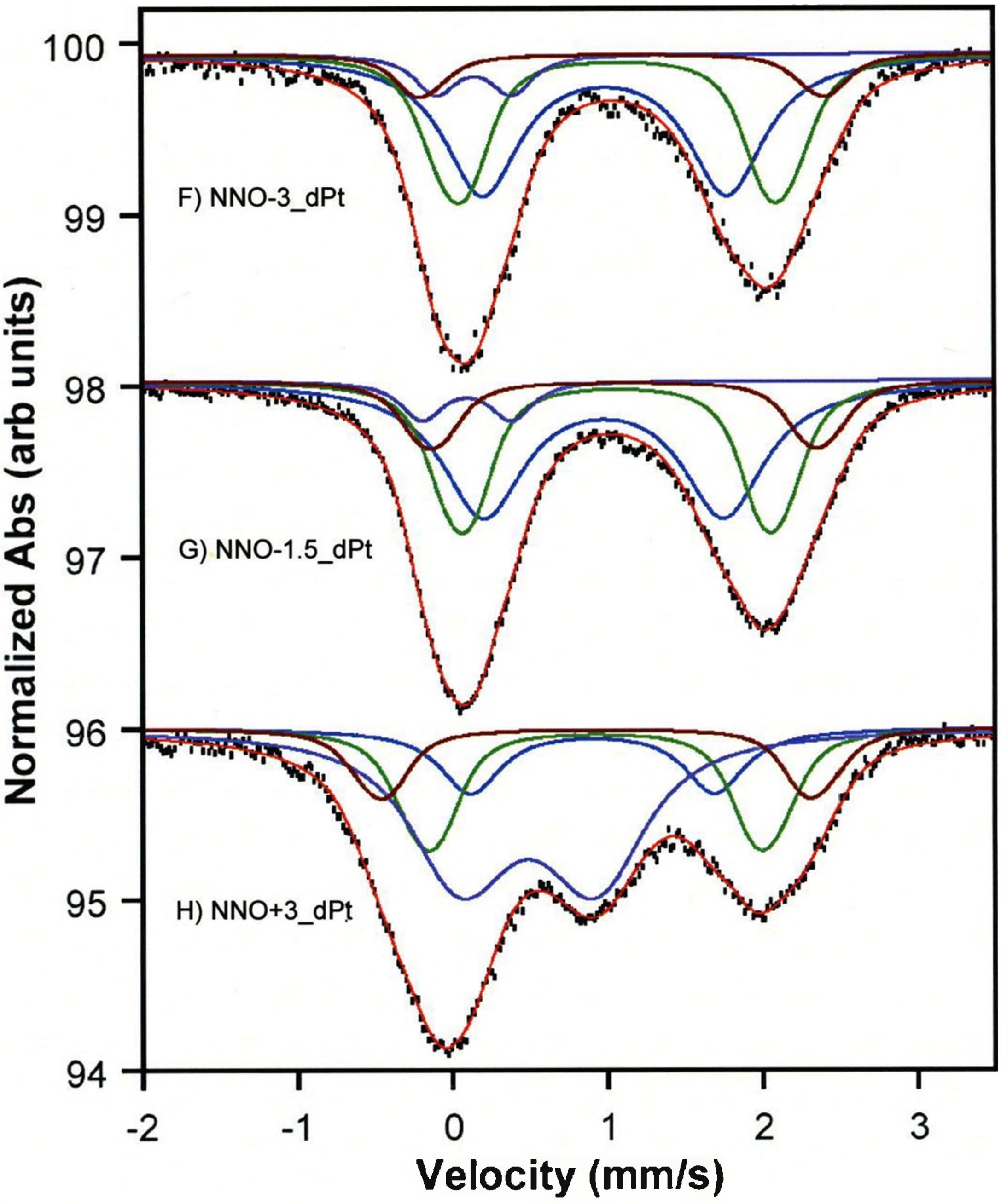

Figure 2 Continued.

Table 4: Mössbauer parameters (widths, Γ, isomer shifts, δ, and quadrupole splittings, Δ) from Dr. M. Darby Dyar, Mt. Holyoke College, MA, USA.

		NNO+ 5_Pt	NNO+ 3_Pt	NNO+ 3_dPt	NNO+ 1_Pt	NNO- 1.5_Re	NNO- 1.5_dPt	NNO- 3_Re	NNO- 3_dPt
$^{IV}Fe^{2+}$	δ(mm/s)	0.92	0.96	0.90	0.99	0.98	0.98	1.00	0.99
	Δ(mm/s)	1.56	1.55	1.56	1.56	1.57	1.55	1.54	1.57
	Γ(mm/s)	0.39	0.39	0.47	0.46	0.64	0.64	0.58	0.59
	Area(%)	11	15	14	27	47	46	46	48
IV-$^{VI}Fe^{2+}$	δ(mm/s)	0.92	0.96	0.92	1.02	1.07	1.06	1.06	1.07
	Δ(mm/s)	2.13	2.10	2.11	2.02	2.11	1.90	1.94	2.00
	Γ(mm/s)	0.30	0.30	0.30	0.30	0.30	0.30	0.30	0.30
	Area(%)	19.2	23.2	23	26	36	33	34	36
IV-$^{VI}Fe^{2+}$	δ(mm/s)	0.90	0.93	0.93	1.07	1.09	1.11	1.09	1.10
	Δ(mm/s)	2.73	2.87	2.71	2.56	2.63	2.57	2.57	2.67
	Γ(mm/s)	0.40	0.30	0.30	0.30	0.30	0.30	0.30	0.30
	Area(%)	16	9	13	12	9	14	15	9
$^{VI}Fe^{3+}$	δ(mm/s)	0.47	0.42	0.49	0.38	0.15	0.10	0.17	0.15
	Δ(mm/s)	0.96	1.01	0.95	1.01	0.50	0.58	0.42	0.48
	Γ(mm/s)	0.73	0.69	0.69	0.88	0.30	0.30	0.30	0.30
	Area(%)	54	53	51	35	9	7	5	7
	χ^2	1.49	1.39	1.34	1.38	1.61	2.05	2.61	1.61
	Fe^{3+}/Fe^{2+}	1.1742	1.0200	1.1279	0.5386	0.0753	0.0989	0.0526	0.0753

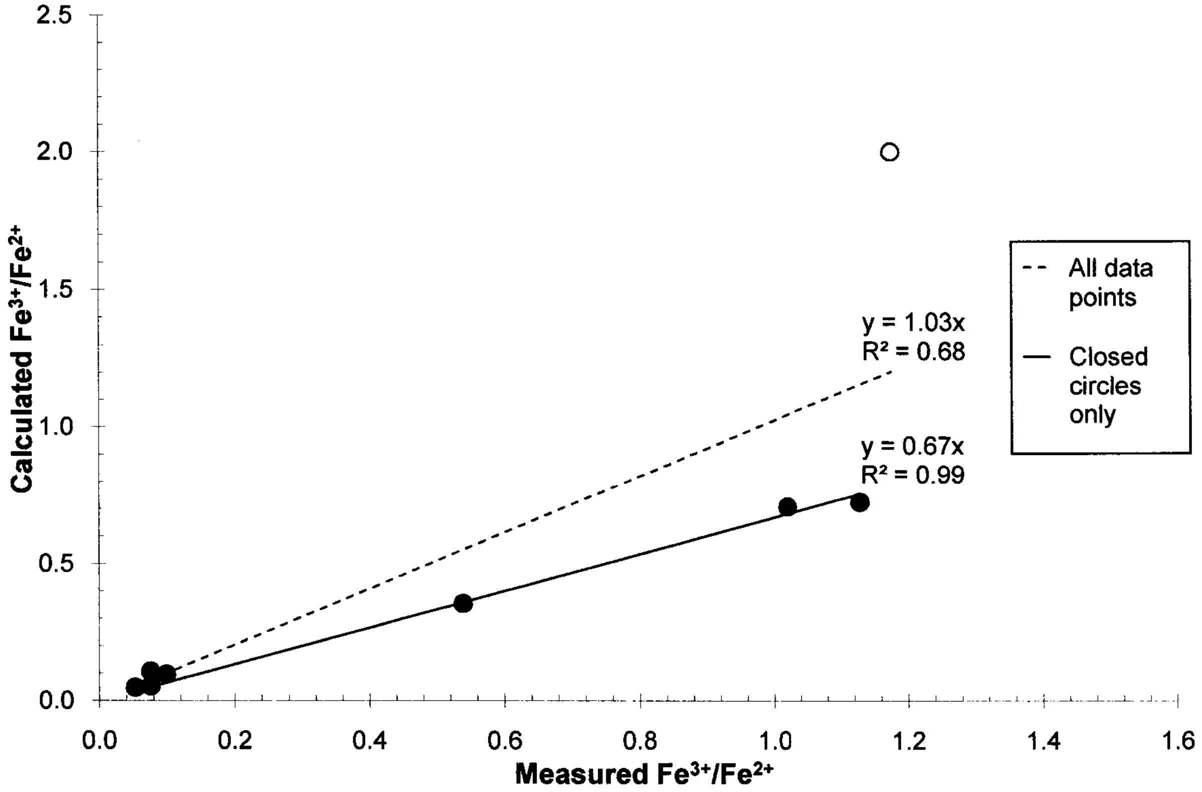

Figure 3: Plot of calculated Fe^{3+}/Fe^{2+} versus measured Fe^{3+}/Fe^{2+}. The open circle represents the samples synthesized at NNO+5 which is significantly higher than the expected trend that calculated values = measured values. The linear trend represented by the dashed line encompasses all data points while the linear trend represented by the solid line only considers data points that were synthesized below NNO+3.

4.4 Micro-reflectance Fourier transform infrared spectroscopy

Figure 4 shows the mid-IR μR-spectra for two glasses: NNO-3_dPt and NNO+5_dPt with compositions at the extremes of the synthesis f_{O_2}. Si-O troughs due to Si-O asymmetric stretching vibrations have minima located between 1220 and 1245 cm^{-1} for the 98 individual spot locations for the synthetic basaltic glasses in this study. A positive correlation was observed between the Si-O trough and the SiO_2 content of the basaltic glasses synthesized for this study (Figure 5). This correlation indicates that as SiO_2 increases the location of the reflectance trough shifts to higher wavenumbers. The positive linear correlation corresponds to an equation of Si-O trough location = 2.7* SiO_2 wt.% + 1092 (R^2 = 0.72). I note that atmospheric and dissolved H_2O and CO_2 (~3500 cm^{-1} and 2350 cm^{-1}, respectively) are below detection.

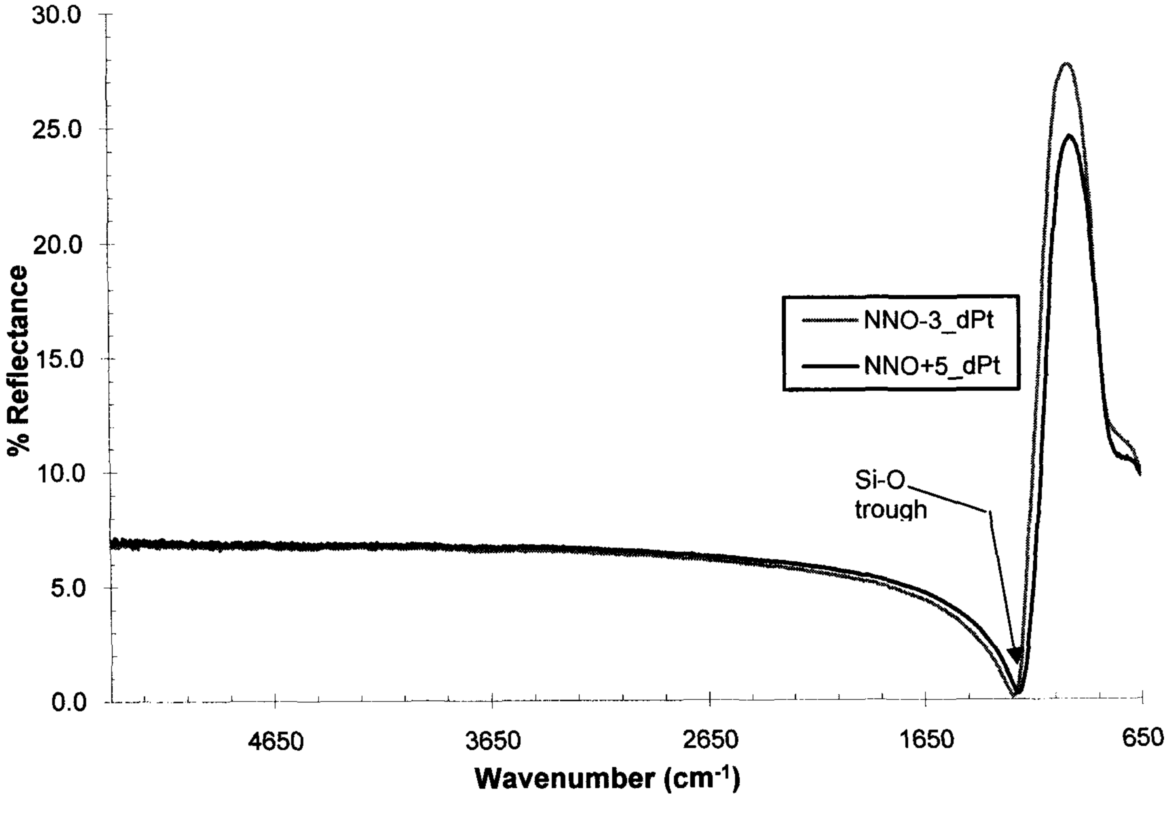

Figure 4: Micro-reflectance FTIR spectra for the two select synthetic basaltic glasses synthesized at the most extreme f_{O_2} showing the range of spectral shifts in this study.

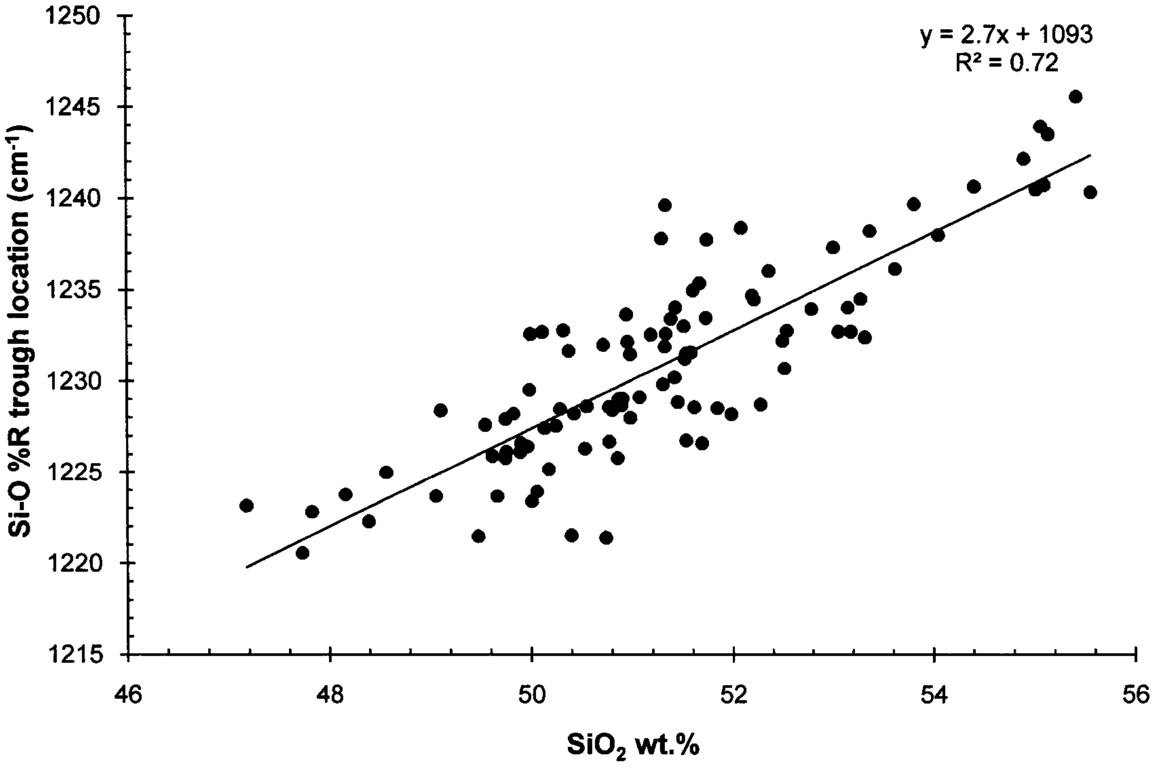

Figure 5: Plot of μR-FTIR Si-O trough location (%R) versus SiO_2 content for the 98 individual spot locations.

4.5 Kramers-Kronig transformed micro-reflectance Fourier transform infrared spectra

Figure 6 shows smoothed, baseline-corrected KK-absorbance spectra that have been cropped to 1300 – 800 cm^{-1} for the two glasses NNO-3_dPt and NNO+5_dPt whose μR-FTIR spectra were shown in Figure 4. Figure 6 demonstrates that the KK-absorption spectra show changes in both peak location and FWHM for compositions at the extremes of synthesis f_{O_2}. For the entire dataset, the Si-O peak maximum is located between 1031 and 1054 cm^{-1} and the FWHM of the Si-O peaks ranged from 188 to 235 cm^{-1}. Correlations with $R^2 \geq 0.64$ are observed between KK-absorption Si-O peak location and SiO_2, FeO_{total}, Mg#, or calculated refractive index, n, and correlations with $R^2 \geq 0.64$ are observed between FWHM and Na_2O or total alkalis (Table 3).

The Si-O peak location shows a positive correlation with the SiO_2 content of the glasses as seen from the correlation matrix, and similar to the μR-FTIR spectra (Fig. 7). As SiO_2 increases the peak location shifts to higher wavenumbers. The positive linear correlation corresponds to an equation of Si-O peak location = 2.0*SiO_2 wt.% + 938 (R^2 = 0.70). No correlation was observed between SiO_2 of the glasses and the FWHM of the peaks (Table 3).

Figure 8 shows the relationship between the Si-O peak location and FeO_{total} of the glasses. Because Fe correlated strongly with SiO_2 it is important to also account for SiO_2 content, as shown by the different symbols in Figure 8. This figure shows that the peak location shifts to higher wavenumbers as FeO_{total} decreases and SiO_2 increases. The linear correlation observed has an equation of Si-O peak location = -1.7* FeO_{total} wt.% + 1059 (R^2 = 0.71). Because Fe contributes to Mg# and both are correlated with SiO_2, a correlation is also observed between Mg# and Si-O peak location (Table 3).

The synthesized glasses have calculated Fe^{3+}/Fe^{2+} ranging from 0.027 to 2.001. To determine if there is a correlation between the Fe^{3+}/Fe^{2+} ratio and the Si-O peak location I investigated glasses with SiO_2 between 49.5 and 53.5 wt.% in 1.0 wt.% intervals (Fig. 9 A – D). Data points within the SiO_2 intervals were grouped according to FeO_{total} in order to limit FeO_{total} to less than 2.0 wt.% ranges within each data set. Figure 9 shows that each data set (A – D) falls within two standard deviations of their average Si-O peak location indicating that there is no dependence of the Si-O peak location on the Fe^{3+}/Fe^{2+}. No correlations were observed between the FWHM of the peaks and the FeO_{total}, Mg#, or Fe^{3+}/Fe^{2+} ratio of the glasses (Table 3).

Si-O peak location does not correlate with either Na_2O or total alkalis (Fig. 10 and Table 3). However, there are negative linear correlations between the FWHM and Na_2O (Fig. 11 and Table 3) as well as total alkalis (Fig. 12 and Table 3). Na_2O has a negative correlation corresponding to an equation of Si-O peak FWHM = -16*Na_2O wt.% + 233 (R^2 =0.86). Total alkali content exhibited a negative correlation corresponding to an equation of Si-O peak FWHM = -13*total alkali wt.% + 235 (R^2 = 0.92). Figure 12 shows that SiO_2 does not affect the relationship between total alkalis and FWHM. Figure 13 contains two spectra of similar SiO_2, Mg#, and peak location but different total alkali contents.

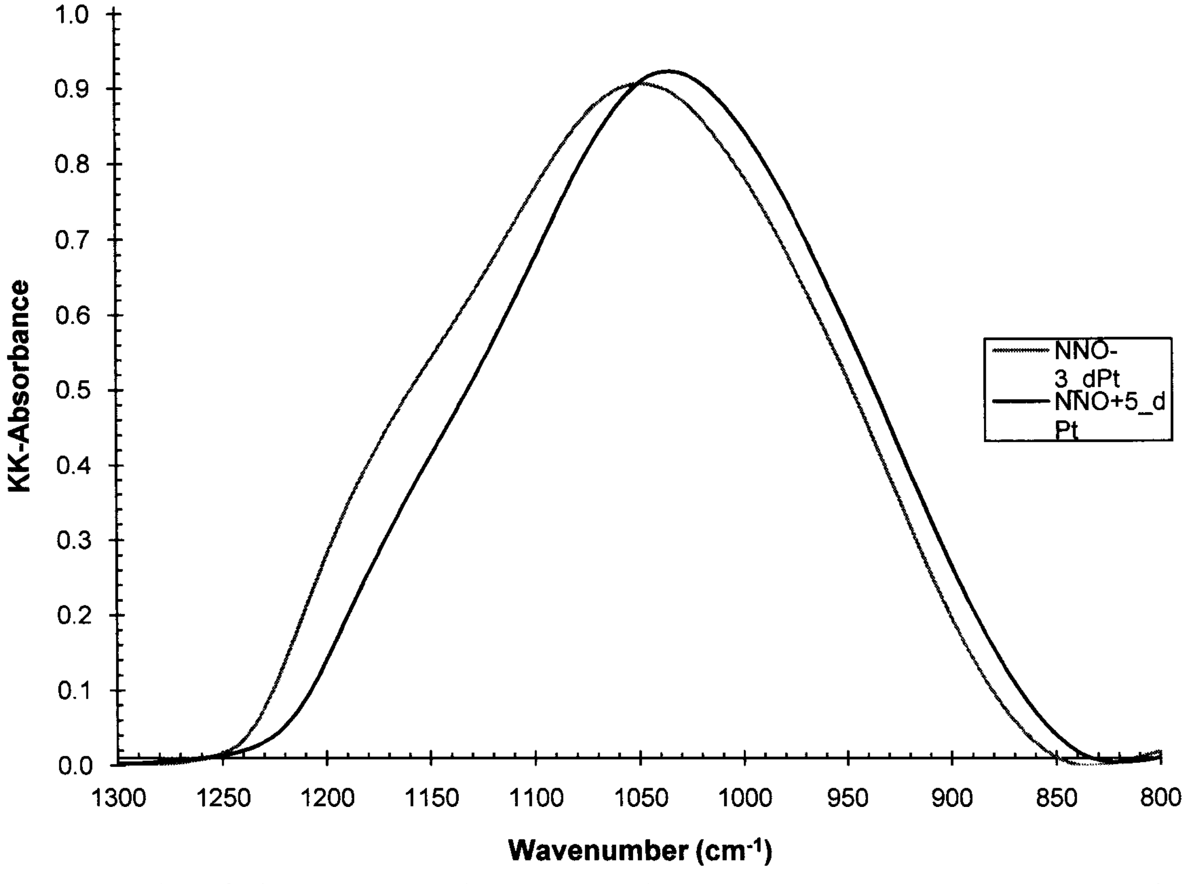

Figure 6: Plot of Si-O peak KK-absorbance values versus wavenumber for two synthetic basaltic glasses, NNO-3_dPt (grey) and NNO+5_dPt (black).

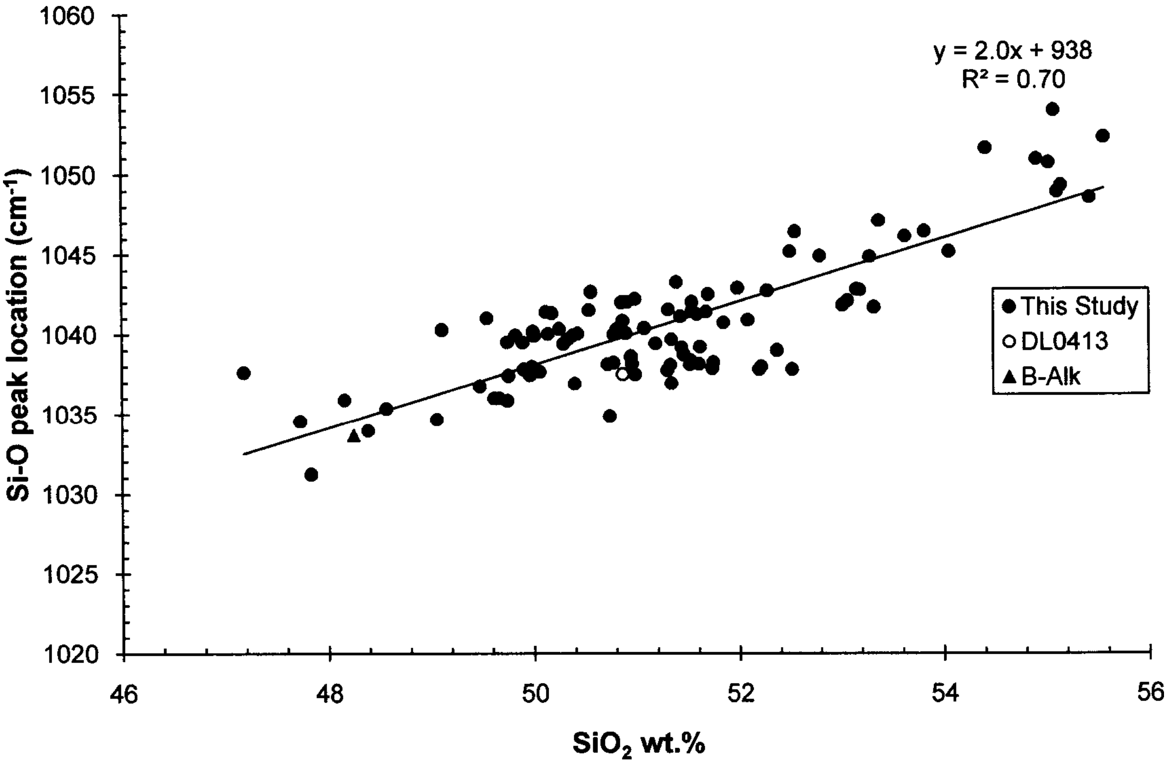

Figure 7: Plot of Si-O KK-abs peak location versus SiO_2 wt.% for 100 samples.

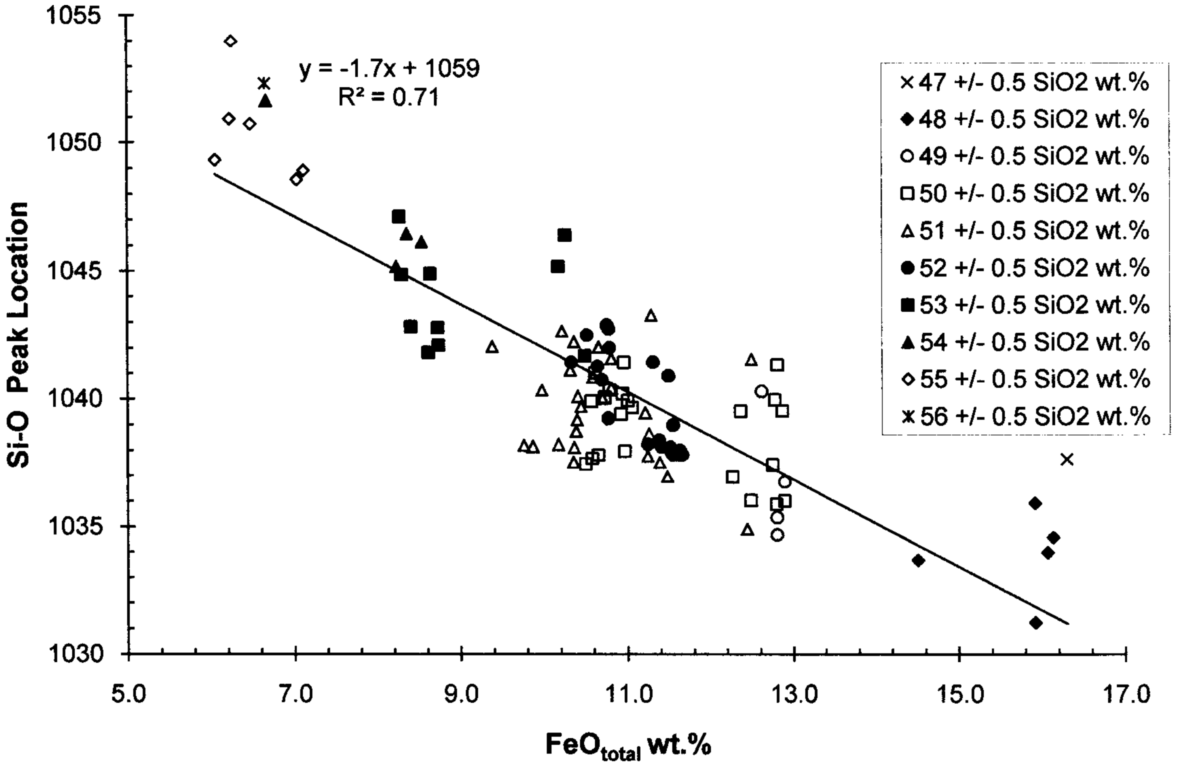

Figure 8: Plot of Si-O KK-abs peak location versus FeO_{total} wt.% for 100 samples considering SiO_2.

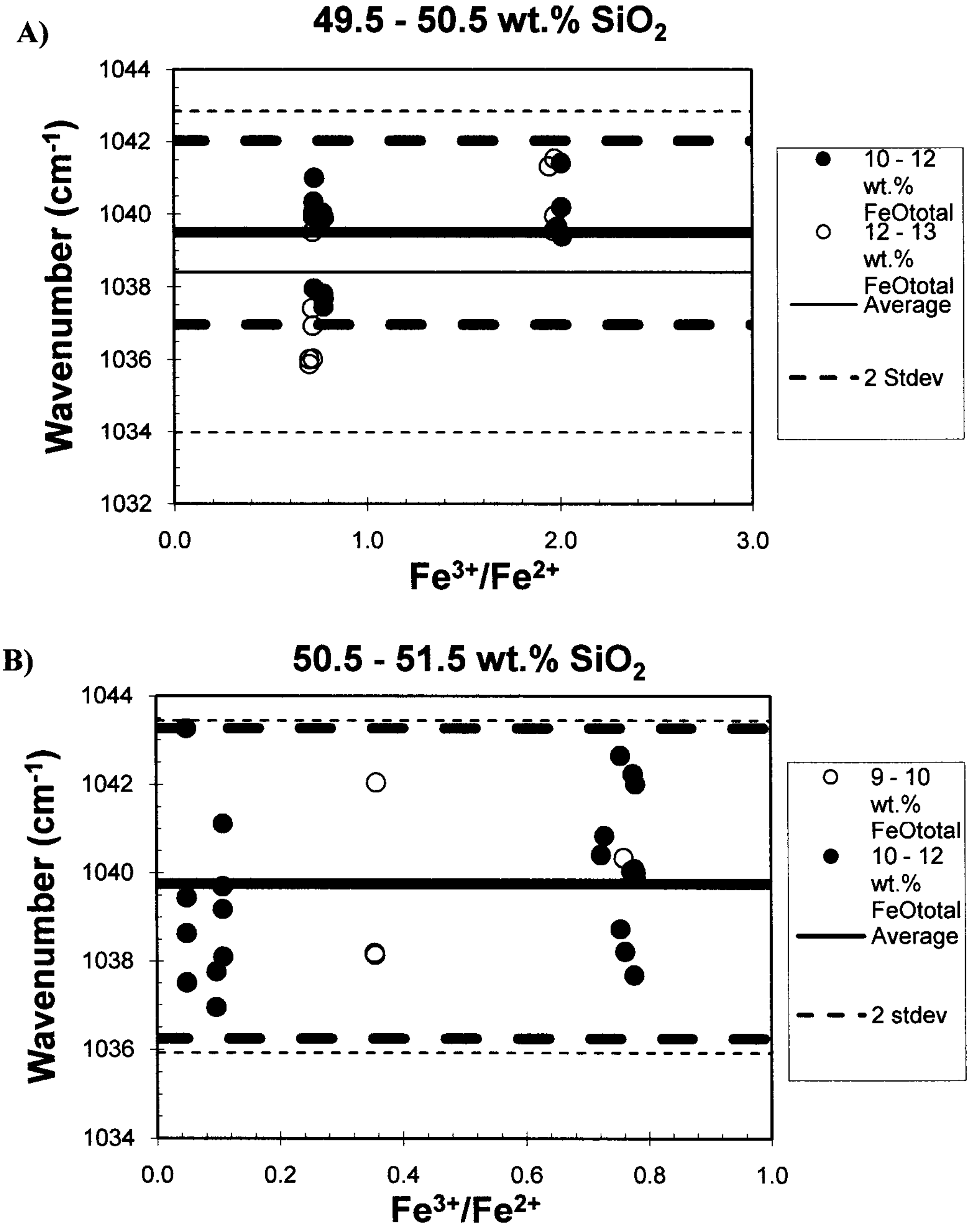

Figure 9: Plot of Si-O KK-abs peak location versus Fe^{3+}/Fe^{2+}. Four plots are shown in order to examine the data without compositional effects that could be caused by SiO_2 and FeO_{total}. A) Data for glasses with 50 ± 0.5 wt.% SiO_2 and 10 – 12 wt.% FeO_{total} (closed circles) or 12 – 13 wt.% FeO_{total} (open circles). B) Data for glasses with 51 ± 0.5 wt.% SiO_2 and 9 – 10 wt.% FeO_{total} (open circles) or 10 – 12 wt.% FeO_{total} (closed circles). C) Data for glasses with 52 ± 0.5 wt.% SiO_2 and 10 – 12 wt.% FeO_{total} (closed circles). D) Data for glasses with 52 ± 0.5 wt.% SiO_2 and 8 – 9 wt.% FeO_{total} (open circles) or 10 – 12 wt.% FeO_{total} (closed circles). Within each of the four plots the solid lines indicate the average peak location for the data set and dashed lines indicate a distance of two standard deviations away from the mean. The thicker lines represent the average and standard deviation for the solid symbols and the thinner lines are for the open symbols.

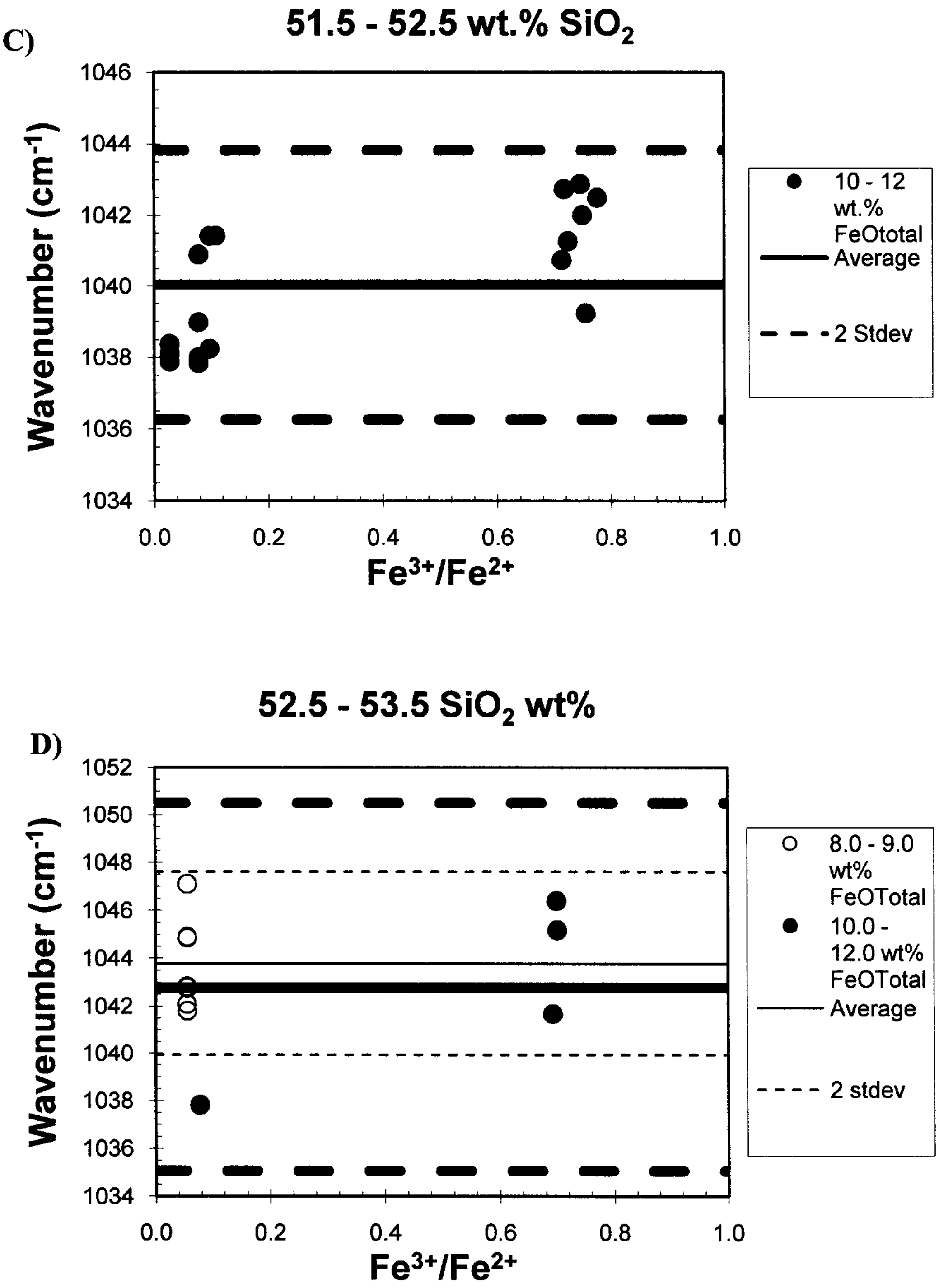

Figure 9: Continued.

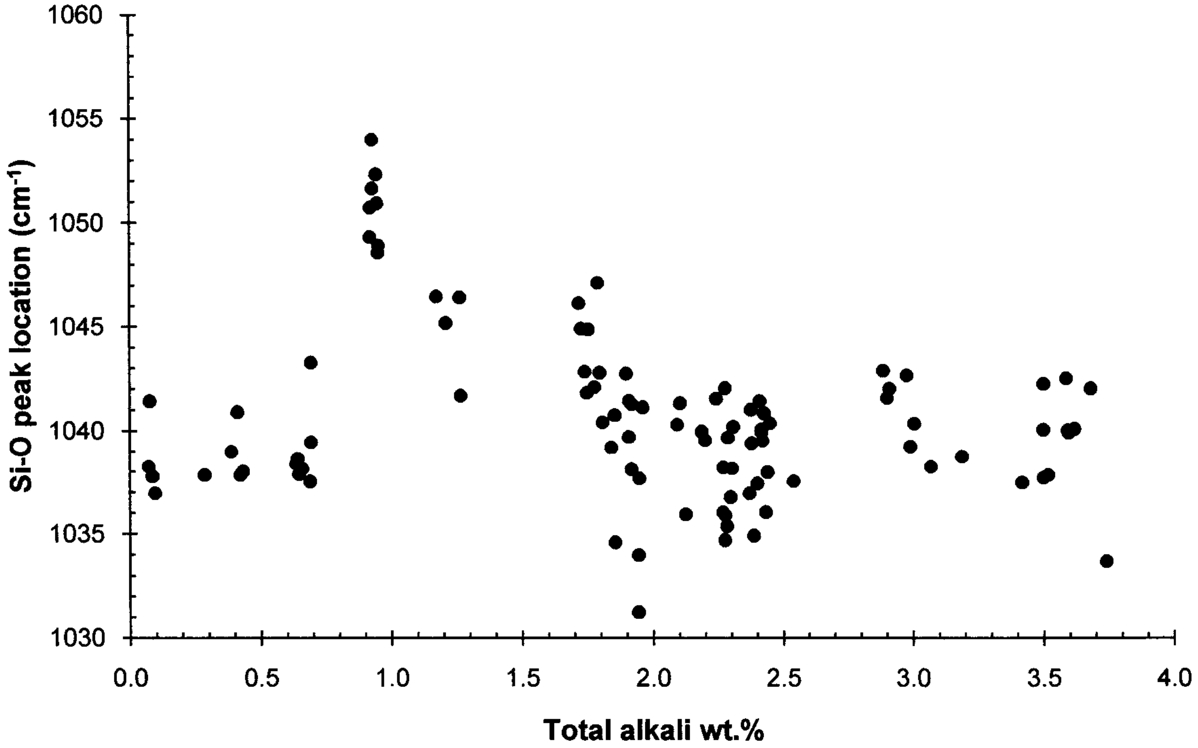

Figure 10: Plot of Si-O KK-abs peak location versus total alkali content.

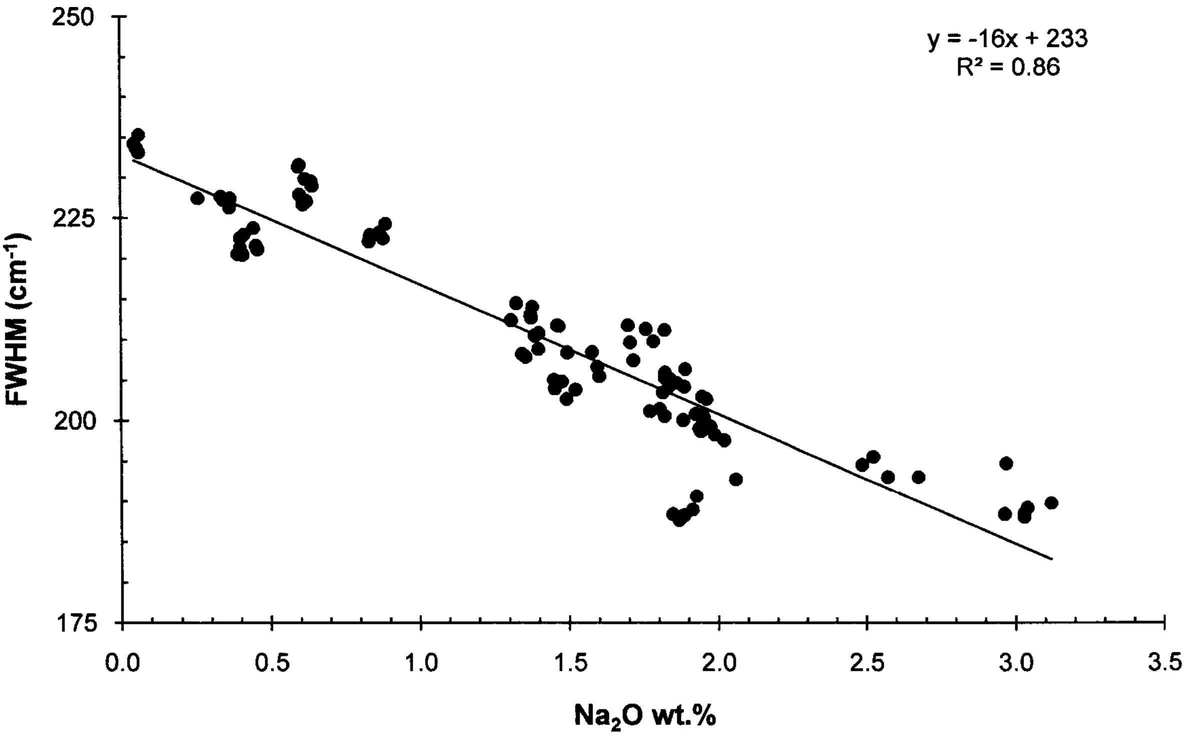

Figure 11: Plot of Si-O KK-abs FWHM versus Na_2O content.

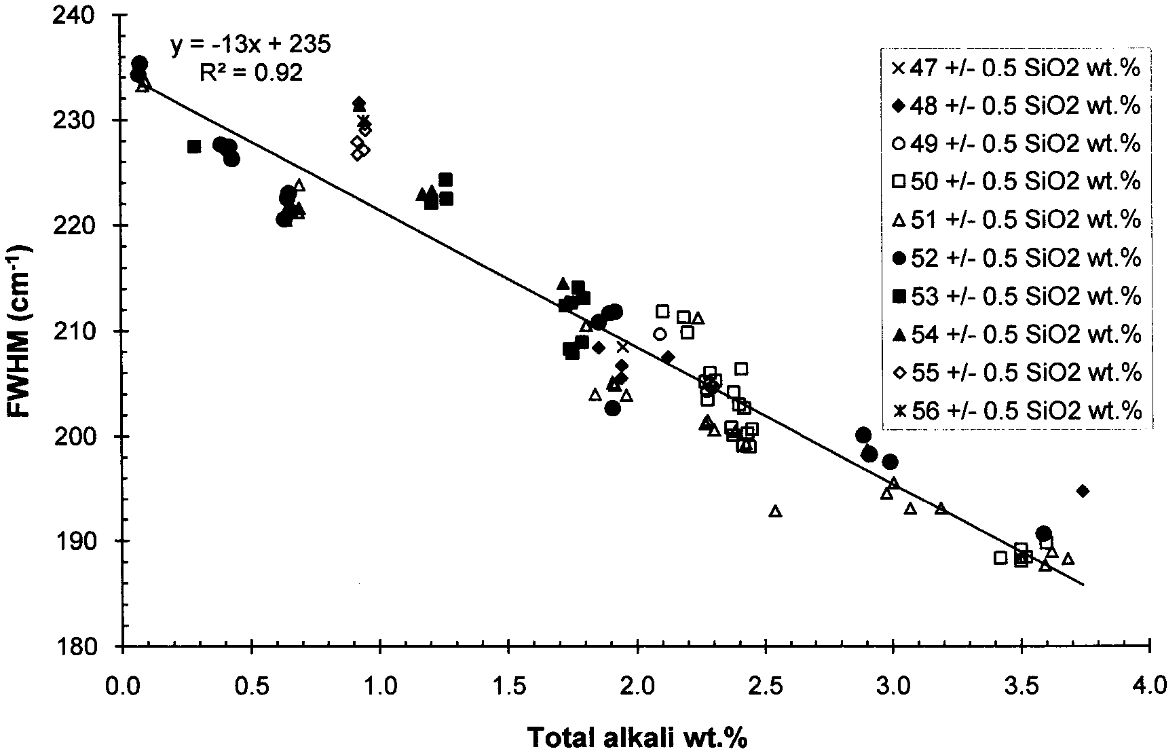

Figure 12: Plot of Si-O KK-abs FWHM versus total alkali content considering a constant SiO_2.

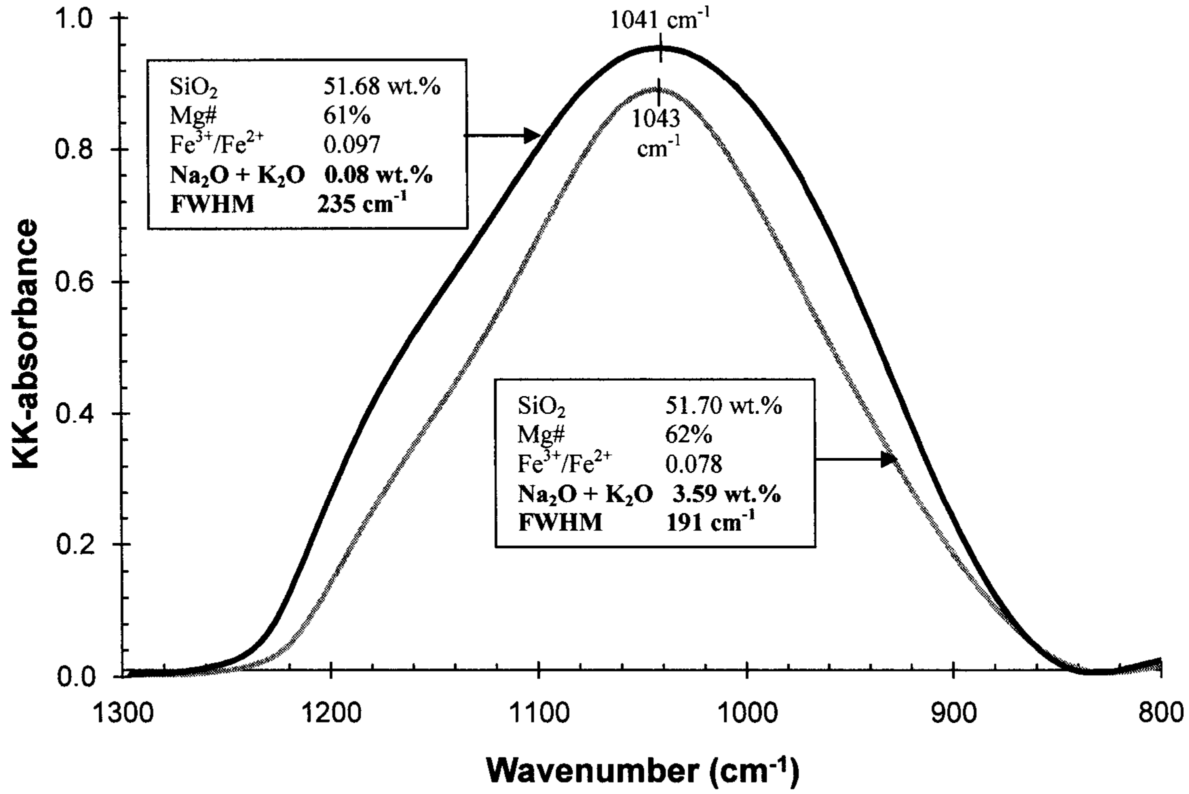

Figure 13: Comparison of two spectra of similar SiO_2, Mg#, and peak location but with varying total alkalis and Fe^{3+}/Fe^{2+}.

4.5 Calculated refractive indices

As indicated from the correlation matrix (Table 3) the calculated refractive indices of the glasses are correlated with the location of the Si-O asymmetric stretching vibrational KK-absorption peak.

5.0 Discussion

5.1 Bulk chemistry

This study provides, for the first time, a suite of tholeiitic glasses that have been examined for their chemistry and mid-IR signal. Approximately the same location in each synthetic glass chip was examined using IR and microprobe techniques. The spot size for the electron microprobe analyses, 10 μm diameter, is much smaller than the spot size used for the IR analyses, 100 μm by 100 μm. However, the difference in spot size is negligible because the average chemistry for individual glass pieces indicates that the glass pieces are homogeneous within microprobe error.

Another aspect of the bulk chemistry that was investigated was the Fe^{3+}/Fe^{2+} of the suite of glasses. As mentioned in the results section the calculated and measured Fe^{3+}/Fe^{2+} are expected to be similar because Kress and Carmichael (1988) stated that the melt should reach ferric/ferrous equilibrium when the synthesis duration was between 5 to 8 hours. My results indicate that measured Fe^{3+}/Fe^{2+} for glass (NNO+5) synthesized under the most oxidizing conditions deviated to a greater extent from the calculated values (Fig. 3). I attribute this observation to zoning of Fe^{3+}/Fe^{2+} within that glass because only 15 – 18 mg of glass was used to determine the measured Fe^{3+}/Fe^{2+}. Zoning within a glass could occur if the duration of the synthesis run did not provide a sufficient amount of time for the conversion of ferrous to ferric. The synthesis duration for the NNO+5 glass in which measured Fe^{3+}/Fe^{2+} was determined was only 5 hours. Therefore I speculate that if the synthesis duration were to increase the measured Fe^{3+}/Fe^{2+} would be more similar to the calculated Fe^{3+}/Fe^{2+}. It is also possible that the sample synthesized in air (NNO+5) may have a larger deviation (Fig. 3) because there was not a continuous flow of air through the furnace tube and the presence of still air may not have allowed the melt to equilibrate to the expected ratio.

5.2 Influence of glass composition on the Si-O peak

The shape and location of the Si-O feature varies as the bond angles and lengths within the silicate structure change because of the addition of network formers, such as Al^{3+} and Fe^{3+}, and network modifiers, such as Fe^{2+} and Na^{+} (e.g., review in King et al., 2004a). This occurs because the presence of network formers and modifiers affect bond angles and lengths within the silicate structure (Mysen and Richet, 2005). This study did not investigate every element within the silicate structure of basaltic glasses but has instead focussed on Fe and alkali contents.

My results show that the Si-O peak shifts position as the composition of basaltic glass is slightly changed. The SiO_2 content appears to be the major control on the position of the peak (Fig. 7). Other compositional parameters like Fe, Ca, and Mg# are also dependent on SiO_2 content in my dataset (Table 3), but do not appear to exert a major role on Si-O peak position when examined holding SiO_2 to within 1.0 wt.%. The FWHM of the Si-O band appears to be controlled by Na_2O and total alkali content of the basaltic glasses. The discussion below will include interpretations of the observed spectral changes and discuss these observations in context of other glasses.

5.3 Correlation matrix of basaltic glasses and a larger range of glass compositions

Within the results of this study I reported data that demonstrated correlations for basaltic glasses only. However from these results I cannot definitively say whether or not these correlations are true for only basaltic glasses or whether they are true for a large range of glass compositions. Therefore to help solve this dilemma data for the basaltic glasses was investigated in combination with eleven glasses analyzed by Dalby (2007) and an Fe-free basalt synthesized by Lockard (2005) using a correlation matrix (Table 5) and graphs (below). The matrix in Table 5 indicates that SiO_2 has $R^2 \geq 0.64$ with FeO_{total}, CaO, MgO, and calculated n. Correlations with $R^2 \geq 0.64$ are observed between KK-absorption Si-O peak location and SiO_2, FeO_{total}, and calculated n (Table 5). Other components that showed little correlation were omitted from Table 5. Some of the trends mentioned above, as well as trends that observed for the basaltic glasses only (Table 3) are discussed below.

Table 5: Correlation matrix, R^2 values, generated in Statview for 100 Fe-bearing basaltic glasses (This study; Lui, 2005; Oskarsson et al., 1982), one Fe-free basaltic glass (Lockard, 2005), and eleven other glasses of a large range in composition (Dalby, 2007). Data that show significant correlations are underlined and bold.

	KK-peak loc. (cm^{-1})	KK FWHM (cm^{-1})	SiO_2 wt.%	FeO wt.%	MgO wt.%	CaO wt.%	Na_2O wt.%	K_2O wt.%	Total alkali wt.%	Calculated refractive index, n
KK- peak loc. (cm^{-1})	1.00	0.14	0.89	0.72	0.59	0.53	0.20	0.11	0.22	0.78
KK FWHM (cm^{-1})	0.14	1.00	0.21	0.13	0.37	0.50	0.42	0.45	0.62	0.32
SiO_2 wt.%	**0.89**	0.21	1.00	0.75	0.65	0.69	0.26	0.16	0.31	0.87
FeO wt.%	**0.72**	0.13	**0.75**	1.00	0.55	0.48	0.32	0.21	0.38	0.84
MgO wt.%	0.59	0.37	**0.65**	0.55	1.00	0.84	0.63	0.30	0.67	0.86
CaO wt.%	0.53	0.50	**0.69**	0.48	**0.84**	1.00	0.57	0.45	0.75	0.84
Na_2O wt.%	0.20	0.42	0.26	0.32	0.63	0.57	1.00	0.14	0.74	0.51
K_2O wt.%	0.11	0.45	0.16	0.21	0.30	0.45	0.14	1.00	0.63	0.32
Total alkali wt.%	0.22	0.62	0.31	0.38	**0.67**	**0.75**	**0.74**	0.63	1.00	0.61
Calculated refractive index, n	**0.78**	0.32	**0.87**	**0.84**	**0.86**	**0.84**	0.51	0.32	0.61	1.00

5.4 Band fitting of the Si-O peak

To help determine why I observed narrowing of the Si-O peak as alkalis increased I applied a band fitting technique to the Si-O peak. Band fitting of the Si-O peak helps to determine which Si-O units are likely present within the structure and their relative abundance (Dalby and King, 2006). The technique of band fitting the mid-IR Si-O peak to determine the relative abundance of Si-O units was first applied by Dalby and King (2006) to $PbO-SiO_2$ glasses. The procedure they followed was to first take the second derivative of the Si-O peak, which provided approximate band locations. A program called PeakFit 4.0 was used to fit a series of Voigt-shaped bands, using the approximate locations from the second derivative, to the Si-O peak. Dalby and King (2006) found that the bands were in approximately the same location (within 10 cm^{-1}) every time. This fact and data from nuclear magnetic resonance and Raman spectroscopy allowed Dalby and King to assign Si-O units to the fitted bands. When the fit appeared to be accurate they examined the residuals and band fitting was considered successful if the fit produced by the bands was <0.02 KK-abs units different from the real Si-O peak.

Band fitting of the basaltic spectra in this study was done for two data sets: 51 ± 0.5 wt.% SiO_2 and 52 ± 0.5 wt.% SiO_2. These two data sets contain a large amount of data points and large ranges in alkalis and f_{O_2}. Using the band locations provided by Dalby (2007) for aluminosilicate glasses I fit bands to the Si-O peak. Figure 14 shows a representative band fitted spectrum and residuals for a basaltic glass that contains 51.70 wt.% SiO_2, 62% Mg# and 3.59 total alkali wt.%. Band locations and amplitudes for the two datasets can be found in a data repository (Appendix C). Results from the band fitting will be discussed below with respect to SiO_2 and total alkali.

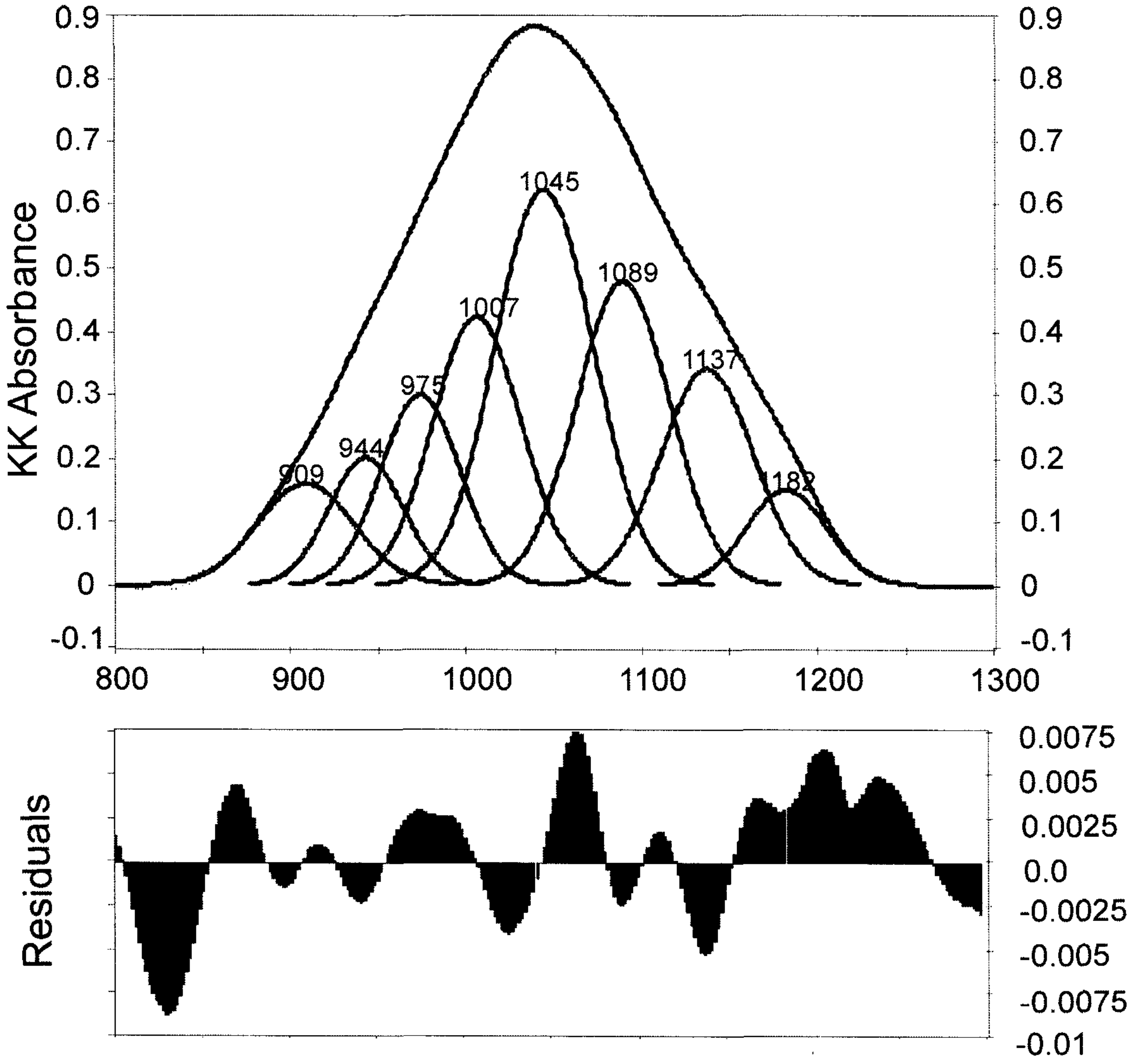

Figure 14: Representative example of band fitting of an Si-O peak (KK-absorbance units) and corresponding residuals. Fitted spectrum for a basaltic glass containing 51.70 wt.% SiO_2, 62% Mg#, and 3.59 total alkali wt.%.

5.5 Effect of SiO_2 on mid-infrared spectra

This study confirms the expected correlation between the Si-O peak location and the SiO_2 content of basaltic glasses (Fig. 7). When the basaltic glasses are compared to the glasses studied in Dalby (2007) and an Fe-free basalt (Lockard, 2005) I see that all of the glasses show a correlation between peak location and SiO_2 (Fig. 15), as previously shown by Dalby (2007). However, this study shows that there is essentially no correlation between SiO_2 of any of the glasses and the FWHM of the peak (Table 4 and Table 5). This finding indicates that even though the position of the peak is controlled by SiO_2 it has little impact on the shape, or FWHM, of the peak. Studies by Dalby and King (2006) and Dalby (2007) showed that the percent amplitude of some of the bands representing Si-O units vary systematically as SiO_2 changes. In this study I investigated the amplitude of each band in order to avoid normalizing the band amplitudes as a percentage (Appendix C). Within the SiO_2 range investigated, 51.5 ± 1.0 wt.%, I observe a positive linear correlation between band amplitude and SiO_2 in all but one band (1050 cm^{-1}). The band amplitude is related to SiO_2 by a factor of ~0.019 (average) with most bands within one standard deviation of the average (Fig. 16). Two of the bands, located at 1180 cm^{-1} and 1050 cm^{-1}, are within two standard deviation of the average slope, 0.019 ± 0.029, indicating that they are slightly more affected by changes in SiO_2. Since the slopes for all of the bands are within two standard deviations of the average slope I suggest that within a 2.0 wt.% SiO_2 range that all of the bands change by approximately the same amount. This finding further suggests that the Si-O units in the glass all increase equally as SiO_2 increases.

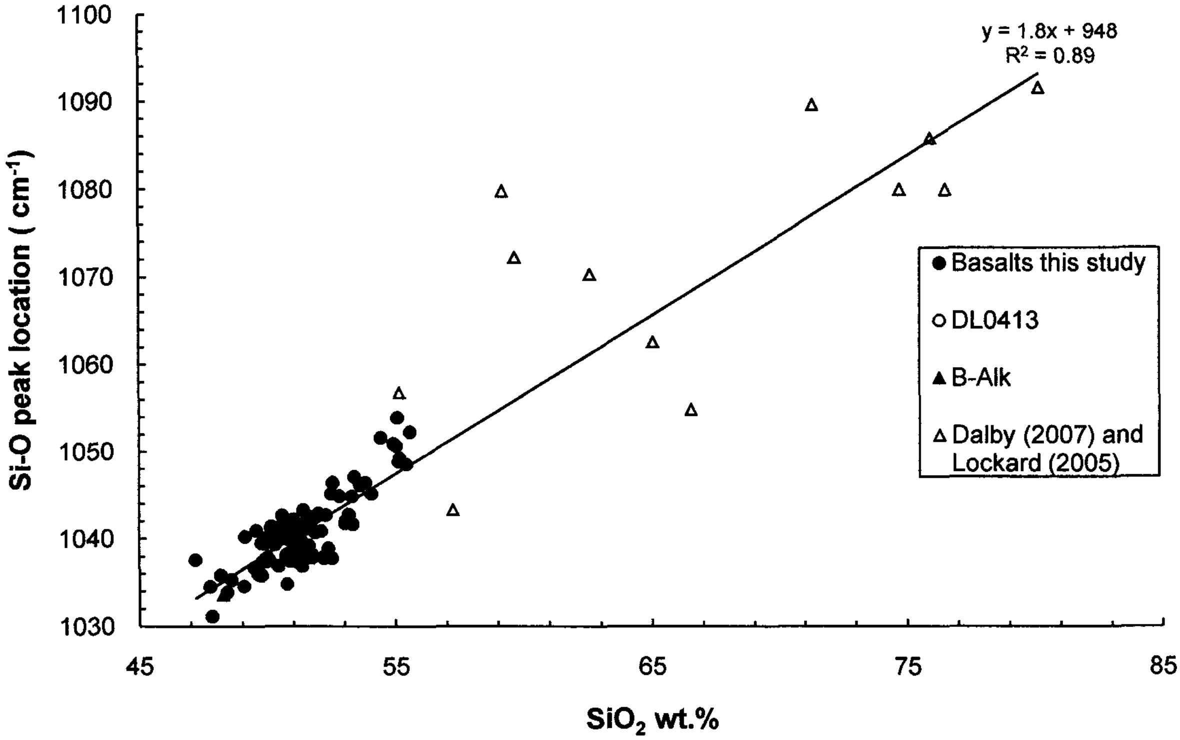

Figure 15: Plot of Si-O peak location versus SiO_2 content for the basaltic glasses presented in the results (open and closed circles, as well as the closed triangle) and glasses presented by Dalby (2007) and Lockard (2006) (open triangles).

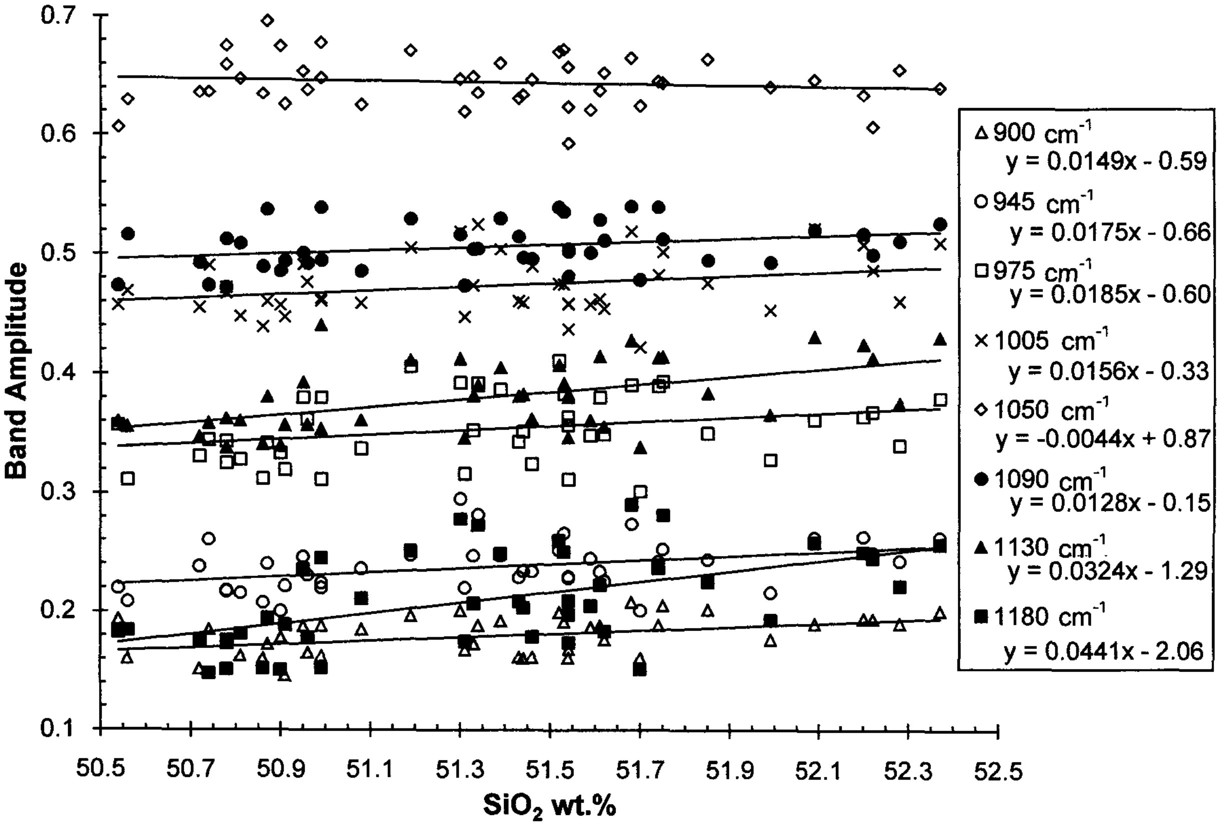

Figure 16: Plot of Si-O unit band amplitudes versus SiO_2 content.

5.6 Effect of FeO_{total} and Fe^{3+}/Fe^{2+} on mid-infrared spectra

The effect of Fe on the mid-IR spectra of basaltic glasses was investigated in this study because previous studies have stated that Fe might play the role of a network modifier and/or a network former within the silicate structure (Henderson, 2005; Jackson et al., 2005; Mysen and Richet, 2005; Wilke et al., 2006). Since Fe is divalent I must consider both the affects of Fe^{3+} and Fe^{2+} on the silicate system. A network former has a similar charge and ionic radius as Si^{4+} and becomes part of the silicate framework by replacing a Si^{4+} tetrahedra, which changes the bond lengths and angles within the structure (Mysen and Richet, 2005). Fe^{3+} may act as a network former when it is four-fold coordinated but it may act as a network modifier if it is in a higher coordination, such as six-fold (Henderson, 2005; Mysen and Richet, 2005). Network modifiers decrease polymerization by promoting non-bridging O atoms and therefore help to join silicate networks together (Mysen and Richet, 2005). In contrast, Fe^{2+} is an example of a network modifier (Mysen and Richet, 2005) that is commonly found in four- or five-fold coordination (Jackson et al., 2005; Wilke et al., 2006). From these studies I would expect to see a change in the silicate framework as the amount of FeO_{total} changes and as the ferric/ferrous changes. However, this study shows that mid-IR spectra is not sensitive enough to show changes induced by FeO_{total} content or Fe^{3+}/Fe^{2+}.

Results when comparing the basaltic glasses to the other glasses analyzed by Dalby (2007) and an Fe-free basalt (Lockard, 2005) confirm that there is a correlation between FeO_{total} and the Si-O peak but also shows a correlation between FeO_{total} and SiO_2 (Table 5). Therefore I propose that the location of the Si-O peak is not significantly affected by the FeO_{total} of the silicate glasses rather it is influenced by the SiO_2 as mentioned above.

When the expected Fe^{3+}/Fe^{2+} and the Si-O peak in the mid-IR was investigated while holding SiO_2 and FeO_{total} constant (Fig. 9) there appears to be no correlation. All of the KK-absorbance peak locations fell within two standard deviations of the average KK-absorption peak location. In contrast, I would have expected to observe the Si-O peak location shift to higher wavenumbers as the Fe^{3+}/Fe^{2+} decreases since this change in composition decreases polymerization (Dalby et al., 2006). I conclude that the mid-IR spectra of silicate glasses is not sufficiently sensitive to changes in Fe^{3+}/Fe^{2+} to record this information. Therefore in order to gain knowledge of the expected Fe^{3+}/Fe^{2+} ratio one must obtain spectra from the UV-visible-near-IR regions where features specifically attributed to Fe electronic transitions are present (Bell and Mao, 1976; Kakkadapu et al., 2003).

5.7 Effect of alkali on mid-infrared spectra

The relationship between total alkalis and the Si-O feature in the mid-IR spectra was investigated because Na and K, the two alkalis present in basaltic glasses, become incorporated into the silicate structure as network modifiers. The Na_2O and total alkalis are correlated with the FWHM of the Si-O peak (Table 3; Figs. 11 and 12) indicating that alkalis affect the silicate structure of the basaltic glasses. Since the correlation between the FWHM and total alkalis is slightly better than Na_2O alone I will focus my discussion on the effects caused by total alkalis. My observations indicate that as total alkalis decrease the FWHM of the Si-O feature increases (Fig. 12). In contrast the SiO_2 content of the suite of glasses is not correlated with the FWHM and the alkali content of the basaltic glasses (Table 3 and Fig. 12).

Upon investigation of the Si-O peak amplitudes versus total alkali content I determined that there is no correlation between the observed Si-O peak amplitude and the total alkali content of the basaltic glasses (Fig. 17A). However, since a change in FWHM was apparent in the spectra band fitting results were plotted versus the total alkali content of the basaltic glasses to determine if any trends are present. My band fitting results for samples with $SiO_2 = 51 \pm 0.5$ wt.% and $SiO_2 = 52 \pm 0.5$ wt.% indicate that the amplitude of each band decreases as total alkali wt.% increases, with the exception of the 1050 cm^{-1} band (Figs. 17B and 17C). For the 51 ± 0.5 wt.% SiO_2 dataset, the 1050 cm^{-1} band has a slightly positive slope of 0.002. For the 52 ± 0.5 wt.% SiO_2 dataset, the 1050 cm^{-1} band had a slightly negative slope of -0.006. The slopes generated from the linear fits for plots of amplitude versus total alkali content are mostly within one standard deviation of the average slope (average = -0.015 for $SiO_2 = 51 \pm 0.5$ wt.%, and average = -0.018 for SiO_2 52 ± 0.5 wt.%). Bands at 1050 cm^{-1} and 1180 cm^{-1} for both data sets are within two standard deviations of average slopes (-0.015 ± 0.021 for the 51 ± 0.5 SiO_2 wt.% dataset, and -0.018 ± 0.017 for the 52 ± 0.5 SiO_2 wt.% dataset), which are the same bands that deviated to a greater extent for SiO_2 (Fig. 16). In comparison to the average slope, the band at 1050 cm^{-1} has a shallower slope and the band at 1180 cm^{-1} has a steeper slope. Since the slopes for all of the bands are within two standard deviations of the average slope I am able to conclude that the Si-O units of the Si-O peak change in approximately the same amount as total alkalis change.

Because FWHM correlates negatively with the total alkalis of the basaltic glasses, I also examined these variables for other glasses (Dalby, 2007; Lockard, 2005). There does not appear to be a strong correlation between FWHM and alkali content when all of the glasses are investigated (Fig. 18 and Table 5). However it is important to note that some of the spectra provided by Dalby (2007) contained shoulders on the Si-O peak. This would in turn affect the FWHM of the Si-O peak, which may be why we do not observe a correlation. From the results presented I conclude that the FWHM of the Si-O peak may be used to determine the total alkali content of basaltic glasses but the technique is not applicable to other glasses, until further investigation is conducted.

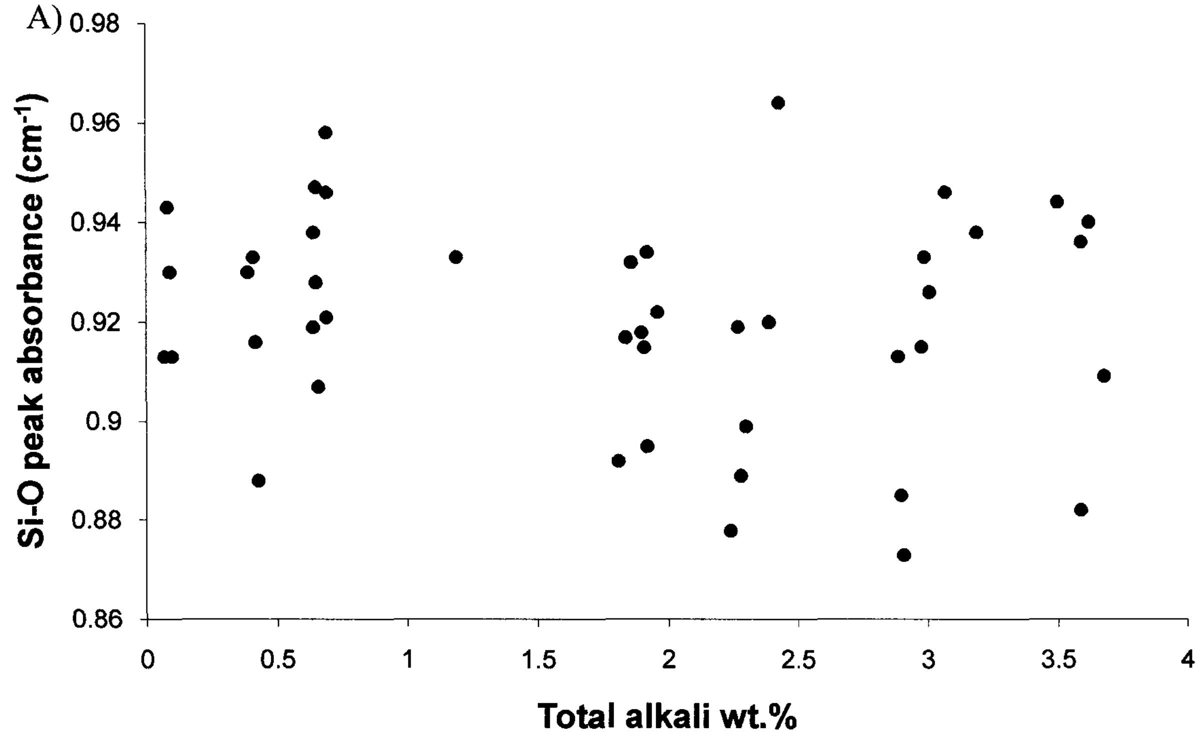

Figure 17: A) Plot of Si-O peak amplitude versus total alkali content for data within the range of 50.5 – 52.5 wt.% SiO_2. Plot of Si-O unit band amplitudes versus total alkali content for two datasets: B) 51 ± 0.5 wt.% SiO_2 and C) 52 ± 0.5 wt.% SiO_2.

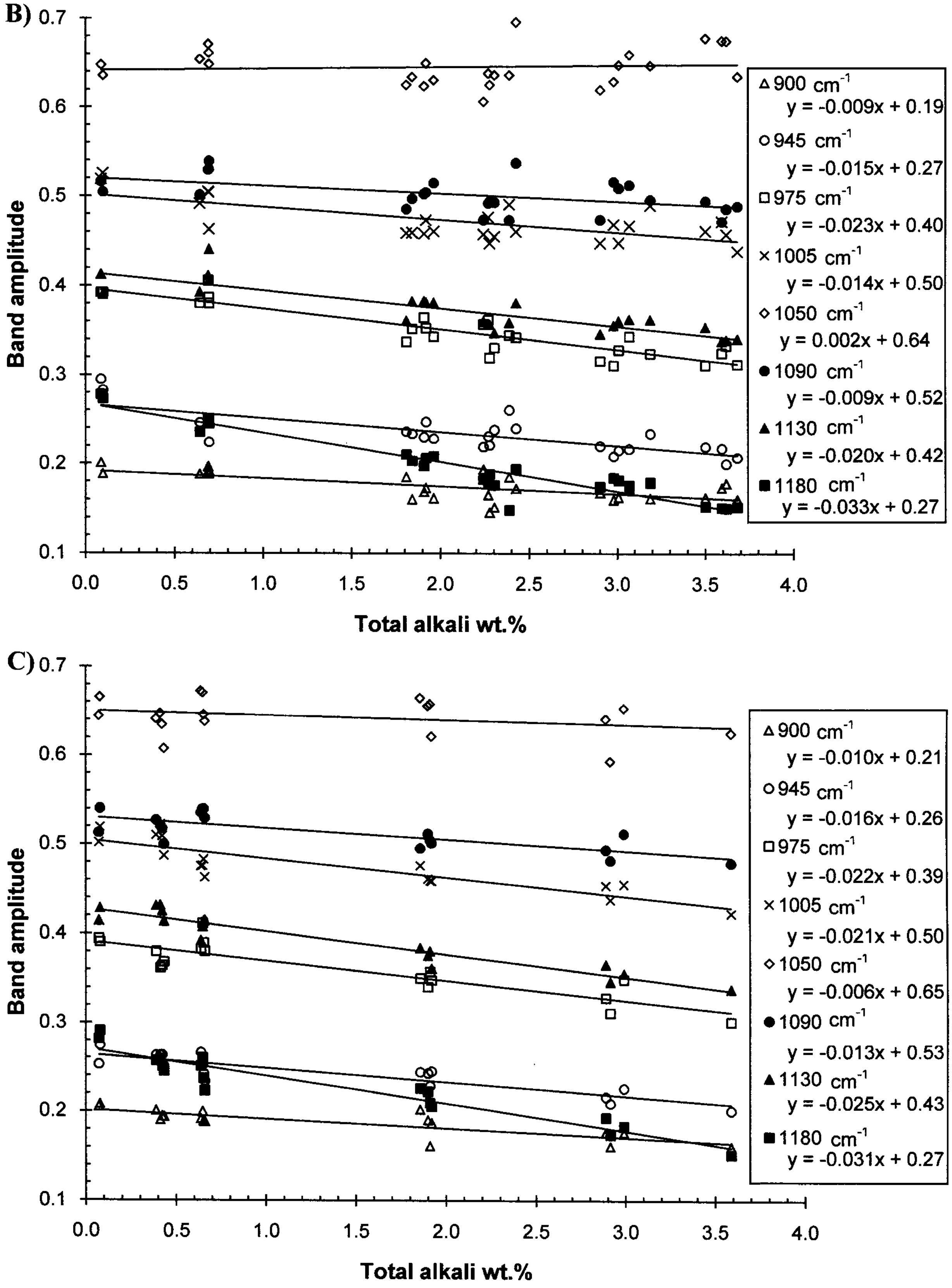

Figure 17: Continued.

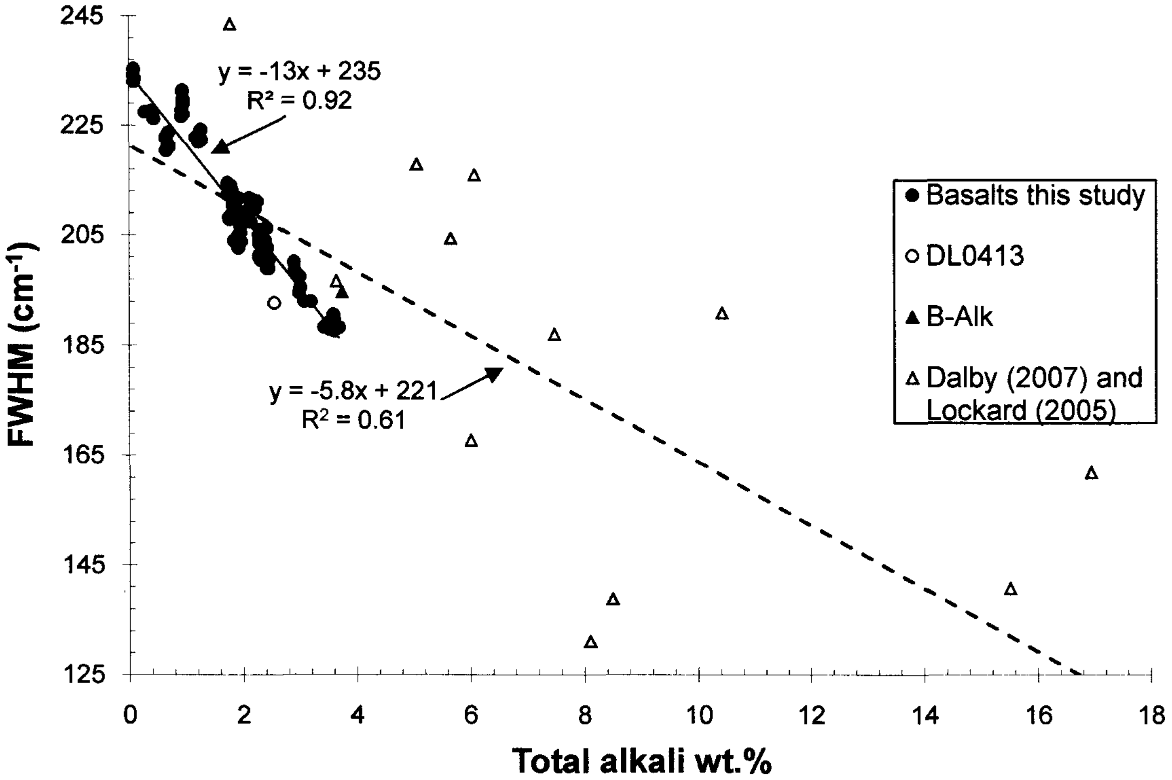

Figure 18: Plot of FWHM versus total alkali content for the basaltic glasses presented in the results (open and closed circles, as well as the closed triangle) and the glasses presented by Dalby (2007) and Lockard (2005) (open triangles). The solid line represents the fit through the basaltic glasses only and the dashed line represents the fit through all data points.

5.8 Application to infrared remote sensing

From the obtained results I speculate that the SiO_2 content may be approximated using the Si-O peak location and that the total alkali content of remotely sensed basaltic glass may be determined using the FWHM. Interestingly, FeO_{total} and Fe^{3+}/Fe^{2+} do not affect the mid-IR spectra of basaltic glasses; this means that SiO_2 and alkali content may be determined for basaltic glasses with a wide range of Mg#. Other components within basaltic glasses appear to have little to no observable effect on the shape or position of the Si-O peak for basaltic glasses (Table 3).

As mentioned earlier a study by Byrnes et al. (2007) indicate that the specular reflectance maxima are very similar to minima measured for emission spectra of the same glassy material (Byrnes et al., 2007). Thus I suggest that similar locations are expected for specular reflectance and emission spectra of basaltic glasses. Futhermore, if emission data were treated with a KK-transform to remove the refractive index effects then I should observe very similar changes to those outlined in this study.

The observation that the Si-O peak for basaltic glasses shifts location when SiO_2 varies and that the FWHM changes with respect to total alkalis may help when using basaltic glass as an endmember in spectral libraries. Generally, remotely sensed spectra are interpreted through spectral deconvolution using a spectral library of selected endmembers. Currently most spectral endmember sets contain a few simple glass compositions, such as silica glass. The information presented in this study indicates that basaltic glass can be used as a spectral endmember irrespective of FeO_{total} and Fe^{3+}/Fe^{2+} (f_{O_2}).

5.9 Comparison with other basaltic glass spectra

My study focussed on changes in basalt IR spectra as a function of composition. In contrast other studies have presented spectra for glass-mineral mixtures (Crisp et al., 1990; Johnson et al., 2007; Minitti et al., 2005; Minitti et al., 2002)and glass composition has not been reported. My results show the importance of characterizing the glass composition because even subtle changes in SiO_2 and alkalis affect the mid-IR spectra. In the introduction I mentioned studies by Johnson et al. (2007), Minitti et al. (2002; 2005), and Crisp et al. that investigate changes in basaltic spectra. However, I cannot apply my observation directly to their spectra because there are minerals present in most of their samples that were analyzed, and the bulk composition for the samples are not given. It is only possible to make a comparison between my observations and those found by Minitti et al. (2002; 2005) because the shocked basaltic spectra presented by Johnson et al. (2007) contain a maximum of 31% glass and the Si-O peak presented by Crisp et al. obtains shoulders. For example, this study and the studies by Minitti et al. (2002; 2005) observed narrowing of the Si-O feature. I attribute narrowing of the Si-O peak to an increase in alkali content in the glass, whereas Minitti et al. (2002; 2005) attributed this trend to the presence of hematite on the surface of basaltic glasses. Therefore in order to distinguish between these two interpretations for the narrowing of mid-IR spectra of basaltic glasses you should investigate the degree of narrowing and see if it fits within the trend stated in Figure 12.

6.0 Conclusions

The results of this study are significant because they provide information that will help to better constrain mid-IR spectra of basaltic glasses and will aid in determining compositions of basaltic glasses in dangerous and remote areas. Constraints for SiO_2 and alkali contents may help improve spectral databases by providing information that justify using basaltic glass as a spectral endmember since certain compositional effects can be predicted from the spectra. This study shows that the Si-O peak shifts to higher wavenumbers as SiO_2 content increases and the FWHM decreases as total alkalis increase. This study is the first to show the effects of total alkalis on a complex silicate system. I observed that Si-O peak FWHM = -13*total alkali wt.% + 235. This study also shows that FeO_{total} and Fe^{3+}/Fe^{2+} do not affect mid-IR spectra. Instead, other spectral ranges or analytical techniques must be used in order to determine the relative composition of FeO_{total}, Fe^{3+}, and Fe^{2+} within silicate glasses. Although my study did not extend to extremely alkali compositions I would predict that remotely sensed mid-IR basaltic glasses could be classified as alkali basaltic or tholeiitic using Figure 1 and SiO_2 content derived from the peak location and alkali content derived from the FWHM.

7.0 References

Bandfield, J.R. (2002) Global mineral distributions on Mars. Journal of Geophysical Research, 107(E6), 9-1 - 9-20.

Bell, P.M. and Mao, H.K. (1976) Optical spectra and electron paramagnetic resonance of lunar and synthetic glasses: A study of the effects of controlled atmosphere, composition, and temperature. Proceedings Lunar Science Conference, VII, 2543-2559.

Bell, R.J., Bird, N.F., and Dean, P. (1968) The vibrational spectra of vitreous silica, germania and beryllium fluoride. Journal of Physics C: Solid State Physics, 1, 299-303.

Best, M.G. and Christiansen, E.H. (2001) Igneous Petrology. Blackwell Science, Inc., Malden, Massachusetts, 458 p.

Bézos, A., and Humler, E. (2005) The Fe^{3+}/Fe_{total} ratios of MORB glasses and their implications for mantle melting. Geochimica et Cosmochimica Acta, 69, 711-725.

Borisov, A. and Jones, J.H. (1999) An evaluation of Re, as an alternative to Pt, for the 1 bar loop technique: An experimental study at 1400°C. American Mineralogist, 84, 1528-1534.

Byrnes, J.M., Ramsey, M.S., King, P.L., and Lee, R.J. (2007) Thermal infrared reflectance and emission spectroscopy of quartzofeldspathic glasses. Geophysical Research Letters, 34, Article No. L01306 JAN 10 2007.

Carmichael, I.S.E. (1991) The redox states of basic and silicic magmas: a reflection of their source regions? Contributions to Mineralogy and Petrology, 106, 129-141.

Christensen, P.R., Bandfield, J.L., Smith, M.D., Hamilton, V.E., and Clark, R.N. (2000) Identification of a basaltic component on the Martian surface from Thermal Emission Spectrometer data. Journal of Geophysical Research, 105(E4), 9609-9621.

Christie, D.M., Carmichael, I.S.E., and Langmuir, C.H. (1986) Oxidation states of mid-ocean ridge basalt glasses. Earth and Planetary Science Letters, 79, 397-411.

Church, B.N. and Johnson, W.N. (1980) Calculation of the refractive index of silicate glasses from chemical composition. Geological Society of America Bulletin, 91, 619-625.

Corrigan, G., and Gibb, F.G.F. (1979) The loss of Fe and Na from a basaltic melt during experiments using the wire-loop method. Mineralogical Magazine, 43, 121-126.

Crisp, J., Kahle, A.B., and Abbott, E.A. (1990) Thermal infrared spectral character of Hawaiian basaltic glasses. Journal of Geophysical Research, 95(B13), 21657-21669.

Dalby, K.N. (2007) The structure of PbO and natural silicate glasses: An FTIR and XPS study. University of Western Ontario, Ph.D Thesis, Unpublished, 124.

Dalby, K.N., Dufresne, C.D.M., King, P.L., Byrnes, J.M., Lee, R.J., and Ramsey, M.S. (2006) Characterization of glasses using infrared spectroscopy. Geochimica et Cosmochimica Acta Supplement, 70(18), 125.

Dalby, K.N. and King, P.L. (2006) A new approach to determine and quantify structural units in silicate glasses using micro Fourier-Transform infrared spectroscopy. American Mineralogist, 91, 1783-1793.

Domine, F. and Piriou, B. (1983) Study of sodium silicate melt and glass by infrared reflectance spectroscopy. Journal of Non-Crystalline Solids, 55, 125-130.

Donaldson, C.H. (1975) A sample holding technique for study of crystal growth in silicate melts. American Mineralogist, 60, 324-326.

-. (1979) Composition changes in a basalt melt contained in a wire loop of $Pt_{80}Rh_{20}$: effects of temperature, time, and oxygen fugacity. Mineralogical Magazine, 43, 115-119.

Farrand, W.H. and Singer, R.B. (1991) Spectral analysis and mapping of palagonite tuffs of Pavant Butte, Millard County, Utah. Geophysical Research Letters, 18(12), 2237-2240.

Hall, A. (1996) Igneous Petrology. Longman, London, 551 p.

Henderson, G.S. (2005) The structure of silicate melts: a glass perspective. The Canadian Mineralogist, 43, 1921-1958.

Herd, C.D.K. (2006) Insights into the redox history of the NWA 1068/1110 martian basalt from mineral equilibria and vanadium oxybarometry. American Mineralogist, 91, 1616-1627.

Holloway, J.R. and Burnham, C.W. (1972) Melting relations of basalt with equilibrium water pressure less than total pressure. Journal of Petrology, 13, 1-29.

Jackson, W.E., Farges, F., Yeager, M., Mabroux, P.A., Rossano, S., Waychunas, G.A., Solomon, E.I., and Jr., G.E.B. (2005) Multi-spectroscopic study of Fe(II) in silicate glasses: Implications for the coordination environment of Fe(II) in silicate melts. Geochimica et Cosmochimica Acta, 69(17), 4315-4332.

Johnson, J.R., Staid, M.I., and Kraft, M.D. (2007) Thermal infrared spectroscopy and modelling of experimentally shocked basalts. American Mineralogist, 92, 1148-1157.

Kakkadapu, R.K., Li, H., Smith, G.L., Crum, J.D., Jeoung, J.-S., Poisl, W.H., and Weinberg, M.S. (2003) Mössbauer and optical spectroscopic study of temperature and redox effects on iron local environments in a Fe-doped (0.5 mol% Fe_2O_3) $18Na_2O$-$72SiO_2$ glass. Journal of Non-Crystalline Solids, 317, 301-318.

King, P.L., McMillan, P.F., and Moore, G.M. (2004a) Infrared spectroscopy of silicate glasses with application to natural systems. Infrared Spectroscopy in Geochemistry, Exploration Geochemistry and Remote Sensing, Mineralogical Association of Canada Special Volume 33, p. 93-133.

King, P.L., Ramsey, M.S., McMillan, P.F., and Swayze, G.A. (2004b) Laboratory Fourier transform infrared spectroscopy methods for geologic samples. Infrared spectroscopy: in geochemistry, exploration geochemistry, and remote sensing, Mineralogical Association of Canada Special Volume 33, p. 57-91.

Kress, V.C. and Carmichael, I.S.E. (1988) Stoichiometry of the iron oxidation reaction in silicate melts. American Mineralogist, 73, 1267-1274.

Kress, V.C. and Carmichael, I.S.E. (1991) The compressibility of silicate liquids containing Fe_2O_3 and the effect of composition, temperature, oxygen fugacity and pressure on their redox states. Contributions to Mineralogy and Petrology, 108, 82-92.

Le Maitre, R.W. (1989) A Classification of Igneous Rocks and Glossary of Terms. Blackwell Scientific Publications, London, U.K.

Lockard, J. (2005) The effects of iron-oxidation state on the weathering and bacterial colonization of basaltic glass. The University of Western Ontario, B.Sc. Honours thesis, unpublished.

Logan, L.M., Hunt, G.R., and Salisbury, J.W. (1975) The use of mid-infrared spectroscopy in remote sensing of space targets. In C. Karr Jr., Ed. Infrared and raman spectroscopy of lunar and terrestrial minerals. Academic Press, New York.

Lui, D.K. (2005) The Effects of Water on Basalt-Rhyolite Interactions in Volcanic Systems. University of Western Ontario, M.Sc. thesis, unpublished.

McMillan, P.F. and Hofmeister, A.M. (1988) Infrared and raman spectroscopy. In F.C. Hawthorne, Ed. Spectroscopy methods in mineralogy and geology, 18. Mineralogical Society of America, Blacksburg, VA.

Merzbacher, C.I. and White, W.B. (1988) Structure of Na aluminosilicate glasses: A far-infrared reflectance spectroscopic study. American Mineralogist, 73, 1089-1094.

Minitti, M.E., Hamilton, V.E., and Wyatt, M.B. (2007) Deconvolution of martian thermal infrared spectra using a simplified glass-rich library. Lunar Planetary Sciences Conference, XXXVIII, Abstract #2099.

Minitti, M.E., Lane, M.D., and Bishop, J.L. (2005) A new hematite formation mechanism for Mars. Meteoritics & Planetary Science, 40, 55-69.

Minitti, M.E., Mustard, J.F., and Rutherford, M.J. (2002) Effects of glass and oxidation on the spectra of SNC-like basalts: Applications to Mars remote sensing. Journal of Geophysical Research, 107(E5), 6-1: 6-16.

Mysen, B.O. and Richet, P. (2005) Silicate Glasses and Melts: Properties and Structure. Elsvier, New York, 544 p

O'Neill, H.S.C. (2005) A method for controlling alkali-metal oxide activities in one-atmosphere experiments and its application to measuring the relation activity coefficients of $NaO_{0.5}$ in silicate melts. American Mineralogist, 90, 497-501.

O'Neill, H.S.C., and Mavrogenes, J.A. (2002) The sulfide capacity and the sulfur content at sulfide saturation of silicate melts at 1400°C and 1 bar. Journal of Petrology, 43(6), 1049-1087.

Oskarsson, N., Sigvaldason, G.E., and Steinthorsson, S. (1982) A dynamic model of rift-zone petrogenesis and the regional petrology of Iceland. Journal of Petrology, 23, 28-74.

Sinton, J.M. and Detrick, R.S. (1992) Mid-ocean ridge magma chambers. Journal of Geophysical Research, 97(B1), 197-216.

Sweet, J.R. and White, W.B. (1969) Study of sodium silicate glasses and liquids by infrared reflectance spectroscopy. Physics and Chemistry of Glasses, 10, 246-251.

Wilke, M., Schmidt, C., Farges, F., Malavergne, V., Gautron, L., Simionovici, A., Hahn, M., and Petit, P. (2006) Structural environment of iron in hydrous aluminosilicate glass and melt-evidence from X-ray absorption spectroscopy. Chemical Geology, 229, 144-161.

Wilson, M. (1989) Igneous Petrogenesis. Unwin Hyman Ltd, London, 466 p.

Wyatt, M.B., Hamilton, V.E., McSween, H.Y., Christensen, P.R., and Taylor, L.A. (2001) Analysis of terrestrial and martian volcanic compositions using thermal emission spectroscopy: 1. Determination of mineralogy, chemistry, and classification strategies. Journal of Geophysical Research, 106(E7), 14711-14732.

Wyatt, M.B. and McSween, H.Y. (2002) Spectral evidence for weathered basalt as an alternative to andesite in the northern lowlands of Mars. Nature, 417, 263-266.

Appendix A: Vertical controlled-atmosphere gas-mixing furnaces

Samples were synthesized at different oxygen fugacities, therefore generating different Fe^{3+}/Fe^{2+}. To do this a vertical controlled-atmosphere gas-mixing furnace and a zirconia electrode were used. This appendix reviews oxygen fugacity, the zirconia electrode, and the structure and methods of a gas-mixing furnace.

A.1. Oxygen fugacity

The Fe^{3+}/Fe^{2+} of a glass or rock provides information regarding its source region and cooling history (Bézos and Humler, 2005; Carmichael, 1991; Christie et al., 1986; Kress and Carmichael, 1991). Factors that can affect the Fe^{3+}/Fe^{2+} of a glass or rock include crystallization, assimilation, loss of volatiles, and oxidation after eruption (Bézos and Humler, 2005; Carmichael, 1991; Christie et al., 1986; Kress and Carmichael, 1988; Kress and Carmichael, 1991). To obtain a certain Fe^{3+}/Fe^{2+} in a synthesized system it is necessary to control the availability of oxygen (oxygen fugacity, f_{O_2}). Oxygen fugacity corresponds to the partial pressure of a non-ideal gas (Anderson, 2005) and it is dependent on temperature and pressure (Blundy et al., 1991; Carmichael, 1991; Christie et al., 1986).

Typically an f_{O_2} value is referenced relative to a solid buffer for example:

$$\Delta(\text{buffer}) = \log f_{O_2}(\text{sample}) - \log f_{O_2}(\text{buffer}) \qquad [1]$$

Δ(buffer) is independent of temperature since it can be applied anywhere along the buffer curve (Carmichael, 1991). Solid buffers are generally comprised of a metal and its corresponding oxide, such as the nickel-nickel oxide buffer (NNO) equation 2 or an assemblage of minerals, such as the quartz-fayalite-magnetite buffer (QFM) equation 3.

$$Ni_{(s)} + \frac{1}{2}O_{2(g)} \rightarrow NiO_{(s)} \qquad [2]$$

$$\begin{bmatrix} 3SiO_{2(s)} + 2Fe_3O_{4(s)} \rightarrow 3Fe_2SiO_{4(s)} + O_{2(g)} \\ quartz + magnetite \rightarrow fayalite + oxygen \end{bmatrix} \qquad [3]$$

Solid buffers are at a specific f_{O_2} at a given temperature when the closed buffer assemblage has reached equilibrium. The most commonly referenced solid buffer curves ($\log f_{O_2}$ vs T) for basalts are NNO (O'Neill and Pownceby, 1993) and QFM (O'Neill, 1988) (Figure A1).

Experimentally, mixtures of gases, that react together to produce $O_{2(g)}$, are used to create specific f_{O_2} at constant temperatures and pressures (Nafziger et al., 1971). This is accomplished by varying the moles of gas available by varying the flow rates of the interacting gases. $CO_{(g)}$ and $CO_{2(g)}$ are a common gas mixture used to create the desired f_{O_2}. The CO/CO_2 gas environment controls f_{O_2} that in turn controls the redox state in the iron bearing melt as follows:

$$CO_{2(g)} \rightarrow CO_{(g)} + \frac{1}{2}O_{2(g)} \qquad [4]$$

$$2FeO_{(melt)} + \frac{1}{2}O_{2(g)} \rightarrow Fe_2O_{3(melt)} \qquad [5]$$

From these equations and previous studies an approximation of the expected Fe^{3+}/Fe^{2+} ratio can be determined (Kress and Carmichael, 1988).

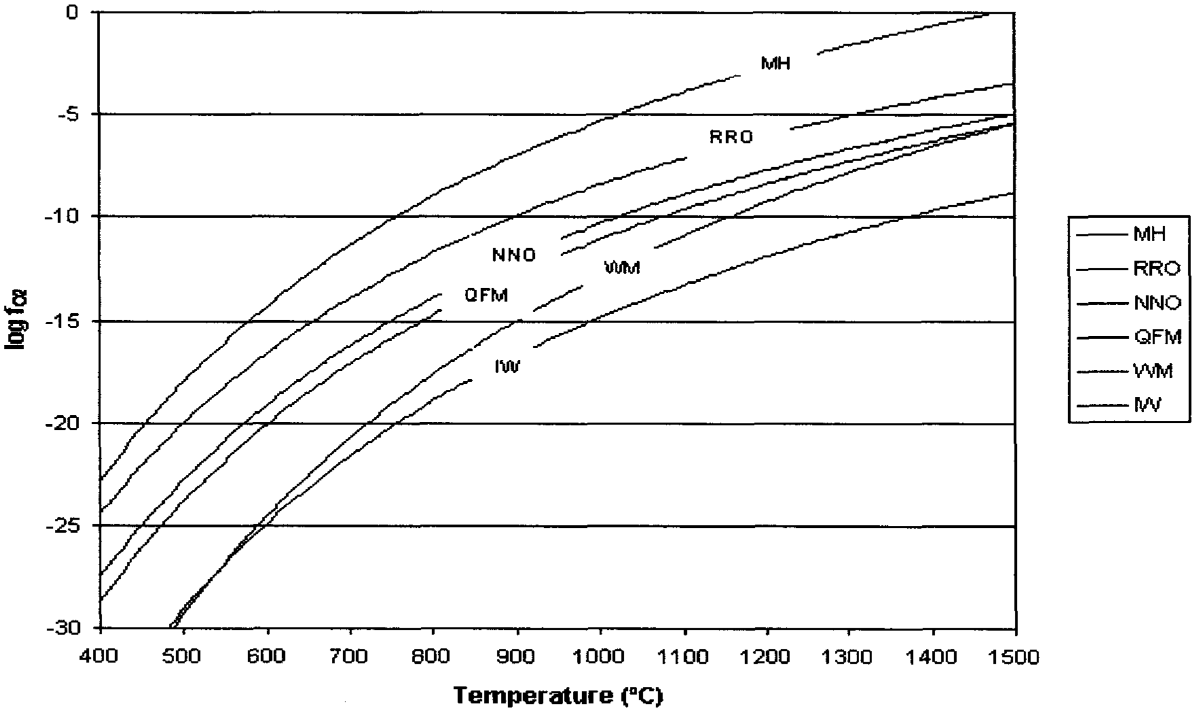

Figure A1: Reference solid buffer curves: nickel-nickel oxide buffer (NNO) (O'Neill and Pownceby, 1993), quartz-fyalite-magnetite buffer (QFM) (O'Neill, 1988), rhenium-rhenium dioxide buffer (RRO) (Pownceby and O'Neill, 1994), magnetite-hematite buffer (MH) (Schwab and Kaster, 1981), wüstite-magnetite redox buffer (WM) (O'Neill, 1988), and iron-wüstite buffer (IW) (O'Neill and Pownceby, 1993).

A.2. Zirconia electrode

A zirconia electrode is a solid electrolyte probe used for the detection of $O_{2(g)}$ (Sato, 1970). The electrode consists of a hollow alumina rod with an yttria (Y_2O_3) doped zirconia tip that has a piece of Pt wire wrapped around the tip and up the exterior of the alumina rod and a second piece of Pt wire inside the alumina rod (Fig. A2).

A potential difference (emf) is produced at elevated temperatures because the doped tip experiences ion mobility due to vacancies in its structure (Sato, 1970). The Pt wires are used to measure the emf between the outer and inner gas environments following:

$$emf = \left(\frac{RT}{4F}\right)\log\left(\frac{f_{O_2(outer)}}{f_{O_2(inner)}}\right) \qquad [6]$$

Where emf is the potential difference (V), R is the gas constant, T is temperature (K), F is Faraday's constant, f_{O_2} (outer) is the oxygen fugacity within the furnace, and f_{O_2} (inner) is the oxygen fugacity inside the alumina rod (generally a reference gas of known oxygen fugacity, such as air, $\log f_{O_2}$ (air) = 0.6789) (Sato, 1970). By using a known reference gas (air) and measuring T the equation simplifies to only two unknowns (emf and f_{O_2} (outer)):

$$emf = \left(4.96x10^{-5}T\right)\log\left(\frac{f_{O_2(outer)}}{f_{O_2(inner)}}\right) \qquad [7]$$

making it easy to obtain the f_{O_2} of the furnace environment from the emf reading.

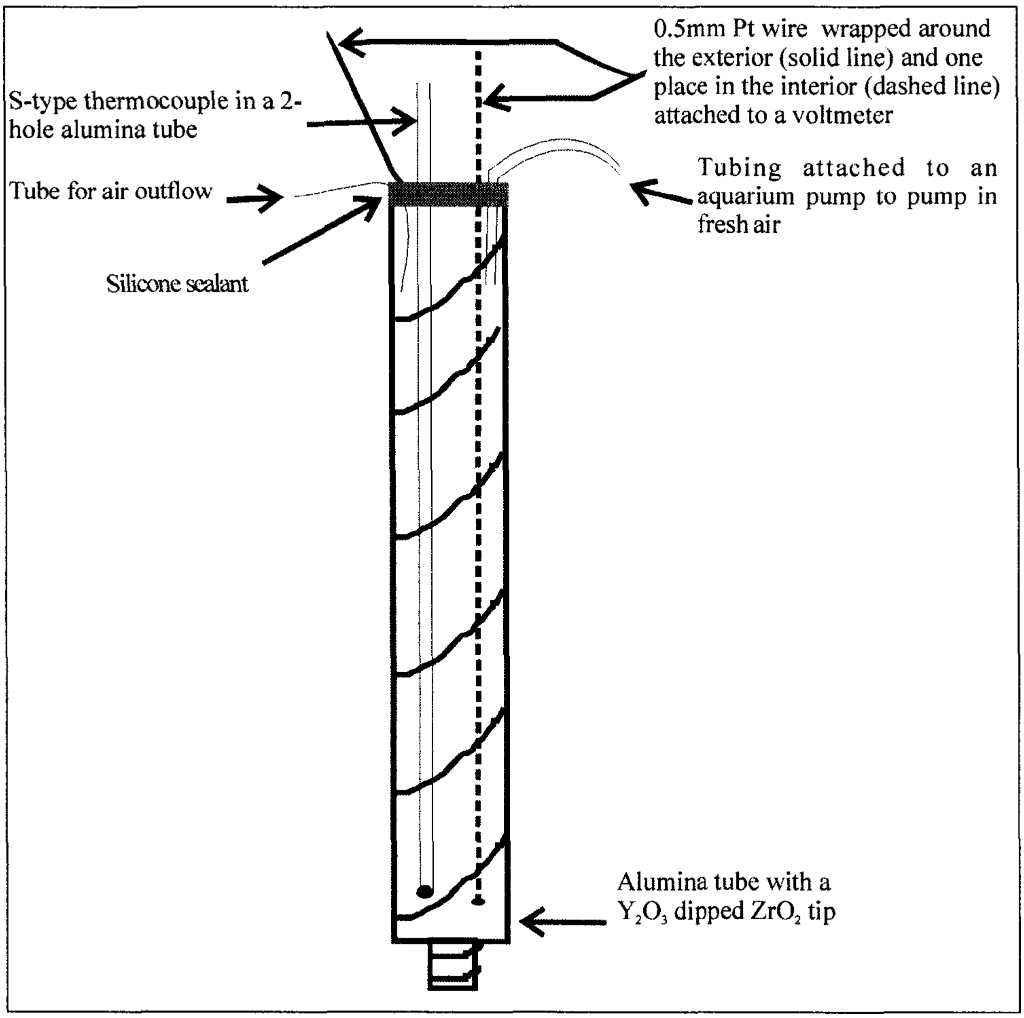

Figure A2: Schematic cross section of a zirconia electrode.

A.3. Structure of the University of Western Ontario vertical controlled-atmosphere gas-mixing furnace

The vertical controlled-atmosphere gas-mixing furnace in the Experimental Analysis Lab (EAL) at the University of Western Ontario includes a mullite tube (Fig. A3) that is surrounded by a series of heating elements all of which are enclosed in an insulated box. The top of the mullite tube is connected to a metal plate that contains the gas inflow pipe. The metal plate forms a tight seal via a Viton O-ring with the base plate for the zirconia electrode or sample holder. The bottom of the mullite tube is welded to a glass piece that connects to a removable glass piece, which contains the gas outflow pipe.

The holders for both the zirconia electrode or sample holder consist of metal base plates that have bored holes welded to Cajon fittings. The Cajon fitting contains a Viton O-ring that holds either the zirconia electrode or sample holder in place. Silicone sealant is used to fill any gaps between the electrode and the Cajon fitting. The tip of the electrode or sample holder sits directly in the centre of the furnace hot spot. In 2006, the furnace hotspot centre was measured to be 36 cm below the base plate of the holder. The structure of the electrode itself is described above in section A.2.

The sample holder is a 4-hole alumina rod that contains an S-type thermocouple in two of its holes and thick Pt wires (0.8 mm diam.) in the other two holes. Samples are either synthesized in a crucible or on wire loops. When synthesizing samples on wire loops a thin piece of Pt wire (0.127 mm diam.) is attached to the two thick Pt wires. A piece of Pt wire (0.25 mm diam.) is hung in a loop from the thin Pt wire and sample loops, in groups of three, are then hung at different heights from this wire all within the furnace hot spot (Fig. A4). Samples are drop quenched when an electric current, from a custom-made rapid quench device, is applied to the thick Pt wires, which breaks the thin Pt wire, and the sample loops drop into the cooled removable glass piece.

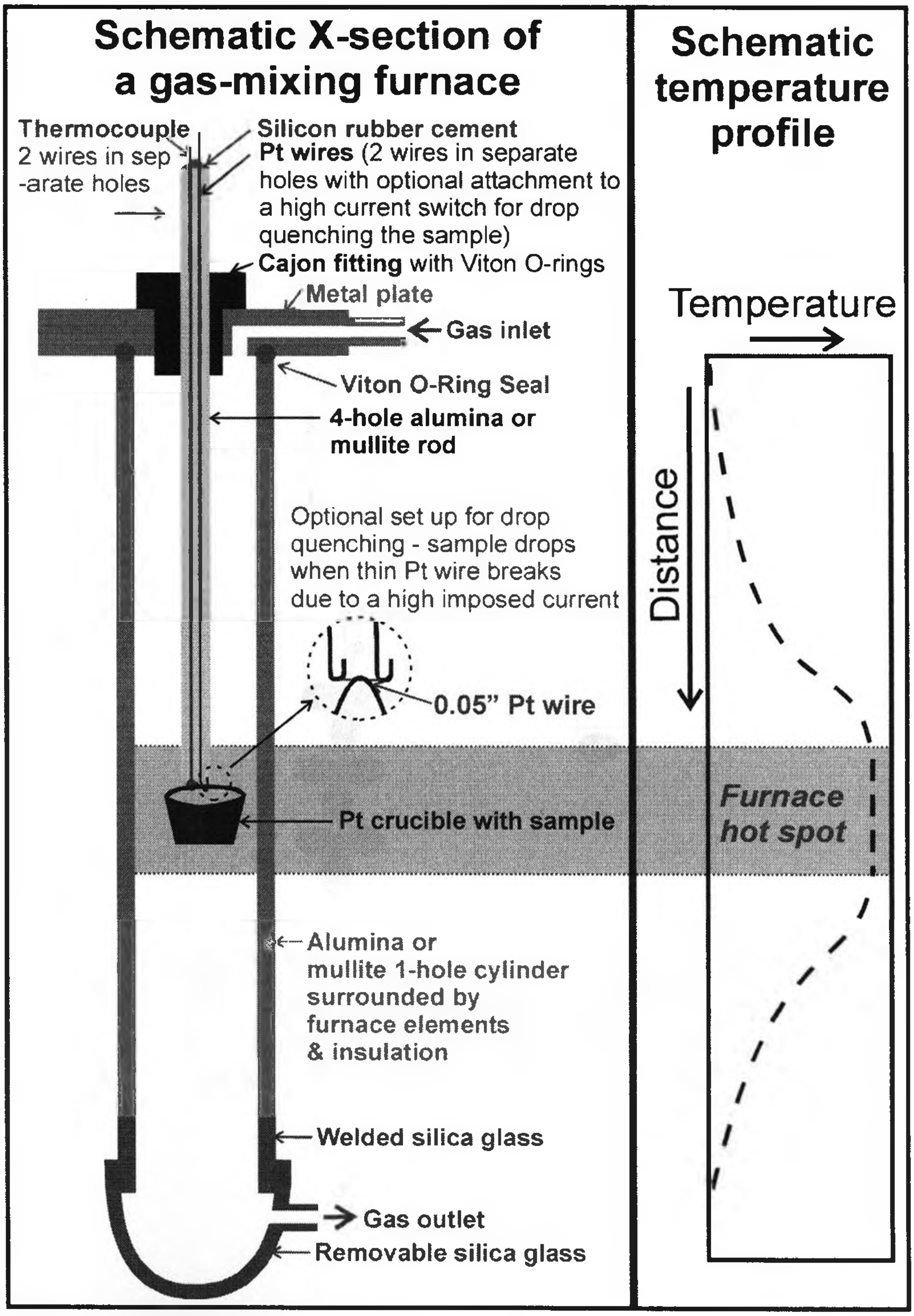

Figure A3: Schematic cross section and temperature profile of a vertical quench gas-mixing furnace

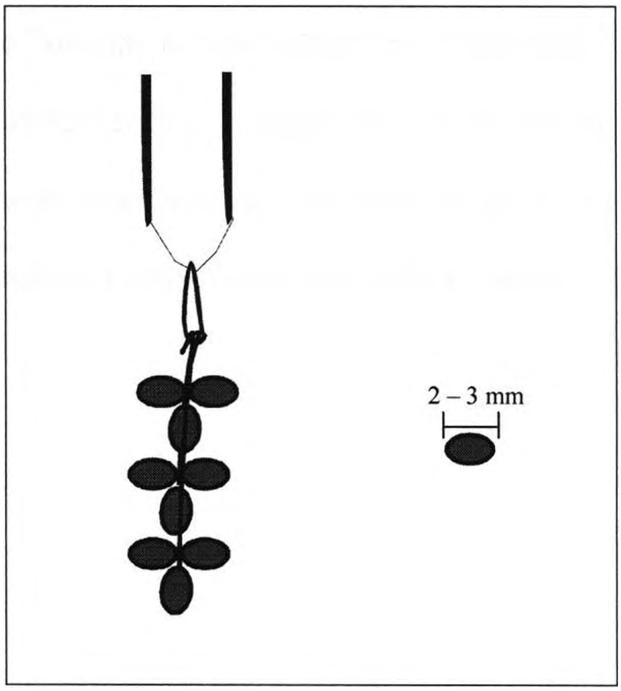

Figure A4: Sample loops, in groups of three, were hung at different heights in order to minimize contact between sample loops. The loop diameters were between 2 – 3 mm.

A.4. Running an experiment

When running an experiment there are specific steps that need to be followed in order to obtain the desired f_{O_2} and a successful synthesis.

1. Calibrate the flowmeters by attaching clear plastic tubing, marked in increments and containing a soapy solution, to the outflow of the flowmeter. Turn on a single gas at a chosen rotameter reading and time the bubbles that form with the soap solution as they pass through a length of tubing. Multiple bubbles for each rotameter reading are timed in order to get an average flow rate for that setting. Flow rates (cm^3/s) were calculated and plotted verses the rotameter reading. Figures A5 and A6 are the calibration curves for $CO_{(g)}$ and $CO_{2(g)}$ that were experimentally calculated in 2006 for the gas-mixing furnace in the Experimental Analysis Laboratory (EAL) at the University of Western Ontario.

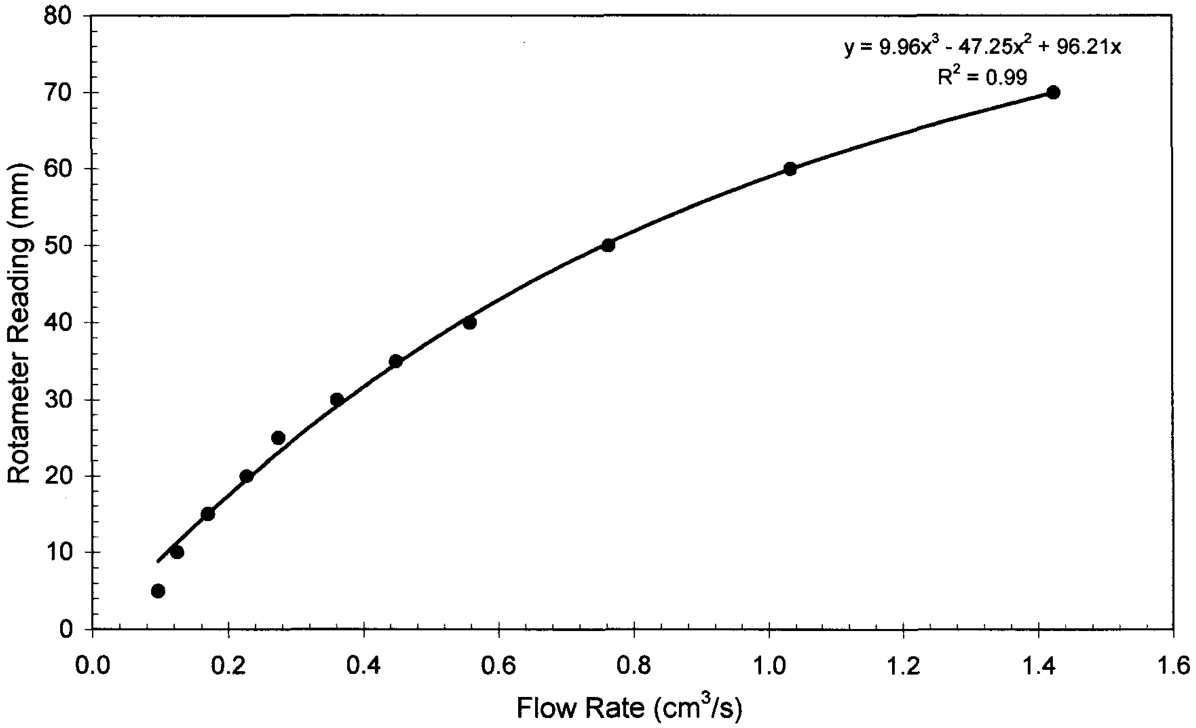

Figure A5: Calibration curve for $CO_{2(g)}$ flowing at 30 psi.

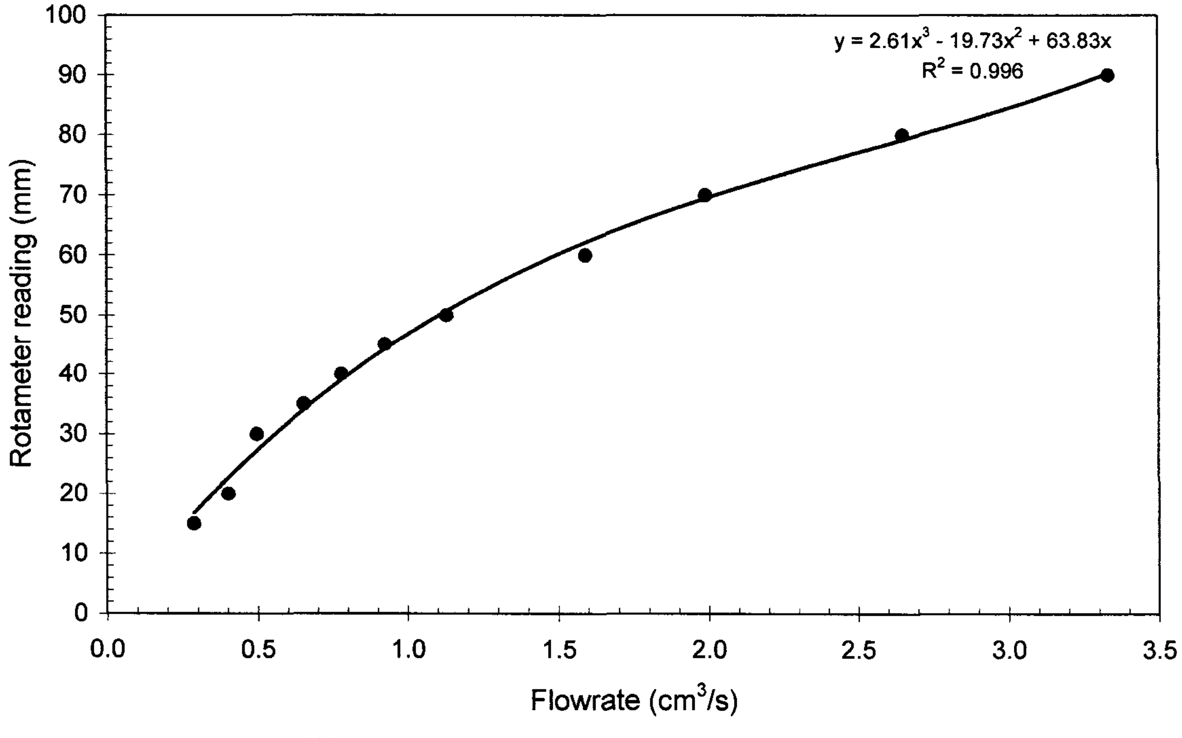

Figure A6: Calibration curve for $CO_{(g)}$ flowing at 30 psi.

2. Calculate the $\log f_{O_2}$ value at a given temperature. These values are calculated by using thermodynamic data for a specific solid buffer that has been previously determined. For example O'Neill & Pownceby (1993) determined that the $\log f_{O_2}$ value for NNO can be calculated by the following:

$$\log\left(f_{O_2}\right)=12.9792-\left(\frac{25015.1}{T}\right)-0.51162*\ln T+\frac{0.046(P-1)}{T} \qquad [8]$$

Where f_{O_2} is oxygen fugacity, T is temperature in K, and P is pressure in bars. References for equations of other common solid buffer curves can be found in the caption for Figure A1. The equations are found in an Excel Spreadsheet called “Determining fO2” on a CD labelled “Gas-Mixing Furnace” in the EAL.

3. Determine the ratio of gases needed to create the desired $\log f_{O_2}$ by using COHSClFgas (Kress et al., 2004) found in an Excel Spreadsheet called “COHSClFgas” on a CD labelled “Gas-Mixing Furnace” in the EAL. The program requires the temperature of the synthesis as well as inputted values for the gases that will be used. The inputted values are varied until the desired output value for $\log f_{O_2}$ is obtained. The $CO:CO_2$ ratio is then recorded.

4. Select a flow rate for the synthesis that allows the gases to reach equilibrium and one strong enough to buffer the system. Generally the total flow rate is kept in the range of 1.67 – 3.00 cm^3/s (Kress, 1997; Kress, 2006). The ratio of $CO:CO_2$ and total flow rate are used to calculate the flow rate of each individual gas using the following:

$$\frac{V_{CO}}{t}+\frac{V_{CO_2}}{t}=\text{Total flow rate} \qquad [9]$$

$$\frac{V_{CO}}{V_{CO_2}} = \text{the ratio calculated from COHSClFgas} \qquad [10]$$

Where V_{CO} and V_{CO_2} are volumes and t is time. Once the individual flow rates for $CO_{(g)}$ and $CO_{2(g)}$ are determined the equations from the calibration curves in Figures A4 and A5 are used to determine the approximate rotameter readings.

5. Begin the synthesis by slowly stepwise lowering the zirconia electrode into the hot spot of the furnace. Once the electrode is in place turn on the gases to the calculated rotameter readings. The gases will need minor adjustments in order to get the correct emf reading that is calculated using equation 7. When the correct emf is stable slowly stepwise remove the zirconia electrode without turning off the gases. Lower the sample, on the sample holder either on wire loops or in a crucible, into the furnace hot spot. Give the sample ample time for the Fe^{3+}/Fe^{2+} to equilibrate, such as 5 – 8 hours for samples that are run on ~2 – 3 mm diameter loops, which allows the melt time to equilibrate while minimizing alkali-loss (Kress and Carmichael, 1988).

6. A rapid quench is used to drop samples to the lower portion of the furnace, which has been pre-cooled in an ice-water bath, ensuring all samples, run at the same f_{O_2} are quenched in the same gaseous environment.

7. A final emf reading should be taken in order to determine if the f_{O_2} fluctuated during the synthesis.

A.5. References

Anderson, G. (2005) Thermodynamics of Natural Systems. 648 p. Cambridge University Press, New York.

Bézos, A., and Humler, E. (2005) The Fe^{3+}/Fe_{total} ratios of MORB glasses and their implications for mantle melting. Geochimica et Cosmochimica Acta, 69, 711-725.

Blundy, J.D., Brodholt, J.P., and Wood, B.J. (1991) Carbon-fluid equilibria and the oxidation state of the upper mantle. Nature, 349, 321-324.

Carmichael, I.S.E. (1991) The redox states of basic and silicic magmas: a reflection of their source regions? Contributions to Mineralogy and Petrology, 106, 129-141.

Christie, D.M., Carmichael, I.S.E., and Langmuir, C.H. (1986) Oxidation states of mid-ocean ridge basalt glasses. Earth and Planetary Science Letters, 79, 397-411.

Kress, V.C. (1997) Thermochemistry of sulfide liquids. I. The system O-S-Fe at 1 bar. Contributions to Mineralogy and Petrology, 127, 176-186.

-. (2006) Personal communication.

Kress, V.C., and Carmichael, I.S.E. (1988) Stoichiometry of the iron oxidation reaction in silicate melts. American Mineralogist, 73, 1267-1274.

-. (1991) The compressibility of silicate liquids containing Fe_2O_3 and the effect of composition, temperature, oxygen fugacity and pressure on their redox states. Contributions to Mineralogy and Petrology, 108, 82-92.

Kress, V.C., Ghiorso, M.S., and Lastuka, C. (2004) Microsoft EXCEL spreadsheet-based program for calculating equilibrium gas speciation in the C-O-H-S-Cl-F system. Computers & Geosciences, 30, 211-214.

Nafziger, R.H., Ulmer, G.C., and Woermann, E. (1971) Gaseous buffering for the control of oxygen fugacity at one atmosphere. In G.C. Ulmer, Ed. Techniques for high pressure and high temperature, p. 9-41. Springer, New York.

O'Neill, H.S.C. (1988) Systems Fe-O and Cu-O - thermodynamic data for the equilibria Fe-FeO, Fe-Fe_3O_4, FeO-Fe_3O_4, Fe_3O_4-Fe_2O_3, Cu-Cu_2O, and Cu_2O-CuO from emf-measurements. American Mineralogist, 73(5-6), 470-486.

O'Neill, H.S.C., and Pownceby, M.I. (1993) Thermodynamic data from redox reactions at high-temperatures. 1. An experimental and theoretical assessment of the electrochemical method using stabilized zirconia electrolytes, with revised values for the Fe-FeO, CO-COO, Ni-NiO and Cu-Cu_2O oxygen buffers and new data for the W-WO_2 buffer. Contributions to Mineralogy and Petrology, 114(3), 296-314.

Pownceby, M.I., and O'Neill, H.S.C. (1994) Thermodynamic data from redox reactions at high temperatures. IV. Calibration of the Re-ReO_2 oxygen buffer from EMF and NiO + Ni-Pd redox sensor measurements. Contributions to Mineralogy and Petrology, 118, 130-137.

Sato, M. (1970) An electrochemical method of oxygen fugacity control of furnace atmosphere for mineral syntheses. The American Mineralogist, 55, 1424-1431.

Appendix B: Synthetic basaltic glass data repository

B.1. Summary of synthetic basaltic glass data

Table 1B: Experimental data for the synthetic basaltic glasses.

	NNO-4_Re				NNO-3_Re			
Sample Number	1	2	3	4	5	6	7	8
T range (°C)	1414-1417	1414-1417	1414-1417	1414-1417	1413-1417	1413-1417	1413-1417	1413-1417
log (f_{O_2})	-10.01	-10.01	-10.01	-10.01	-8.69	-8.69	-8.69	-8.69
Loop material	Re	Re	Re	Re	Re	Re	Re	Re
Duration (h)	5	5	5	5	5	5	5	5
Other								
wt.%								
SiO_2	51.61	51.74	51.52	51.53	51.39	50.99	50.95	51.19
TiO_2	2.67	2.68	2.66	2.66	2.62	2.64	2.60	2.60
Al_2O_3	11.88	11.93	11.98	11.95	11.70	11.57	11.43	11.73
FeO	11.42	11.54	11.52	11.38	11.29	11.39	11.27	11.22
MnO	0.18	0.16	0.16	0.18	0.16	0.14	0.15	0.18
MgO	9.97	9.95	9.87	9.96	9.97	9.99	10.00	10.08
CaO	10.77	10.73	10.72	10.72	10.49	10.46	10.36	10.40
Na_2O	0.40	0.40	0.41	0.39	0.44	0.46	0.41	0.45
K_2O	0.26	0.25	0.24	0.25	0.25	0.23	0.23	0.24
P_2O_5	0.15	0.16	0.14	0.14	0.16	0.14	0.15	0.16
Total	99.30	99.53	99.22	99.16	98.48	98.01	97.55	98.26
μR min. loc.	1235	1233	1233	1231	1233	1231	1234	1233
KK-abs max. loc.	1038	1038	1038	1038	1043	1038	1039	1039
KK-abs FWHM	221	223	223	221	224	221	221	222
Mg#	60.9	60.6	60.4	60.9	61.2	61.0	61.3	61.6
Total Alkali wt.%	0.66	0.65	0.65	0.64	0.69	0.69	0.64	0.69
Calculated Fe^{3+}/Fe^{2+}	0.0269	0.0268	0.0268	0.0268	0.0487	0.0487	0.0486	0.0486
Calculated Refractive Index	1.611	1.612	1.611	1.611	1.611	1.612	1.611	1.611
CIPW Norm wt.%								
Quartz	8.4	8.5	8.4	8.4	8.9	8.5	9.0	8.7
Plagioclase	33.2	33.4	33.6	33.4	32.9	32.7	32.1	33.1
Orthoclase	1.5	1.5	1.4	1.5	1.5	1.4	1.4	1.4
Diopside	18.4	18.1	18.1	18.1	17.7	18.0	17.7	17.3
Hypersthene	31.8	32.1	31.9	31.9	31.1	31.0	31.1	31.5
Ilmenite	5.1	5.1	5.1	5.1	5.0	5.0	4.9	4.9
Magnetite	0.6	0.6	0.6	0.6	1.1	1.1	1.1	1.1
Hematite	0.0	0.0	0.0	0.0	0.0	0.0	0.0	0.0
Apatite	0.4	0.4	0.3	0.3	0.4	0.3	0.4	0.4
Total	99.4	99.6	99.3	99.2	98.6	98.1	97.6	98.3

Table 1B: Continued.

	NNO-3_dPt_1							
Sample Number	9	10	11	12	13	14	15	16
T range (°C)	1413-1416	1413-1416	1413-1416	1413-1416	1413-1416	1413-1416	1413-1416	1413-1416
log (f_{O_2})	-8.7	-8.7	-8.7	-8.7	-8.7	-8.7	-8.7	-8.7
Loop material	dPt	dPt	dPt	dPt	dPt	dPt	dPt	dPt
Duration (h)	5	5	5	5	5	5	5	5
Other								
wt.%								
SiO_2	55.15	54.91	55.03	55.08	54.42	55.43	55.57	55.11
TiO_2	2.82	2.84	2.79	2.79	2.73	2.75	2.79	2.85
Al_2O_3	12.55	12.54	12.50	12.59	12.49	12.68	12.59	12.45
FeO	6.06	6.23	6.48	6.25	6.67	7.04	6.65	7.12
MnO	0.13	0.16	0.17	0.19	0.13	0.18	0.16	0.13
MgO	10.68	10.51	10.59	10.56	10.68	10.63	10.58	10.61
CaO	11.21	11.29	11.27	11.11	11.22	11.24	11.38	11.18
Na_2O	0.60	0.62	0.61	0.60	0.59	0.64	0.62	0.64
K_2O	0.32	0.33	0.31	0.33	0.34	0.31	0.33	0.31
P_2O_5	0.13	0.12	0.12	0.11	0.09	0.11	0.12	0.09
Total	99.64	99.55	99.87	99.61	99.36	101.01	100.78	100.49
µR min. loc.	1243	1242	1240	1244	1241	1246	1240	1241
KK-abs max. loc.	1049	1051	1051	1054	1052	1049	1052	1049
KK-abs FWHM	228	227	227	232	231	230	230	229
Mg#	75.9	75.1	74.5	75.1	74.1	72.9	73.9	72.7
Total Alkali wt.%	0.92	0.95	0.92	0.93	0.93	0.95	0.94	0.95
Calculated Fe^{3+}/Fe^{2+}	0.0539	0.0540	0.0537	0.0535	0.0535	0.0531	0.0537	0.0531
Calculated Refractive Index	1.593	1.594	1.594	1.593	1.595	1.595	1.594	1.596
CIPW Norm wt.%								
Quartz	13.5	13.1	13.1	13.4	12.2	12.7	13.2	12.6
Plagioclase	35.7	35.7	35.6	35.8	35.4	36.2	35.8	35.6
Orthoclase	1.9	2.0	1.8	2.0	2.0	1.8	2.0	1.8
Diopside	19.2	19.7	19.7	18.9	19.6	19.4	20.0	19.7
Hypersthene	23.2	22.8	23.6	23.5	24.1	24.8	23.6	24.5
Ilmenite	5.4	5.4	5.3	5.3	5.2	5.2	5.3	5.4
Magnetite	0.6	0.6	0.6	0.6	0.6	0.7	0.6	0.7
Hematite	0.0	0.0	0.0	0.0	0.0	0.0	0.0	0.0
Apatite	0.3	0.3	0.3	0.3	0.2	0.3	0.3	0.2
Total	99.7	99.6	99.9	99.7	99.4	101.1	100.8	100.5

Table 1B: Continued.

	NNO-3_dPt_1 Cont.	
Sample Number	17	18
T range (°C)	1413-1416	1413-1416
$\log (f_{O_2})$	-8.7	-8.7
Loop material	dPt	dPt
Duration (h)	5	5
Other		
wt.%		
SiO_2	53.82	54.06
TiO_2	2.82	2.76
Al_2O_3	12.27	12.31
FeO	8.36	8.23
MnO	0.20	0.12
MgO	10.36	10.35
CaO	11.13	11.05
Na_2O	0.84	0.87
K_2O	0.34	0.34
P_2O_5	0.11	0.10
Total	100.24	100.20
µR min. loc.	1240	1238
KK-abs max. loc.	1046	1045
KK-abs FWHM	223	223
Mg#	68.8	69.1
Total Alkali wt.%	1.17	1.21
Calculated Fe^{3+}/Fe^{2+}	0.0528	0.0528
Calculated Refractive Index	1.601	1.6
CIPW Norm wt.%		
Quartz	9.8	10.1
Plagioclase	35.8	36.0
Orthoclase	2.0	2.0
Diopside	20.7	20.5
Hypersthene	25.5	25.4
Ilmenite	5.4	5.2
Magnetite	0.8	0.8
Hematite	0.0	0.0
Apatite	0.3	0.2
Total	100.3	100.3

Table 1B: Continued.

	NNO-3_dPt_2							
Sample Number	19	20	21	22	23	24	25	26
T range (°C)	1414-1417	1414-1417	1414-1417	1414-1417	1414-1417	1414-1417	1414-1417	1414-1417
$\log(f_{O_2})$	-8.66	-8.66	-8.66	-8.66	-8.66	-8.66	-8.66	-8.66
Loop material	dPt	dPt	dPt	dPt	dPt	dPt	dPt	dPt
Duration (h)	5	5	5	5	5	5	5	5
Other								
wt.%								
SiO_2	53.38	53.29	53.16	52.80	53.02	53.19	53.07	53.63
TiO_2	2.75	2.75	2.67	2.84	2.83	2.74	2.76	2.83
Al_2O_3	12.41	12.33	12.12	11.92	12.27	12.28	12.24	12.25
FeO	8.27	8.30	8.40	8.64	8.62	8.73	8.74	8.54
MnO	0.14	0.16	0.14	0.14	0.16	0.11	0.14	0.22
MgO	10.62	10.45	10.39	10.17	10.10	10.27	10.31	10.49
CaO	11.01	11.00	10.61	10.97	10.91	10.91	10.84	10.84
Na_2O	1.40	1.36	1.35	1.31	1.38	1.37	1.38	1.33
K_2O	0.39	0.40	0.40	0.42	0.37	0.42	0.40	0.39
P_2O_5	0.21	0.23	0.23	0.20	0.22	0.23	0.20	0.24
Total	100.58	100.25	99.47	99.41	99.87	100.26	100.08	100.75
μR min. loc.	1238	1234	1234	1234	1237	1233	1233	1236
KK-abs max. loc.	1047	1045	1043	1045	1042	1043	1042	1046
KK-abs FWHM	209	208	208	212	213	213	214	215
Mg#	69.6	69.2	68.8	67.7	67.6	67.7	67.8	68.7
Total Alkali wt.%	1.79	1.75	1.74	1.73	1.75	1.80	1.78	1.72
Calculated Fe^{3+}/Fe^{2+}	0.0554	0.0553	0.0546	0.0552	0.0550	0.0549	0.0548	0.0547
Calculated Refractive Index	1.6	1.6	1.599	1.602	1.601	1.601	1.601	1.601
CIPW Norm wt.%								
Quartz	6.4	6.7	7.2	6.9	6.9	6.6	6.5	7.3
Plagioclase	38.3	37.9	37.3	36.5	37.9	37.7	37.7	37.6
Orthoclase	2.3	2.4	2.4	2.5	2.2	2.5	2.4	2.3
Diopside	21.5	21.5	20.3	22.3	21.3	21.3	21.3	20.8
Hypersthene	25.7	25.4	26.0	24.6	24.9	25.6	25.7	26.1
Ilmenite	5.2	5.2	5.1	5.4	5.4	5.2	5.2	5.4
Magnetite	0.8	0.8	0.8	0.8	0.8	0.8	0.8	0.8
Hematite	0.0	0.0	0.0	0.0	0.0	0.0	0.0	0.0
Apatite	0.5	0.5	0.5	0.5	0.5	0.5	0.5	0.6
Total	100.6	100.3	99.5	99.5	99.9	100.3	100.1	100.8

Table 1B: Continued.

	NNO-2_Re				
Sample Number	27	28	29	30	31
T range (°C)	1414-1418	1414-1418	1414-1418	1414-1418	1414-1418
log (fo_2)	-7.63	-7.63	-7.63	-7.63	-7.63
Loop material	Re	Re	Re	Re	Re
Duration (h)	5	5	5	5	5
Other					
wt.%					
SiO_2	52.52	52.37	52.20	52.09	52.22
TiO_2	2.67	2.67	2.67	2.63	2.59
Al_2O_3	12.07	12.09	11.96	11.92	11.97
FeO	11.59	11.55	11.66	11.50	11.63
MnO	0.16	0.15	0.14	0.15	0.18
MgO	10.08	10.00	9.98	9.98	10.03
CaO	10.70	10.82	10.77	10.78	10.72
Na_2O	0.26	0.33	0.37	0.34	0.36
K_2O	0.03	0.05	0.06	0.07	0.07
P_2O_5	0.25	0.25	0.26	0.22	0.23
Total	100.32	100.28	100.06	99.69	100.01
μR min. loc.	1231	1236	1235	1238	1234
KK-abs max. loc.	1038	1039	1038	1041	1038
KK-abs FWHM	228	228	228	227	226
Mg#	60.8	60.7	60.4	60.7	60.6
Total Alkali wt.%	0.29	0.39	0.42	0.41	0.43
Calculated Fe^{3+}/Fe^{2+}	0.0768	0.0776	0.0776	0.0778	0.0775
Calculated Refractive Index	1.611	1.611	1.612	1.611	1.611
CIPW Norm wt.%					
Quartz	11.4	10.9	10.6	10.6	10.5
Plagioclase	33.9	34.2	33.9	33.7	33.9
Orthoclase	0.2	0.3	0.4	0.4	0.4
Diopside	16.1	16.8	17.0	17.3	17.0
Hypersthene	31.6	30.9	31.0	30.7	31.3
Ilmenite	5.1	5.1	5.1	5.0	4.9
Magnetite	1.7	1.7	1.7	1.7	1.7
Hematite	0.0	0.0	0.0	0.0	0.0
Apatite	0.6	0.6	0.6	0.5	0.5
Total	100.5	100.4	100.2	99.8	100.1

Table 1B: Continued.

	NNO-1.5_Re			
Sample Number	32	33	34	35
T range (°C)	1414-1420	1414-1420	1414-1420	1414-1420
log (f_{O_2})	-7.11	-7.11	-7.11	-7.11
Loop material	Re	Re	Re	Re
Duration (h)	5	5	5	5
Other				
wt.%				
SiO_2	51.75	51.30	51.34	51.68
TiO_2	2.74	2.72	2.73	2.72
Al_2O_3	11.96	12.03	11.82	11.87
FeO	11.25	11.25	11.48	11.31
MnO	0.11	0.17	0.18	0.18
MgO	9.95	9.86	9.75	9.82
CaO	10.77	10.71	10.63	10.82
Na_2O	0.04	0.06	0.05	0.06
K_2O	0.03	0.03	0.04	0.02
P_2O_5	0.20	0.24	0.23	0.25
Total	98.80	98.38	98.25	98.72
μR min. loc.	1238	1238	1240	1235
KK-abs max. loc.	1038	1038	1037	1041
KK-abs FWHM	234	233	234	235
Mg#	61.2	61.0	60.2	60.8
Total Alkali wt.%	0.07	0.09	0.10	0.08
Calculated Fe^{3+}/Fe^{2+}	0.0969	0.0967	0.0964	0.0972
Calculated Refractive Index	1.612	1.612	1.612	1.612
CIPW Norm wt.%				
Quartz	12.4	12.0	12.3	12.4
Plagioclase	32.7	33.0	32.3	32.6
Orthoclase	0.2	0.2	0.2	0.1
Diopside	16.0	15.5	15.7	16.2
Hypersthene	30.0	30.1	30.1	29.8
Ilmenite	5.2	5.2	5.2	5.2
Magnetite	2.0	2.0	2.0	2.0
Hematite	0.0	0.0	0.0	0.0
Apatite	0.5	0.6	0.5	0.6
Total	98.9	98.5	98.4	98.9

Table 1B: Continued.

	NNO-1.5_dPt					NNO+1_Pt		
Sample Number	36	37	38	39	40	41	42	43
T range (°C)	1413-1416	1413-1416	1413-1416	1413-1416	1413-1416	1414-1417	1414-1417	1414-1417
$\log (f_{O_2})$	-7.12	-7.12	-7.12	-7.12	-7.12	-4.55	-4.55	-4.55
Loop material	dPt	dPt	dPt	dPt	dPt	Pt	Pt	Pt
Duration (h)	5	5	5	5	5	5	5	5
Other								
wt.%								
SiO_2	51.44	51.33	51.43	51.54	51.34	50.91	50.72	50.96
TiO_2	2.75	2.77	2.79	2.64	2.74	2.68	2.69	2.77
Al_2O_3	12.02	12.00	12.16	12.05	12.04	11.86	11.84	11.84
FeO	10.40	10.37	10.32	10.33	10.45	9.39	9.87	9.76
MnO	0.11	0.17	0.15	0.23	0.13	0.16	0.18	0.16
MgO	9.92	10.05	9.76	9.83	9.83	9.89	9.93	9.88
CaO	10.67	10.71	10.69	10.69	10.59	10.62	10.62	10.57
Na_2O	1.45	1.48	1.52	1.49	1.45	1.80	1.82	1.77
K_2O	0.39	0.44	0.44	0.42	0.46	0.47	0.48	0.50
P_2O_5	0.20	0.21	0.20	0.22	0.21	0.20	0.21	0.23
Total	99.35	99.52	99.46	99.44	99.24	97.99	98.36	98.45
μR min. loc.	1234	1232	1230	1232	1233	1229	1232	1232
KK-abs max. loc.	1039	1038	1041	1041	1040	1042	1038	1038
KK-abs FWHM	204	205	204	203	205	202	201	201
Mg#	63.0	63.4	62.8	62.9	62.7	65.3	64.2	64.3
Total Alkali wt.%	1.84	1.92	1.96	1.91	1.91	2.28	2.30	2.27
Calculated Fe^{3+}/Fe^{2+}	0.1073	0.1079	0.1079	0.1078	0.1072	0.3575	0.3552	0.3543
Calculated Refractive Index	1.608	1.608	1.607	1.606	1.607	1.604	1.606	1.606
CIPW Norm wt.%								
Quartz	4.9	4.2	4.5	4.7	4.7	5.4	4.8	5.5
Plagioclase	37.4	37.3	37.9	37.6	37.3	38.1	38.1	37.9
Orthoclase	2.3	2.6	2.6	2.5	2.7	2.8	2.8	3.0
Diopside	21.4	21.8	21.6	21.6	21.2	22.6	22.8	22.3
Hypersthene	26.0	26.2	25.4	26.0	26.0	19.3	19.8	19.6
Ilmenite	5.2	5.3	5.3	5.0	5.2	5.1	5.1	5.3
Magnetite	1.8	1.8	1.8	1.8	1.9	4.5	4.8	4.7
Hematite	0.0	0.0	0.0	0.0	0.0	0.0	0.0	0.0
Apatite	0.5	0.5	0.5	0.5	0.5	0.5	0.5	0.5
Total	99.5	99.7	99.6	99.6	99.4	98.3	98.7	98.8

Table 1B: Continued.

	NNO+3_Pt					
Sample Number	44	45	46	47	48	49
T range (°C)	1414-1418	1414-1418	1414-1418	1414-1418	1414-1418	1414-1418
log (f_{O_2})	-2.95	-2.95	-2.95	-2.95	-2.95	-2.95
Loop material	Pt	Pt	Pt	Pt	Pt	Pt
Duration (h)	5	5	5	5	5	5
Other						
wt.%						
SiO_2	50.25	50.87	50.43	49.55	49.99	50.38
TiO_2	2.61	2.63	2.65	2.58	2.55	2.59
Al_2O_3	11.70	11.77	11.79	11.50	11.55	11.74
FeO	10.79	10.59	10.73	10.62	10.97	11.00
MnO	0.19	0.14	0.12	0.13	0.15	0.18
MgO	9.69	9.72	9.79	9.60	9.60	9.69
CaO	10.41	10.52	10.47	10.49	10.47	10.56
Na_2O	1.94	1.97	1.94	1.88	1.94	1.94
K_2O	0.51	0.45	0.48	0.49	0.50	0.47
P_2O_5	0.22	0.23	0.20	0.24	0.21	0.21
Total	98.31	98.90	98.59	97.09	97.92	98.78
μR min. loc.	1228	1229	1228	1228	1230	1232
KK-abs max. loc.	1040	1041	1040	1041	1038	1040
KK-abs FWHM	201	199	199	200	199	199
Mg#	61.6	62.1	61.9	61.7	60.9	61.1
Total Alkali wt.%	2.45	2.43	2.42	2.38	2.44	2.42
Calculated Fe^{3+}/Fe^{2+}	0.7239	0.7272	0.7237	0.7286	0.7251	0.7234
Calculated Refractive Index	1.608	1.607	1.608	1.609	1.609	1.609
CIPW Norm wt.%						
Quartz	6.7	7.3	6.8	6.5	6.5	6.6
Plagioclase	38.1	38.6	38.5	37.4	37.8	38.4
Orthoclase	3.0	2.7	2.8	2.9	3.0	2.8
Diopside	22.3	22.4	22.3	22.7	22.9	22.8
Hypersthene	14.5	14.3	14.5	14.2	14.4	14.6
Ilmenite	5.0	5.0	5.0	4.9	4.8	4.9
Magnetite	8.9	8.7	8.8	8.6	8.8	8.7
Hematite	0.0	0.0	0.0	0.0	0.0	0.0
Apatite	0.5	0.5	0.5	0.6	0.5	0.5
Total	98.9	99.5	99.2	97.7	98.5	99.4

Table 1B: Continued.

	NNO+3_dPt							
Sample Number	50	51	52	53	54	55	56	57
T range (°C)	1408-1412	1408-1412	1408-1412	1408-1412	1408-1412	1408-1412	1408-1412	1408-1412
$\log (f_{O_2})$	-2.95	-2.95	-2.95	-2.95	-2.95	-2.95	-2.95	-2.95
Loop material	dPt	dPt	dPt	dPt	dPt	dPt	dPt	dPt
Duration (h)	5	5	5	5	5	5	5	5
Other								
wt.%								
SiO_2	50.74	49.9	49.62	50.4	49.76	49.67	49.75	48.57
TiO_2	2.6426	2.6035	2.5755	2.5705	2.6289	2.5511	2.5763	2.5618
Al_2O_3	11.71	11.56	11.52	11.69	11.61	12.17	12.24	12.12
FeO	12.444403	12.36342	12.489393	12.26444	12.750339	12.894309	12.795329	12.804328
MnO	0.1514	0.1558	0.1944	0.1618	0.1587	0.1468	0.1913	0.1631
MgO	9.78	9.83	9.45	9.78	9.67	9.49	9.41	9.48
CaO	10.17	10.27	10.26	10.36	10.35	10.25	10.23	10.11
Na_2O	1.95	1.9613	1.9536	1.9241	1.9464	1.8399	1.8141	1.8348
K_2O	0.4373	0.4593	0.4791	0.4462	0.4543	0.4286	0.4628	0.4494
P_2O_5	0.2206	0.1889	0.2139	0.2187	0.207	0.1447	0.147	0.1648
Total	100.25	99.29	98.76	99.82	99.54	99.59	99.62	98.26
μR min. loc.	1221	1226	1226	1222	1226	1224	1226	1225
KK-abs max. loc.	1035	1040	1036	1037	1037	1036	1036	1035
KK-abs FWHM	201	203	200	201	203	205	204	205
Mg#	58.4	58.6	57.4	58.7	57.5	56.8	56.7	56.9
Total Alkali wt.%	2.39	2.42	2.43	2.37	2.40	2.27	2.28	2.28
Calculated Fe^{3+}/Fe^{2+}	0.7124	0.7194	0.7192	0.7190	0.7157	0.7009	0.7008	0.7004
Calculated Refractive Index	1.612	1.613	1.613	1.612	1.615	1.614	1.614	1.616
CIPW Norm wt.%								
Quartz	7.2	6.1	6.4	6.8	6.2	6.5	6.8	5.7
Plagioclase	38.4	38.0	37.8	38.2	38.1	39.3	39.2	39.0
Orthoclase	2.6	2.7	2.8	2.7	2.7	2.5	2.7	2.7
Diopside	21.2	22.2	22.2	21.9	22.2	20.6	20.3	20.1
Hypersthene	15.8	15.5	14.7	15.5	15.2	15.7	15.6	15.8
Ilmenite	5.0	4.9	4.9	4.9	5.0	4.8	4.9	4.9
Magnetite	10.2	10.2	10.3	10.1	10.5	10.6	10.5	10.5
Hematite	0.0	0.0	0.0	0.0	0.0	0.0	0.0	0.0
Apatite	0.5	0.4	0.5	0.5	0.5	0.3	0.4	0.4
Total	101.0	100.0	99.5	100.5	100.3	100.3	100.3	99.0

Table 1B: Continued.

	NNO+3_dPt Cont.		Alk_5A			
Sample Number	58	59	60	61	62	63
T range (°C)	1408-1412	1408-1412	1414-1417	1414-1417	1414-1417	1414-1417
log (f_{O_2})	-2.95	-2.95	-2.95	-2.95	-2.95	-2.95
Loop material	dPt	dPt	Pt	Pt	Pt	Pt
Duration (h)	5	5	5	5	5	5
Other			3.22 mg Na_2CO_3 added to 248.19 mg basalt	3.22 mg Na_2CO_3 added to 248.19 mg basalt	3.22 mg Na_2CO_3 added to 248.19 mg basalt	3.22 mg Na_2CO_3 added to 248.19 mg basalt
wt.%						
SiO_2	49.48	49.06	50.81	50.56	50.78	51.46
TiO_2	2.5762	2.5689	2.65	2.70	2.65	2.66
Al_2O_3	12.48	12.38	11.72	11.73	11.75	11.91
FeO	12.894309	12.804328	9.98	10.22	10.18	10.39
MnO	0.1275	0.1794	0.20	0.16	0.17	0.14
MgO	9.61	9.43	9.48	9.61	9.63	9.85
CaO	10.21	10.16	10.43	10.42	10.54	10.30
Na_2O	1.8623	1.8361	2.53	2.49	2.57	2.68
K_2O	0.4354	0.4399	0.48	0.49	0.50	0.51
P_2O_5	0.1268	0.1465	0.13	0.15	0.14	0.19
Total	99.80	99.01	98.41	98.53	98.90	100.10
µR min. loc.	1221	1224	1228	1229	1229	1229
KK-abs max. loc.	1037	1035	1040	1043	1038	1039
KK-abs FWHM	205	204	196	195	193	193
Mg#	57.1	56.8	62.9	62.6	62.8	62.8
Total Alkali wt.%	2.30	2.28	3.01	2.98	3.07	3.19
Calculated Fe^{3+}/Fe^{2+}	0.6979	0.6984	0.7587	0.7538	0.7608	0.7531
Calculated Refractive Index	1.615	1.615	1.604	1.606	1.605	1.605
CIPW Norm wt.%						
Quartz	5.9	6.0	4.9	4.6	4.2	4.2
Plagioclase	40.1	39.8	40.6	40.5	40.8	41.6
Orthoclase	2.6	2.6	2.8	2.9	3.0	3.0
Diopside	19.9	19.8	24.7	24.4	25.2	24.1
Hypersthene	16.2	15.9	12.4	12.9	12.6	13.7
Ilmenite	4.9	4.9	5.0	5.1	5.0	5.1
Magnetite	10.6	10.5	8.2	8.4	8.4	8.5
Hematite	0.0	0.0	0.0	0.0	0.0	0.0
Apatite	0.3	0.4	0.3	0.4	0.3	0.4
Total	100.5	99.8	99.0	99.1	99.5	100.7

Table 1B: Continued.

	Alk_5B				
Sample Number	64	65	66	67	68
T range (°C)	1414-1417	1414-1417	1414-1417	1414-1417	1414-1417
log (f_{O_2})	-2.95	-2.95	-2.95	-2.95	-2.95
Loop material	Pt	Pt	Pt	Pt	Pt
Duration (h)	5	5	5	5	5
Other	5.47 mg Na_2CO_3 added to 246.91 mg basalt	5.47 mg Na_2CO_3 added to 246.91 mg basalt	5.47 mg Na_2CO_3 added to 246.91 mg basalt	5.47 mg Na_2CO_3 added to 246.91 mg basalt	5.47 mg Na_2CO_3 added to 246.91 mg basalt
wt.%					
SiO_2	49.91	49.97	50.01	50.14	50.06
TiO_2	2.58	2.59	2.68	2.65	2.77
Al_2O_3	11.60	11.56	11.58	11.68	11.55
FeO	10.65	10.50	10.57	10.73	10.58
MnO	0.17	0.20	0.11	0.15	0.16
MgO	9.37	9.58	9.63	9.54	9.47
CaO	10.38	10.46	10.39	10.39	10.42
Na_2O	3.03	2.97	3.12	3.04	3.03
K_2O	0.49	0.45	0.48	0.46	0.47
P_2O_5	0.15	0.20	0.20	0.21	0.18
Total	98.34	98.47	98.77	99.00	98.69
μR min. loc.	1227	1226	1223	1227	1224
KK-abs max. loc.	1038	1037	1040	1040	1038
KK-abs FWHM	189	188	190	189	188
Mg#	61.1	61.9	61.9	61.3	61.5
Total Alkali wt.%	3.52	3.42	3.60	3.50	3.50
Calculated Fe^{3+}/Fe^{2+}	0.7744	0.7742	0.7786	0.7710	0.7756
Calculated Refractive Index	1.607	1.607	1.607	1.607	1.607
CIPW Norm wt.%					
Quartz	1.7	1.8	1.2	1.8	1.9
Plagioclase	42.2	42.0	42.6	42.6	42.2
Orthoclase	2.9	2.7	2.8	2.7	2.8
Diopside	26.5	26.3	26.6	26.0	26.5
Hypersthene	11.7	12.3	12.0	12.2	11.6
Ilmenite	4.9	4.9	5.1	5.0	5.3
Magnetite	8.8	8.6	8.7	8.8	8.7
Hematite	0.0	0.0	0.0	0.0	0.0
Apatite	0.4	0.5	0.5	0.5	0.4
Total	99.0	99.1	99.4	99.6	99.3

Table 1B: Continued.

	Alk_5C			
Sample Number	69	70	71	72
T range (°C)	1408-1412	1408-1412	1408-1412	1408-1412
log (f_{O_2})	-2.95	-2.95	-2.95	-2.95
Loop material	Pt	Pt	Pt	Pt
Duration (h)	5	5	5	5
Other	3.53 mg K_2CO_3 added to 248.79 mg basalt	3.53 mg K_2CO_3 added to 248.79 mg basalt	3.53 mg K_2CO_3 added to 248.79 mg basalt	3.53 mg K_2CO_3 added to 248.79 mg basalt
wt.%				
SiO_2	51.54	51.62	51.31	51.99
TiO_2	2.68	2.58	2.60	2.57
Al_2O_3	11.91	11.61	11.61	11.85
FeO	10.79	10.77	10.82	10.76
MnO	0.18	0.15	0.15	0.14
MgO	9.92	9.78	9.61	9.79
CaO	10.34	10.31	10.41	10.21
Na_2O	1.99	2.02	1.94	1.95
K_2O	0.92	0.97	0.96	0.94
P_2O_5	0.18	0.18	0.18	0.24
Total	100.46	99.99	99.59	100.44
μR min. loc.	1227	1229	1230	1228
KK-abs max. loc.	1042	1039	1042	1043
KK-abs FWHM	198	198	199	200
Mg#	62.1	61.8	61.3	61.9
Total Alkali wt.%	2.91	2.99	2.90	2.89
Calculated Fe^{3+}/Fe^{2+}	0.7497	0.7557	0.7549	0.7460
Calculated Refractive Index	1.606	1.605	1.606	1.605
CIPW Norm wt.%				
Quartz	6.1	6.2	6.5	7.1
Plagioclase	37.7	36.8	36.6	37.3
Orthoclase	5.4	5.7	5.7	5.6
Diopside	22.8	23.6	23.7	22.1
Hypersthene	14.7	14.1	13.6	14.8
Ilmenite	5.1	4.9	4.9	4.9
Magnetite	8.9	8.8	8.9	8.8
Hematite	0.0	0.0	0.0	0.0
Apatite	0.4	0.4	0.4	0.6
Total	101.1	100.6	100.2	101.1

Table 1B: Continued.

	Alk_5D				
Sample Number	73	74	75	76	77
T range (°C)	1408-1412	1408-1412	1408-1412	1408-1412	1408-1412
log (f_{O_2})	-2.95	-2.95	-2.95	-2.95	-2.95
Loop material	Pt	Pt	Pt	Pt	Pt
Duration (h)	5	5	5	5	5
Other	7.23 mg K_2CO_3 added to 247.56 mg basalt	7.23 mg K_2CO_3 added to 247.56 mg basalt	7.23 mg K_2CO_3 added to 247.56 mg basalt	7.23 mg K_2CO_3 added to 247.56 mg basalt	7.23 mg K_2CO_3 added to 247.56 mg basalt
wt.%					
SiO_2	50.99	50.90	50.86	50.78	51.70
TiO_2	2.60	2.61	2.61	2.61	2.59
Al_2O_3	11.64	11.67	11.58	11.60	11.79
FeO	10.37	10.41	10.66	10.71	10.52
MnO	0.17	0.16	0.12	0.17	0.13
MgO	9.62	9.78	9.46	9.72	9.80
CaO	10.26	10.22	10.27	10.45	10.39
Na_2O	1.85	1.91	1.88	1.87	1.93
K_2O	1.65	1.71	1.80	1.72	1.66
P_2O_5	0.17	0.16	0.15	0.19	0.17
Total	99.32	99.53	99.39	99.83	100.68
μR min. loc.	1228	1229	1226	1227	1227
KK-abs max. loc.	1042	1040	1042	1040	1043
KK-abs FWHM	188	189	188	188	191
Mg#	62.3	62.6	61.3	61.8	62.4
Total Alkali wt.%	3.50	3.62	3.68	3.59	3.59
Calculated Fe^{3+}/Fe^{2+}	0.7743	0.7766	0.7782	0.7783	0.7759
Calculated Refractive Index	1.604	1.605	1.605	1.606	1.604
CIPW Norm wt.%					
Quartz	4.6	3.8	4.1	3.7	4.4
Plagioclase	34.2	34.4	33.8	34.0	34.9
Orthoclase	9.8	10.1	10.6	10.2	9.8
Diopside	24.3	24.5	25.1	25.3	24.8
Hypersthene	13.1	13.4	12.4	13.1	13.4
Ilmenite	4.9	5.0	5.0	5.0	4.9
Magnetite	8.5	8.6	8.8	8.8	8.6
Hematite	0.0	0.0	0.0	0.0	0.0
Apatite	0.4	0.4	0.4	0.4	0.4
Total	99.9	100.1	100.0	100.4	101.3

Table 1B: Continued.

	Alk_100				Alk_200		
Sample Number	78	79	80	81	82	83	84
T range (°C)	1408-1412	1408-1412	1408-1412	1408-1412	1408-1412	1408-1412	1408-1412
log (f_{O_2})	-2.95	-2.95	-2.95	-2.95	-2.95	-2.95	-2.95
Loop material	Pt	Pt	Pt	Pt	Pt	Pt	Pt
Duration (h)	100	100	100	100	200	200	200
Other							
wt.%							
SiO_2	51.08	51.85	51.59	52.28	52.55	52.50	53.33
TiO_2	2.73	2.66	2.74	2.73	2.73	2.82	2.76
Al_2O_3	11.78	12.11	11.93	12.27	12.11	12.09	12.46
FeO	10.82	10.70	10.64	10.78	10.26	10.18	10.49
MnO	0.15	0.17	0.21	0.15	0.15	0.18	0.14
MgO	9.88	9.96	10.09	10.16	10.33	9.99	10.20
CaO	10.76	10.48	10.71	10.71	10.67	10.75	10.66
Na_2O	1.39	1.40	1.46	1.47	0.89	0.83	0.88
K_2O	0.42	0.46	0.46	0.43	0.38	0.38	0.39
P_2O_5	0.07	0.07	0.08	0.07	0.03	0.06	0.04
Total	99.08	99.85	99.91	101.05	100.10	99.77	101.35
μR min. loc.	1229	1229	1232	1229	1233	1232	1232
KK-abs max. loc.	1040	1041	1041	1043	1046	1045	1042
KK-abs FWHM	211	211	212	212	224	222	223
Mg#	62.0	62.4	62.8	62.7	64.2	63.6	63.4
Total Alkali wt.%	1.81	1.86	1.92	1.90	1.26	1.21	1.27
Calculated Fe^{3+}/Fe^{2+}	0.7216	0.7133	0.7241	0.7175	0.6988	0.7000	0.6919
Calculated Refractive Index	1.609	1.607	1.608	1.608	1.607	1.607	1.606
CIPW Norm wt.%							
Quartz	9.7	10.2	9.4	9.8	13.0	13.8	13.8
Plagioclase	36.4	37.3	37.0	38.1	35.5	35.2	36.3
Orthoclase	2.5	2.7	2.7	2.5	2.3	2.3	2.3
Diopside	22.0	20.4	21.8	21.1	19.3	19.3	18.5
Hypersthene	14.8	15.9	15.5	15.9	17.0	16.0	17.1
Ilmenite	5.2	5.1	5.2	5.2	5.2	5.4	5.2
Magnetite	8.9	8.8	8.7	8.9	8.4	8.4	8.6
Hematite	0.0	0.0	0.0	0.0	0.0	0.0	0.0
Apatite	0.2	0.2	0.2	0.2	0.1	0.1	0.1
Total	99.7	100.5	100.5	101.7	100.7	100.4	101.9

Table 1B: Continued.

	NNO+5_Pt				NNO+5_dPt			
Sample Number	85	86	87	88	89	90	91	92
T range (°C)	1413-1417	1413-1417	1413-1417	1413-1417	1408-1412	1408-1412	1408-1412	1408-1412
log (f_{O_2})	-0.68	-0.68	-0.68	-0.68	-0.68	-0.68	-0.68	-0.68
Loop material	Pt	Pt	Pt	Pt	dPt	dPt	dPt	dPt
Duration (h)	5	5	5	5	5	5	5	5
Other								
wt.%								
SiO_2	50.33	50.12	50.29	50.00	50.54	49.83	49.11	49.75
TiO_2	2.67	2.70	2.61	2.60	2.65	2.58	2.59	2.60
Al_2O_3	11.78	11.68	11.70	11.60	11.73	11.41	11.32	11.55
FeO	11.06	10.96	10.92	10.95	12.50	12.78	12.62	12.87
MnO	0.18	0.14	0.20	0.17	0.11	0.18	0.18	0.19
MgO	9.73	9.88	9.66	9.69	9.73	9.68	9.46	9.68
CaO	10.33	10.34	10.43	10.44	10.17	10.22	10.32	10.22
Na_2O	1.82	1.89	1.89	1.82	1.82	1.76	1.71	1.78
K_2O	0.47	0.52	0.49	0.49	0.42	0.43	0.39	0.42
P_2O_5	0.25	0.23	0.21	0.19	0.20	0.22	0.20	0.18
Total	98.61	98.46	98.39	97.96	99.87	99.08	97.90	99.23
μR min. loc.	1233	1233	1228	1233	1226	1228	1228	1228
KK-abs max. loc.	1040	1041	1039	1040	1042	1040	1040	1040
KK-abs FWHM	206	206	204	205	211	211	210	210
Mg#	61.1	61.6	61.2	61.2	58.1	57.5	57.2	57.3
Total Alkali wt.%	2.29	2.41	2.38	2.31	2.24	2.19	2.09	2.20
Calculated Fe^{3+}/Fe^{2+}	1.9849	2.0047	2.0096	2.0052	1.9703	1.9692	1.9774	1.9641
Calculated Refractive Index	1.609	1.61	1.609	1.609	1.613	1.615	1.615	1.615
CIPW Norm wt.%								
Quartz	7.9	6.9	7.4	7.4	8.4	8.1	8.0	7.9
Plagioclase	38.0	37.8	38.0	37.4	38.0	36.9	36.5	37.4
Orthoclase	2.8	3.1	2.9	2.9	2.5	2.5	2.3	2.5
Diopside	21.0	21.8	22.1	22.2	20.7	21.3	21.7	21.2
Hypersthene	14.5	14.5	13.8	13.9	14.7	14.3	13.5	14.3
Ilmenite	5.1	5.1	5.0	4.9	5.0	4.9	4.9	4.9
Magnetite	2.8	2.5	3.0	2.9	4.0	4.7	4.5	4.7
Hematite	6.9	7.0	6.7	6.8	7.3	7.0	7.0	7.1
Apatite	0.6	0.5	0.5	0.4	0.5	0.5	0.5	0.4
Total	99.5	99.3	99.3	98.8	100.9	100.1	98.9	100.3

Table 1B: Continued.

	NNO+5 dPt Cont.						DL0413	B-Alk
Sample Number	93	94	95	96	97	98		
T range (°C)	1408-1412	1408-1412	1408-1412	1408-1412	1408-1412	1408-1412	1300	
log (f_{O_2})	-0.68	-0.68	-0.68	-0.68	-0.68	-0.68	NNO-2	air
Loop material	dPt	dPt	dPt	dPt	dPt	dPt	PC exp. Pt capsule	Fe-doped Pt crucible
Duration (h)	5	5	5	5	5	5	3	N/A
Other							Lui (2005) P = 0.5GPa 0.97 wt% H_2O	King (in Dalby 2007)
wt.%								
SiO_2	50.18	48.16	48.39	47.73	47.18	47.83	50.87	48.25
TiO_2	2.57	2.41	2.55	2.47	2.49	2.49	2.59	4.22
Al_2O_3	11.80	10.98	11.25	10.96	10.91	11.11	12.13	12.38
FeO	12.81	15.92	16.07	16.13	16.30	15.92	10.36	14.51
MnO	0.20	0.15	0.09	0.18	0.14	0.19	0.16	0.22
MgO	9.83	9.40	9.31	9.20	8.96	9.29	9.37	5.35
CaO	10.16	9.88	9.94	9.91	9.98	9.90	10.51	10.00
Na_2O	1.70	1.72	1.60	1.50	1.58	1.60	2.06	2.97
K_2O	0.41	0.41	0.35	0.36	0.37	0.34	0.48	0.77
P_2O_5	0.20	0.17	0.19	0.18	0.19	0.19	0.28	0.56
Total	99.86	99.19	99.74	98.62	98.11	98.86	98.81	99.23
µR min. loc.	1225	1224	1222	1221	1223	1223		
KK-abs max. loc.	1041	1036	1034	1035	1038	1031	1038	1034
KK-abs FWHM	212	208	207	208	209	206	193	195
Mg#	57.8	51.3	50.8	50.4	49.5	51.0	61.7	39.7
Total Alkali wt.%	2.10	2.13	1.95	1.86	1.95	1.94	2.54	3.74
Calculated Fe^{3+}/Fe^{2+}	1.9421	1.8536	1.8271	1.8215	1.8334	1.8337		
Calculated Refractive Index	1.614	1.624	1.625	1.626	1.627	1.625	1.604	1.622
CIPW Norm wt.%								
Quartz	8.4	7.7	8.6	8.8	8.1	8.3	1.7	6.2
Plagioclase	37.7	35.6	36.0	34.8	35.0	35.7	40.3	43.3
Orthoclase	2.4	2.4	2.1	2.1	2.2	2.0	2.9	4.6
Diopside	20.0	20.9	19.9	20.1	20.8	20.0	22.9	21.6
Hypersthene	15.2	13.7	14.0	13.6	12.7	13.9	25.1	3.3
Ilmenite	4.9	4.6	4.8	4.7	4.7	4.7	5.0	8.0
Magnetite	4.8	7.9	7.4	8.0	8.0	7.8	1.5	1.6
Hematite	7.0	7.3	7.8	7.4	7.6	7.4	0.0	10.5
Apatite	0.5	0.4	0.4	0.4	0.4	0.4	0.7	1.3
Total	100.9	100.5	101.0	99.9	99.4	100.2	100.1	100.4

B.2. References

Dalby, K.N. (2007) The structure of PbO and natural silicate glasses: An FTIR and XPS study. University of Western Ontario, Ph.D Thesis, Unpublished, 124.

Lui, D.K. (2005) The effects of water on basalt-rhyolite interactions in volcanic systems. University of Western Ontario, M.Sc. thesis, unpublished.

Appendix C: Band fitting data

C.1 Summary of band fitting data

Table C1: Band location and absorbance for basaltic spectra containing $SiO_2 = 51 \pm 0.5$ wt.%.

Sample Name	Sample Number		Peak	900	945	975	1005	1050	1090	1030	1080
NNO-3_Re	8	Band Loc (cm^{-1})	1039	909	941	972	1005	1045	1089	1135	1182
		Absorbance	0.946	0.19	0.25	0.39	0.50	0.66	0.53	0.41	0.25
	7	Band Loc (cm^{-1})	1039	909	942	972	1005	1045	1090	1135	1182
		Absorbance	0.919	0.19	0.25	0.38	0.49	0.65	0.50	0.39	0.24
	5	Band Loc (cm^{-1})	1043	910	941	972	1005	1045	1089	1137	1185
		Absorbance	0.921	0.19	0.22	0.38	0.46	0.65	0.54	0.44	0.25
	6	Band Loc (cm^{-1})	1038	909	941	972	1005	1045	1089	1135	1182
		Absorbance	0.958	0.20	0.25	0.41	0.51	0.67	0.53	0.41	0.25
NNO-1.5_Re	34	Band Loc (cm^{-1})	1037	908	942	973	1007	1048	1092	1135	1182
		Absorbance	0.913	0.19	0.28	0.39	0.53	0.64	0.50	0.39	0.27
	33	Band Loc (cm^{-1})	1038	907	942	973	1005	1046	1090	1135	1182
		Absorbance	0.930	0.20	0.30	0.39	0.52	0.65	0.52	0.41	0.28
NNO-1.5_dPt	37	Band Loc (cm^{-1})	1038	909	943	974	1006	1044	1088	1135	1182
		Absorbance	0.934	0.17	0.25	0.35	0.47	0.65	0.50	0.38	0.21
	40	Band Loc (cm^{-1})	1040	910	943	974	1007	1045	1087	1135	1182
		Absorbance	0.915	0.17	0.23	0.36	0.46	0.62	0.50	0.38	0.20
	38	Band Loc (cm^{-1})	1041	910	943	974	1007	1045	1088	1135	1182
		Absorbance	0.922	0.16	0.23	0.34	0.46	0.63	0.52	0.38	0.21
	36	Band Loc (cm^{-1})	1039	910	942	975	1006	1045	1087	1135	1182
		Absorbance	0.917	0.16	0.23	0.35	0.46	0.63	0.50	0.38	0.20

Table C1: Continued.

Sample Name	Sample Number		Peak	900	945	975	1005	1050	1090	1030	1080
NNO+1	41	Band Loc (cm^{-1})	1042	909	943	974	1007	1045	1090	1137	1182
		Absorbance	0.898	0.15	0.22	0.32	0.45	0.63	0.49	0.36	0.19
	42	Band Loc (cm^{-1})	1038	908	942	974	1006	1045	1089	1137	1182
		Absorbance	0.899	0.15	0.24	0.33	0.46	0.64	0.49	0.35	0.18
	43	Band Loc (cm^{-1})	1038	908	942	974	1007	1046	1090	1137	1183
		Absorbance	0.919	0.17	0.23	0.36	0.48	0.64	0.49	0.36	0.18
NNO+3_Pt	45	Band Loc (cm^{-1})	1041	909	943	975	1005	1044	1089	1136	1182
		Absorbance	0.964	0.17	0.24	0.34	0.46	0.70	0.54	0.38	0.19
NNO+3_dPt	50	Band Loc (cm^{-1})	1040	909	943	975	1006	1045	1089	1137	1183
		Absorbance	0.920	0.18	0.26	0.34	0.49	0.64	0.47	0.36	0.15
NNO+5_dPt	89	Band Loc (cm^{-1})	1042	910	943	975	1009	1048	1091	1137	1182
		Absorbance	0.878	0.19	0.22	0.36	0.46	0.61	0.47	0.36	0.18
Alk-100	78	Band Loc (cm^{-1})	1040	909	943	974	1006	1045	1089	1134	1181
		Absorbance	0.892	0.18	0.24	0.34	0.46	0.63	0.49	0.36	0.21
Alk-5A	61	Band Loc (cm^{-1})	1043	910	944	975	1007	1045	1089	1136	1182
		Absorbance	0.915	0.16	0.21	0.31	0.47	0.63	0.52	0.36	0.18
	63	Band Loc (cm^{-1})	1039	909	943	975	1007	1045	1088	1136	1182
		Absorbance	0.938	0.16	0.23	0.32	0.49	0.65	0.50	0.36	0.18
	62	Band Loc (cm^{-1})	1038	910	943	974	1006	1043	1088	1136	1182
		Absorbance	0.946	0.17	0.22	0.34	0.47	0.66	0.51	0.36	0.18
	60	Band Loc (cm^{-1})	1040	909	943	974	1006	1044	1088	1136	1182
		Absorbance	0.926	0.16	0.22	0.33	0.45	0.65	0.51	0.36	0.18
Alk-5C	71	Band Loc (cm^{-1})	1042	908	943	975	1007	1046	1089	1136	1181
		Absorbance	0.885	0.17	0.22	0.32	0.45	0.62	0.47	0.35	0.17

Table C1: Continued.

Sample Name	Sample Number		Peak	900	945	975	1005	1050	1090	1030	1080
Alk-5D	75	Band Loc (cm^{-1})	1042	909	944	975	1007	1045	1089	1137	1182
		Absorbance	0.909	0.16	0.21	0.31	0.44	0.63	0.49	0.34	0.15
	76	Band Loc (cm^{-1})	1040	909	944	975	1007	1046	1090	1137	1182
		Absorbance	0.936	0.17	0.22	0.33	0.47	0.68	0.47	0.34	0.15
	73	Band Loc (cm^{-1})	1042	909	943	975	1006	1045	1089	1137	1182
		Absorbance	0.944	0.16	0.22	0.31	0.46	0.68	0.49	0.35	0.15
	74	Band Loc (cm^{-1})	1040	911	943	975	1007	1045	1090	1137	1182
		Absorbance	0.940	0.18	0.20	0.33	0.46	0.68	0.49	0.34	0.15

Table C2: Band location and absorbance for basaltic spectra containing $SiO_2 = 52 \pm 0.5$ wt.%.

Sample Name	Sample Number		Peak	900	945	975	1005	1050	1090	1030	1080
NNO-4_Re	1	Band Loc (cm^{-1})	1038	910	941	972	1005	1044	1089	1138	1186
		Absorbance	0.907	0.19	0.23	0.38	0.46	0.64	0.53	0.41	0.22
	2	Band Loc (cm^{-1})	1038	909	941	972	1005	1044	1089	1137	1184
		Absorbance	0.928	0.19	0.24	0.39	0.48	0.65	0.54	0.41	0.24
	3	Band Loc (cm^{-1})	1038	908	941	972	1005	1044	1089	1135	1182
		Absorbance	0.947	0.20	0.25	0.41	0.48	0.67	0.54	0.41	0.26
	4	Band Loc (cm^{-1})	1048	908	942	974	1005	1045	1090	1136	1182
		Absorbance	0.938	0.19	0.27	0.38	0.48	0.67	0.54	0.39	0.25
NNO-1.5 _Re	35	Band Loc (cm^{-1})	1041	909	943	973	1005	1046	1090	1136	1183
		Absorbance	0.943	0.21	0.27	0.39	0.52	0.67	0.54	0.43	0.29
	32	Band Loc (cm^{-1})	1038	910	941	972	1005	1045	1089	1134	1182
		Absorbance	0.913	0.21	0.25	0.39	0.50	0.64	0.51	0.41	0.28
NNO-1.5 _dPt	39	Band Loc (cm^{-1})	1041	910	943	975	1007	1045	1089	1135	1182
		Absorbance	0.933	0.16	0.23	0.36	0.46	0.66	0.50	0.38	0.21

Table C2: Continued.

Sample Name	Sample Number		Peak	900	945	975	1005	1050	1090	1030	1080
NNO-2_Re	28	Band Loc (cm^{-1})	1039	909	943	973	1006	1045	1089	1136	1184
		Absorbance	0.930	0.20	0.26	0.38	0.51	0.64	0.53	0.43	0.26
	30	Band Loc (cm^{-1})	1041	909	943	972	1005	1046	1090	1136	1184
		Absorbance	0.933	0.19	0.26	0.36	0.52	0.65	0.52	0.43	0.26
	29	Band Loc (cm^{-1})	1038	909	943	973	1006	1045	1089	1136	1184
		Absorbance	0.916	0.19	0.25	0.37	0.49	0.61	0.50	0.41	0.25
	31	Band Loc (cm^{-1})	1038	909	943	972	1005	1045	1089	1136	1184
		Absorbance	0.888	0.19	0.26	0.36	0.51	0.63	0.52	0.43	0.25
Alk-5C	69	Band Loc (cm^{-1})	1042	910	944	975	1007	1045	1088	1135	1181
		Absorbance	0.873	0.16	0.21	0.31	0.44	0.59	0.48	0.35	0.17
	70	Band Loc (cm^{-1})	1039	909	943	974	1006	1044	1088	1135	1181
		Absorbance	0.933	0.18	0.23	0.35	0.45	0.65	0.51	0.36	0.18
	72	Band Loc (cm^{-1})	1043	909	944	974	1007	1046	1089	1135	1181
		Absorbance	0.913	0.18	0.22	0.33	0.45	0.64	0.49	0.37	0.19
Alk -5D	77	Band Loc (cm^{-1})	1043	909	944	975	1007	1045	1089	1137	1183
		Absorbance	0.882	0.16	0.20	0.30	0.42	0.62	0.48	0.34	0.15
Alk-100	80	Band Loc (cm^{-1})	1041	908	943	974	1007	1045	1089	1136	1181
		Absorbance	0.895	0.19	0.24	0.35	0.46	0.62	0.50	0.36	0.21
	78	Band Loc (cm^{-1})	1040	909	944	974	1006	1046	1089	1134	1181
		Absorbance	0.892	0.20	0.24	0.35	0.48	0.66	0.50	0.38	0.23
	81	Band Loc (cm^{-1})	1043	909	943	974	1006	1046	1090	1135	1181
		Absorbance	0.918	0.19	0.24	0.34	0.46	0.66	0.51	0.38	0.22